Electron capture in collisions of tin ions with molecular hydrogen

Klaas Bijlsma

university of groningen

faculty of science and engineering

zernike institute for advanced materials

ARCNL

ADVANCED RESEARCH CENTER FOR NANOLITHOGRAPHY

rijksuniversiteit groningen

Electron capture in collisions of tin ions with molecular hydrogen

Proefschrift

ter verkrijging van de graad van doctor aan de
Rijksuniversiteit Groningen
op gezag van de
rector magnificus prof. dr. ir. J.M.A. Scherpen
en volgens besluit van het College voor Promoties.

De openbare verdediging zal plaatsvinden op

dinsdag 18 juni 2024 om 14.30 uur

door

Klaas Isaäc Jeftha Bijlsma

geboren op 10 januari 1994
te Leeuwarden

Promotores
Prof. dr. ir. R.A. Hoekstra
Dr. O.O. Versolato

Beoordelingscommissie
Prof. dr. S. Hoekstra
Prof. dr. R.J.E. Jaspers
Prof. dr. S. Schippers

Contents

CHAPTER 1

Introduction

Over the last six decades, integrated circuits (ICs) have revolutionized society. Integrating many transistors on a chip enables the resulting device to perform logic operations at a high speed. Initially the amount of resources and space required to accumulate enough computing power for useful applications limited the use to dedicated mainframe computers. Numerous advances in the production process of ICs have brought the digital world first to our homes with personal computers and thereafter to everyone's pockets in the form of smartphones. Compared to the early days, the amount of computing power has increased enormously, opening up new applications at a staggering pace. At the same time, the cost of ICs has fallen such that in our modern world more and more devices become "smart" and interconnected through the use of ICs.

The main driver of all these innovations has been the continued miniaturization of the components that make up the IC, enabling ever higher numbers of components to be integrated in an IC. In 1965, the number of components per IC for minimum cost was around one hundred. Gordon Moore, who would co-found Intel a few years later, then predicted that this number would double every year [1]. This prediction had come true over the next ten years, after which he modified it to a doubling every two years [2], which has become known as Moore's law. It is an incredible achievement that industry has been able to follow Moore's law up to this day and age, where commercial computer chips contain tens of billions of transistors. Innovations in the field of photolithography have been crucial to this achievement and will continue to be vital for keeping Moore's law alive.

1.1   Photolithography

The most important step in the production process of computer chips is photolithography, in which light is used to "write" atomic-level structures on a surface of silicon. Many chips are fabricated together on a single silicon disk, called a wafer. In a preceding step in the production process, this wafer, already covered with a layer of insulating silicon dioxide, is covered with a photosensitive material named the photoresist. Before the light is focused onto a small part of the wafer, it passes a mask which contains the blueprint of the structures to be patterned such that areas of the surface which are in the shadow of the mask are not illuminated by the light. In the parts that did get illuminated, the photosensitive molecules change their structure and, depending on the photoresist, either this part of the photoresist or the part in the shadow can be easily removed. After this removal, an etching treatment is applied which removes the silicon oxide in the areas uncovered by photoresist but leaves the remaining photoresist intact. The conductivity of the bare silicon may then be altered by implantation. Next, the remaining photoresist is removed, leaving behind an elevated pattern of silicon oxide. Finally, a new layer of silicon or metallic material is deposited and flattened. All steps together have formed a 2D layer with complex structures exhibiting different conductive properties. By repeating this cycle several times the chip is built up layer by layer.

Diffraction limits the size of the features that can be patterned. The shorter the wavelength of the light used for illumination, the smaller the features can be. The light source is therefore a crucial part of a photolithography machine. Over the years new light sources have been developed, each time reducing the wavelength. Industry started with visible violet light from mercury vapor lamps at a wavelength λ of 436 nm. Later on excimer lasers enabled industry to use deep ultraviolet (DUV) light, first with KrF ($\lambda = 248$ nm) and later with ArF ($\lambda = 193$ nm) lasers systems. Developing powerful light sources at shorter wavelengths has proven to be very challenging, leaving industry stuck at 193 nm until the year 2013, when the Dutch company ASML brought a photolithography machine to the market with a light source in the extreme ultraviolet (EUV) regime, at a wavelength of 13.5 nm. Actual high-volume manufacturing (HVM) of chips by making use of the new EUV machines started in 2019. The further development of the EUV source fuels an active research community, which this thesis contributes to.

1.2 EUV photolithography

The EUV light source is based on the creation of a tin (Sn) plasma [3, 4]. Under the right plasma circumstances (plasma temperature of 20–40 eV, electron density of 10^{19}–10^{21} cm^{-3}), highly charged Sn^{q+} ions ($q = 9$–15) are created in multiply excited states whose energy level separations fortuitously are all close to 92 eV, leading to strong emission of EUV light in a narrow bandwidth around 13.5 nm [5–7]. It is this wavelength, with a 2%-bandwidth, where carefully developed Mo/Si multilayer EUV mirrors have their optimal reflectivity [8, 9]. These (curved) mirrors are used for collecting, transporting and focusing the light in the machine. Their use is necessitated by the fact that EUV light is strongly absorbed by almost all materials, prohibiting the use of conventional glass optics. For the same reason the machine has to operate in a vacuum environment. The problem of low reflectivity in the EUV range of single-layer mirrors is overcome by using Bragg reflector mirrors consisting of a stack of alternating Mo and Si layers. Light is partially reflected from the interface between the low-Z (Si) and high-Z (Mo) material. The thickness of the layers is made such that the reflected light from all layers interferes constructively. A maximum reflectivity of approximately 70% is reached at a wavelength of 13.5 nm [8]. The efficient production of light at this wavelength by Sn has been the reason for choosing this element [10].

Figure 1.1 shows the principle of EUV light generation typical for an industrial EUV photolithography machine. A Sn microdroplet is rapidly heated by firing a powerful infrared laser pulse onto it, creating a so-called laser-produced plasma (LPP) [4]. Absorption of laser light is increased by first hitting the droplet with a pre-pulse that deforms it into a disk-shaped target. As described above, de-excitation of multiply excited highly charged Sn ions results in the emission of photons with a prominent emission peak in a narrow bandwidth around 13.5 nm. A hemispherical mirror, the so-called collector mirror, is used for optimal light collection of the isotropically emitted light. Complementary to the desired EUV photons, the plasma emits energetic highly charged Sn ions which can have undesirable effects. Their energy is on the order of sub-keV to keV but a small fraction of Sn ions may reach energies as high as several tens of keV [12, 13]. The energetic ions could potentially damage plasma-facing surfaces, most notably the collector mirror, by sputtering and implantation. One way of mitigating such a detrimental effect is the use of a buffer gas to slow the ions down by collisional energy transfer.

Several considerations have contributed to the choice of molecular hydrogen (H$_2$) as buffer gas [14]. Next to its ability to stop fast Sn ions, the gas should
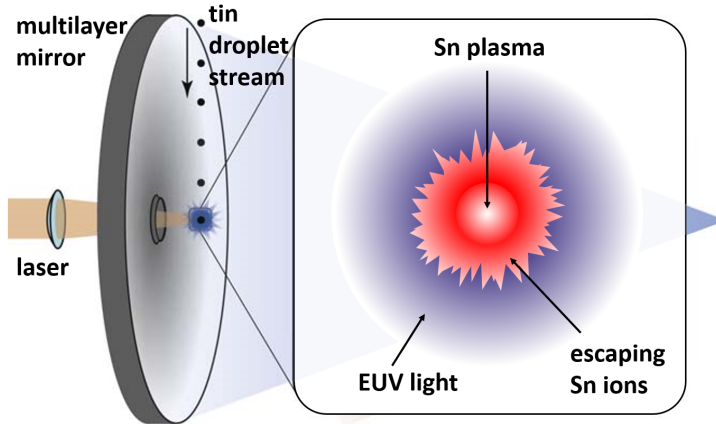
Figure 1.1: Simplified schematic illustrating EUV light generation typical for an industrial EUV photolithography machine. Figure adapted with permission from Ref. [11].

have a low absorption cross section for EUV light. The ionization potential of an H_2 molecule is 16 eV [15, 16]. Once ionized, the binding energy of the remaining electron is 29 eV [15]. An EUV photon of 92 eV can therefore ionize both H_2 and H_2^+, however since the energy difference is large, the cross section is relatively small. Gases of other elements have more electrons, some of them having binding energies closer to 92 eV, leading to higher absorption cross sections. Another advantage of using molecular hydrogen is that hydrogen radicals can bind to Sn to form the gas stannane (SnH_4), which can be pumped away [14]. The amount of (slowed down) Sn ending up on the collector mirror is reduced and deposited Sn can even be removed from the mirror. The hydrogen buffer gas should not be static, but should flow instead. A flow enables the removal of Sn out of the system, and is also needed to cool the system. The buffer gas is heated by the kinetic energy transfer by the Sn ions as well as by absorption of plasma radiation.

The continued demand from industry for higher EUV power poses challenges for the Sn debris mitigation strategies. To fulfil these demands and to optimize source performance, simulations are used to find optimal H_2 pressures and flows. In order for these simulations to produce most reliable output, fundamental atomic data on the collision system $Sn^{q+} - H_2$ is needed as input. Two processes are of particular importance here, namely stopping and electron capture. These processes will be discussed in the next section.

1.3 Atomic processes in buffer gas surrounding EUV generating tin plasma

When a Sn ion projectile collides with an H_2 molecule, a repulsive Coulomb force will act on the particles when the nuclei are in close proximity. Via this interaction, momentum and energy are transferred from the projectile ion to the molecular target. Because the projectile loses energy, this process is commonly called (nuclear) stopping. The amount of transferred momentum and energy depends on how close the ion and target get, and also on how long they interact, i.e. on the velocity of the projectile. How does stopping depend on the charge state of the ion? A more highly charged ion could result in a stronger Coulomb force, however will also push the target away more such that the distance of closest approach increases. It is therefore not straightforward to predict the effect of charge state on the amount of energy transferred. So far, only a single article is available that reports stopping cross sections for Sn ions on H_2, namely by Abramenko *et al.* for Sn^+ and Sn^{2+} ions [17]. They find that for energetic ions ($E > 1$ keV), Sn^+ ions have a larger stopping cross section than Sn^{2+} ions. For EUV source models, it is therefore important to know whether the charge state of the ions traveling through the buffer gas is mainly 1+ or 2+, or perhaps some other charge state.

This is where the process of electron capture, also known as charge transfer or charge exchange, becomes important. When the ion is close to the H_2 molecule, it may capture an electron, or both electrons, from the H_2 molecule. Three processes can be distinguished, being single electron capture (SEC or SC):

$$Sn^{q+} + H_2 \rightarrow Sn^{(q-1)+} + H_2^+, \tag{1.1}$$
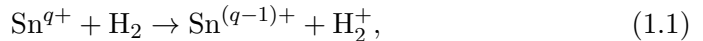
bound double capture (BDC or simply DC):

$$Sn^{q+} + H_2 \rightarrow Sn^{(q-2)+} + 2H^+, \tag{1.2}$$

and autoionizing double capture (ADC):

$$Sn^{q+} + H_2 \rightarrow Sn^{(q-2)+} + 2H^+ \rightarrow Sn^{(q-1)+} + 2H^+ + e^-. \tag{1.3}$$
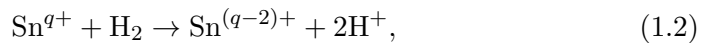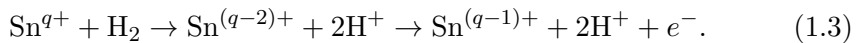
In all three cases, the ion's initial charge state q is reduced. Even though the ions responsible for emission of 13.5 nm-wavelength light have charge states of 9+ to 15+, ions emitted by the plasma have lower charge states due to recombination at the peripheral part of the plasma. Their charge states range from 8+ down to 1+, however energetic ions ($E > 1$ keV) predominantly have

relatively high charge states of 4+ to 7+ [13]. While traveling through the hydrogen gas, their charge states will be further reduced by multiple charge transfer collisions with H_2 molecules. It can be expected that this process stops at 2+, because the binding energy of the outer electron in Sn^+ is, compared to the ionization potential of H_2, too low to make the capture process from Sn^{2+} to Sn^+ energetically favourable. In this thesis however, we show that this process does happen in an LPP plasma source and explain the mechanism by which it occurs. Moreover, we show that Sn^+ can also be efficiently generated through double electron capture by Sn^{3+}.

It is important for the EUV source simulations to include the process of electron capture, because the efficiency of energy transfer depends on the charge state. With electron capture included, information about which charge states are present at a given position in the source vessel can be obtained. Also, it would be possible to establish what charge states are dominantly present, enabling defining which stopping cross sections would be most relevant. However, no literature is available reporting electron capture cross sections for Sn ions colliding with H_2 molecules. This thesis presents the results of first studies on electron capture in this collision system.

1.4 Zernike low-energy ion beam facility

The experiments described in this thesis for measuring electron capture cross sections are performed with a beam of Sn ions produced with the Zernike low-energy ion beam facility (ZERNIKELEIF), located at the University of Groningen. The facility will be briefly described here, more details can be found in [18, 19]. Figure 1.2 shows a photograph of ZERNIKELEIF.

The Sn ions constituting the ion beam are produced with an electron cyclotron resonance ion source (ECRIS). It consists of a vacuum plasma chamber, which is surrounded by a permanent hexapole magnet (~ 1 T) creating a radially and axially confining field. First, Sn vapor is generated by heating solid Sn to approximately 1100°C in a crucible oven located inside the source. Due to the magnetic field, free electrons will revolve around closed circular orbits with an angular gyration frequency given by

$$\omega = \frac{e}{m}B, \qquad (1.4)$$

where e and m are the charge and mass of the electron, respectively, and B the magnetic field strength. A radio frequency (RF) field of 14 GHz is injected into the chamber. Electrons gyrating on a specific magnetic field iso-surface are in
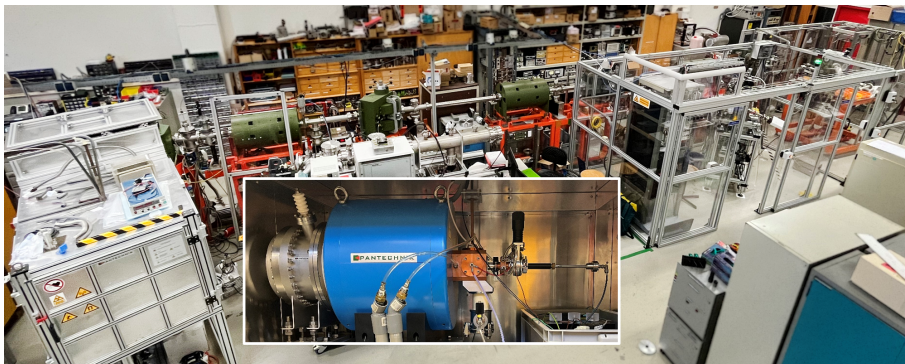
Figure 1.2: Photograph of the Zernike low-energy ion beam facility (ZERNIKELEIF). The inset shows the inside of the source cabinet on the left, containing an electron cyclotron resonance ion source (ECRIS). On the right, the gas-target (left) and solid-target (right) experimental setups can be seen. These setups can be floated on a high potential to decelerate incoming ions. Therefore, as a safety measure, the setups are enclosed by a cage.

resonance with the RF field and are accelerated up to energies high enough to ionize Sn atoms and Sn ions upon a collision, thereby creating a plasma. A plasma potential V_p of typically 10 V is generated between the plasma and the chamber walls. The RF power can be tuned; higher power enables the production of higher charge states. The source is floating on a high potential V_s, up to 30 kV. During extraction from the source the potential energy of the ions is converted into kinetic energy. The final energy of an ion with charge state q is given by

$$E = q(V_s + V_p). \tag{1.5}$$

An analyzing (electro-)magnet is used to select one particular charge state out of all charge states extracted from the source by setting the magnetic field strength such that ions with this charge state are bent over exactly 110° into the beamline. Moreover, the different isotopes are also separated which allows further beam purification. The ions can be transported through the beam line towards either the gas-target (this thesis) or the solid-target experimental setup. In the beamline, three sets of triplet quadrupole magnets are present for ion beam focusing and two sets of small dipole correction magnets can be used to optimize the position of the ion beam in the horizontal and vertical direction. A dipole magnet is used to bend the ion beam out of the central beamline towards an experimental setup.

The physical processes studied at the experimental setups are dependent

on the energy of the ions, therefore the experiments are typically repeated for various ion energies. Equation 1.5 shows that the ion energy can be varied by changing V_s. However for source potentials below 3 kV, ion extraction and transport become increasingly inefficient resulting in too low ion beam currents arriving at the experimental setups. This means that only the highest energies typical for LPP Sn ions can be generated, e.g. for Sn^{3+} ions the minimum energy obtained from ZERNIKELEIF is 9 keV. To overcome this limitation, the facility has been upgraded during the course of the PhD project with the possibility to float the gas-target setup on a high potential such that part of the kinetic energy of the ions is again converted into potential energy, thereby decelerating the ions after their transport to the setup.

1.5   Thesis outline

This thesis studies electron capture in collisions of Sn ions with H_2 molecules for charge states and energies relevant for EUV light sources for photolithography machines. Because the charge state influences ion stopping, ion mitigation models for EUV sources can benefit from the work presented in this thesis. Specifically, the production of Sn^{2+} and Sn^+ ions out of Sn^{3+} ions is studied in this thesis. There are several reasons for this focus. First of all, the electronic structure of Sn^{3+}, $[Kr]4d^{10}5s$, is convenient for both experiment and theory because the single valence electron makes it a relatively simple system. Second, the electron capture cross sections for higher charge states are, based on the basic over-the-barrier model [20], expected to be larger. This means that soon after Sn ions are emitted from the LPP and start to travel through the buffer gas, they have their charge state reduced. For most of the distance towards the collector mirror, they will travel with a lower charge state. Given that the stopping power of Sn^+ ions is larger than for Sn^{2+} ions, it is then important to know at which positions in the source the ions convert from 3+ to 2+ and to 1+. The main method for studying these processes is by performing controlled crossed-beam experiments. Next to that, we collaborate with the Theory of Atomic and Molecular Collisions group of professors Rabadán and Méndez from the Autonomous University of Madrid (Universidad Autónoma de Madrid - UAM), who calculate electron capture cross sections using semiclassical and quantal models. By comparing our results to theirs, both experimental and theoretical methods can be benchmarked and improved. Moreover, from the model we can learn more about the specific mechanism by which electron capture occurs.

Chapter 2 presents the first combined experimental and theoretical study of

charge transfer in collisions of Sn^{3+} ions with H_2 molecules. The experiments were performed before the upgrade equipping the setup with deceleration capabilities, hence the minimum energy is limited to 9 keV. The focus of this chapter is on single electron capture.

In Chapter 3 we perform experiments on an actual LPP source surrounded by an H_2 buffer gas. Charge-state-resolved kinetic energy spectra are presented for various pressures of the buffer gas. Contrary to expectation, we observe the production of energetic Sn^+ ions in the buffer gas. We propose that these are produced by electron capture not from the ground state but from a metastable state of Sn^{2+}.

Chapter 4 presents a follow-up research on the study of Chapter 2. Two major upgrades have been implemented in the experimental setup. The first is the already mentioned ability to decelerate incoming ions, which enabled us to extend the energy range down to 50 eV. Second, the ion detector is changed to one which provides charge state resolution. With it, we measured both single and double electron capture cross sections for Sn^{3+}. The latter shows a remarkable energy dependence, with negligible cross sections above an energy of approximately 5 keV and substantial ones below it.

In Chapter 5 we focus on the magnitude and energy dependence of the cross section of the electron capture reaction identified in Chapter 3, i.e. Sn^{2+*} to Sn^+. Experimentally, these are extracted from double collisions of Sn^{3+} ions.

Finally, in the Conclusion and outlook, the main conclusions drawn from all chapters combined are formulated and suggestions for further research are given.

References

[1]   G. E. Moore, "Cramming more components onto integrated circuits", *Electronics* **38** (1965).

[2]   G. E. Moore, "Progress in digital integrated electronics", *Int. Electron Devices Meet., IEEE*, 11–13 (1975).

[3]   V. Bakshi (ed), *EUV lithography*, 2nd edn, Bellingham, WA: SPIE Press, 2018.

[4]   O. O. Versolato, "Physics of laser-driven tin plasma sources of EUV radiation for nanolithography", *Plasma Sources Sci. Technol.* **28**, 083001 (2019).

[5]   W. Svendsen and G. O'Sullivan, "Statistics and characteristics of xuv transition arrays from laser-produced plasmas of the elements tin through iodine", *Phys. Rev. A* **50**, 3710–3718 (1994).

[6]   J. Colgan, D. Kilcrease, J. Abdallah, M. Sherrill, C. Fontes, P. Hakel, and G. Armstrong, "Atomic structure considerations for the low-temperature opacity of Sn", *High Energy Density Phys.* **23**, 133–137 (2017).

[7]   F. Torretti, J. Sheil, R. Schupp, M. M. Basko, M. Bayraktar, R. A. Meijer, S. Witte, W. Ubachs, R. Hoekstra, O. O. Versolato, A. J. Neukirch, and J. Colgan, "Prominent radiative contributions from multiply-excited states in laser-produced tin plasma for nanolithography", *Nat. Commun.* **11**, 1–8 (2020).

[8]   S. Bajt, J. B. Alameda, T. W. Barbee Jr., W. M. Clift, J. A. Folta, B. Kaufmann, and E. A. Spiller, "Improved reflectance and stability of Mo-Si multilayers", *Opt. Eng.* **41**, 1797 (2002).

[9]   V. Banine and R. Moors, "Plasma sources for EUV lithography exposure tools", *J. Phys. D: Appl. Phys.* **37**, 3207 (2004).

[10] V. Y. Banine, K. N. Koshelev, and G. H. P. M. Swinkels, "Physical processes in EUV sources for microlithography", *J. Phys. D: Appl. Phys.* **44**, 253001 (2011).

[11] D. Kurilovich, "Laser-induced dynamics of liquid tin microdroplets", English, PhD thesis (Vrije Universiteit Amsterdam, 2019).

[12] A. Bayerle, M. J. Deuzeman, S. van der Heijden, D. Kurilovich, T. de Faria Pinto, A. Stodolna, S. Witte, K. S. E. Eikema, W. Ubachs, R. Hoekstra, and O. O. Versolato, "Sn ion energy distributions of ns-and ps-laser produced plasmas", *Plasma Sources Sci. Technol.* **27**, 045001 (2018).

[13] L. Poirier, A. Bayerle, A. Lassise, F. Torretti, R. Schupp, L. Behnke, Y. Mostafa, W. Ubachs, O. O. Versolato, and R. Hoekstra, "Cross-calibration of a combined electrostatic and time-of-flight analyzer for energy-and charge-state-resolved spectrometry of tin laser-produced plasma", *Appl. Phys. B* **128** (2022).

[14] I. Fomenkov, D. Brandt, A. Ershov, A. Schafgans, Y. Tao, G. Vaschenko, S. Rokitski, M. Kats, M. Vargas, M. Purvis, R. Rafac, B. L. Fontaine, S. D. Dea, A. LaForge, J. Stewart, S. Chang, M. Graham, D. Riggs, T. Taylor, M. Abraham, and D. Brown, "Light sources for high-volume manufacturing EUV lithography: technology, performance, and power scaling", *Adv. Opt. Techn.* **6**, 173–186 (2017).

[15] T. E. Sharp, "Potential-energy curves for molecular hydrogen and its ions", *At. Data Nucl. Data Tables* **2**, 119–169 (1971).

[16] M. Wacks, "Franck-Condon factors for ionization of H_2, HD and D_2", *J. Res. Natl. Bur. Stand., Sect. A* **68**, 631 (1964).

[17] D. Abramenko, M. Spiridonov, P. Krainov, V. Krivtsun, D. Astakhov, V. Medvedev, M. van Kampen, D. Smeets, and K. Koshelev, "Measurements of hydrogen gas stopping efficiency for tin ions from laser-produced plasma", *Appl. Phys. Lett.* **112**, 164102 (2018).

[18] M. Deuzeman, "Generation and interactions of energetic tin ions", English, PhD thesis (University of Groningen, 2019).

[19] S. Rai, "Ionic interactions around EUV generating tin plasma", English, PhD thesis (University of Groningen, 2023).

[20] A. Niehaus, "A classical model for multiple-electron capture in slow collisions of highly charged ions with atoms", *J. Phys. B: At. Mol. Phys.* **19**, 2925–2937 (1986).

Charge exchange in collisions of 1–100 keV Sn^{3+} ions with H$_2$ and D$_2$

Abstract

Absolute cross sections for single electron capture by Sn^{3+} colliding with H_2 and D_2 have been measured and calculated in the energy range of 1–100 keV. The cross sections are determined by measuring the change in ion beam current with varying target density and by measuring the yields of charged target fragments by means of a time-of-flight spectrometer. The results for D_2 show good agreement with our seven-state semiclassical calculations, while for H_2 the experimental results increase more strongly than the calculations towards lower energies. This discrepancy is attributed to vibrational effects, not included in the calculations, that lead to the breakdown of the Franck-Condon approximation.

2.1   Introduction

Charge exchange in collisions of keV-energy multiply-charged ions with neutral species remains an active research topic ever since the advent of highly charged ion sources (e.g. [1–3]). Experiments have continually challenged, in ever-increasing detail, the theoretical approaches, which were initially classical and subsequently semiclassical in their description of the electron dynamics during the interactions (e.g. [4]). The bulk of the research has dealt with low-Z ions, because the number of active electrons and quantum states to be included in the calculations is limited and because intense ion beams can most easily be produced from low-Z, gaseous species. More complex and heavier ions, in particular intermediately charged Fe ions, have been studied (e.g. [5–7]) because of their astrophysical and fusion plasma relevance. Over the past years, Sn ions have moved into the focus of highly charged ion physics [8–14] as Sn alloys are considered for fusion plasma vapor shielding [15–17] and foremost because laser-produced Sn plasma is the source of 13.5-nm extreme ultraviolet (EUV) light driving state-of-the-art EUV nanolithography machines [18–22]. In such machines, multilayer mirror optics collect and guide the EUV light [23, 24]. To prevent damage to the optics by the energetic Sn ions [25–27], the plasma is embedded in H$_2$ gas. Fundamental data on charge exchange and stopping in Sn^{q+} + H$_2$ collisions is missing though it is crucial for accurate and predictive modeling.

Here in a joint experimental and theoretical study, absolute cross sections for single electron capture (SC) from H$_2$ (and its heavier isotopologue D$_2$) by Sn^{3+}, i.e., for the reaction

$$\text{Sn}^{3+} + \text{H}_2 \rightarrow \text{Sn}^{2+} + \text{H}_2^+ \tag{2.1}$$

are determined. The choice for starting out with Sn^{3+} ions is based on its alkali-like electronic configuration: [Kr]$4d^{10}5s$. For alkali-like ion beams, metastable fractions are negligible [28] making the collision systems tractable to experiment and theory. In the experiments, Sn^{3+} ions in the energy range of 9 to 51 keV are used as projectiles. Due to the high mass of the Sn ions, this corresponds to low velocities of 0.05 to 0.13 a.u. The cross section measurements are based on the measurement of the changes in ion beam current with changing target density. Therefore, in the determination of the SC cross sections, one needs to consider possible contributions of two-electron processes: bound double capture (BDC, Eq. 2.2a) and autoionizing double capture (ADC, Eq. 2.2b).

$$\text{Sn}^{3+} + \text{H}_2 \rightarrow \text{Sn}^+ + 2\text{H}^+ \tag{2.2a}$$

$$\text{Sn}^{3+} + \text{H}_2 \rightarrow \text{Sn}^{2+} + 2\text{H}^+ + e \tag{2.2b}$$
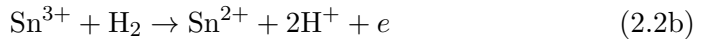
BDC is expected to have a small cross section because the two-electron capture channel closest to resonance is the one leading to capture into the $[\text{Kr}]\,4d^{10}\,5s^2\,5p$ ground electronic configuration of Sn^+ which is endothermic by approximately 6 eV. All other $5s^2\,nl$ configurations are more endothermic and thus not likely to be populated at all. ADC requires the population of doubly excited levels of even much higher endothermicity. Therefore it is safe to exclude ADC from our analysis. The BDC contribution is extracted from Time-of-Flight (ToF) spectrometry on the target fragments. In BDC, the two protons resulting from the Coulomb explosion of $[\text{H}_2]^{2+}$ get kinetic energies of 9.7 eV each, while in SC reactions the few protons created next to the by far dominant H_2^+ production channel have energy close to 0 eV. The yield of 9.7-eV protons is used to correct the data for any BDC contribution. At the same time, this allows for an assessment of the BDC cross sections.

The calculations of SC total cross sections for ion-molecule collisions are carried out by applying methods based on those developed for ion-atom collisions; for instance, at the energies of the present work, expansions in terms of electronic functions of the quasi-molecule formed during the collision, within either semiclassical or quantal frameworks. Besides the obvious difference of treating a many-center system, there are two important characteristics of ion-molecule collisions that must be taken into account. First, in the semiclassical treatment, where the projectile follows a classical trajectory, the probabilities of a given process depend on the orientation of the molecule with respect to the ion trajectory. It is necessary to average the calculated cross sections over a set of collisions with different molecular orientations. The methodology employed in this work ([29] and references therein) employs molecular data (electronic energies and dynamical couplings) calculated along the trajectory. The second important difference between ion-molecule collisions with respect to ion-atom collisions is the presence of molecular nuclear motion. The use of vibronic bases to simultaneously describe the electronic and vibrational motions leads to cumbersome calculations that however allowed us to reproduce the maximum of the electron capture cross section found in detailed experiments for H^+–H_2 collisions, and explain this maximum as a consequence of the interplay between electronic and nuclear motions [30].

In the following section, Part 2.2.1 describes the experimental setup, while Subsections 2.2.2 - 2.2.5 present the actual measurement procedure and all
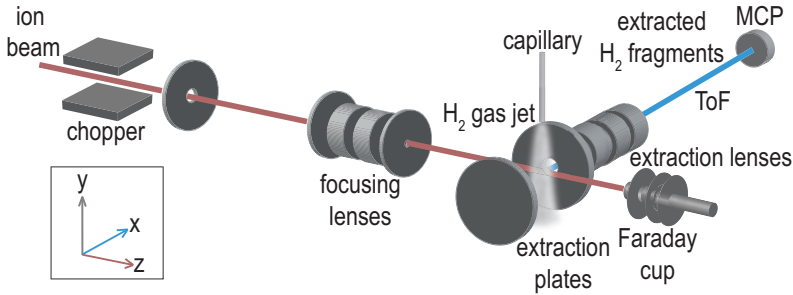
Figure 2.1: Schematic of the crossed-beam setup, CHEOPS, used to measure charge exchange cross section for keV Sn^{3+} ions colliding on H_2 (and D_2).

the calibration and data analysis steps. Section 2.3 describes the theoretical approaches used to calculate single-electron capture in collisions of Sn^{3+} on either H_2 or D_2. Thereafter, the experimental and theoretical data are compared and discussed in Section 2.4.

2.2   Experimental methods

The data presented in this work have been obtained by colliding a beam of mono-energetic Sn^{3+} ions with a neutral gas target (H_2 or D_2) in a series of crossed-beam type experiments. The ions are extracted from an electron cyclotron resonance ion source (ECRIS) stationed at the Zernike low-energy ion beam facility (ZERNIKELEIF) at the University of Groningen. Ions with energies in the range of $3q$ to $25q$ keV can be generated, where q is the charge state of the ion. The ions extracted from the ion source are selected for a given mass-over-charge ratio (m/q) using a 110° analyzing magnet with a resolution of about 0.5%. ^{120}Sn is the most abundant isotope of Sn but for a charge state of 3, the corresponding m/q is 40 which is the same as that of Ar^+. Hence, to prevent possible contamination of the Sn^{3+} beam by Ar^+ impurities, $^{118}Sn^{3+}$ is used. Sn atoms are introduced into the source chamber by heating a crucible oven filled with solid tin. The analyzed ion beam is transported through the central beamline and steered into the gas target setup by a 45° bending magnet.

2.2.1   The crossed-beam setup

The relevant features of the gas target setup, CHEOPS (CHarge Exchange Observed by Particle Spectroscopy) are depicted in Figure 2.1. The ion beam is collimated by a set of four apertures, the smallest one of 1 mm diameter,

positioned at the entrance of the collision chamber. In the chamber, the base pressure is $\approx 2 \times 10^{-8}$ mbar. A ϕ 0.5 mm grounded capillary is located 14 mm above the center of the ion beam. The gas flowing into the chamber, via the capillary, is regulated by a high precision mass flow controller (Bronkhorst FG-200CV) thus creating a localized jet of the H_2 target gas, which is crossed by the beam. A flowrate of 1 ml/min was used throughout the experiments unless stated otherwise and the corresponding chamber pressure for that flow is $\approx 1.5 \times 10^{-4}$ mbar. The ions are collected at the end of the setup by a Faraday Cup (FC) and the beam current is measured using a Keithley 6485 Picoammeter. The FC assembly consists of three components: i) the entrance cap with a ϕ 3 mm aperture, ii) a ϕ 6 mm guard ring, and iii) the FC. The guard ring is biased at -38 V to suppress the escape of secondary electrons from the FC. The cap shields the collision chamber from the field of the guard ring. The whole FC assembly is mounted on an XY translation stage. By scanning the assembly in the horizontal and vertical plane and recording the current at the cap and FC a typical beam width of ≈ 1.5 mm at the FC is determined.

Charged collision fragments produced in the central crossed-beam region can be extracted towards a Time-of-Flight (ToF) spectrometer, which allows for measuring the yields of atomic H^+ and molecular H_2^+ ions. The ToF measurements (see Section 2.2.4) require the continuous ion beam to be chopped in short pulses to have a start pulse for the spectrometer. At a rate of up to 8 kHz, short ≈ 20 ns ion beam pulses are generated by sweeping the ion beam over the entrance aperture by means of alternating the opposite voltages on two electrodes (chopper plates, see Figure 2.1).

Fragments under the influence of the field across the collision center pass through a ϕ 5 mm aperture into the ToF spectrometer. An electrostatic lens system consisting of four elements is then used to accelerate and focus the fragments into the ToF tube floating at -1700 V. Towards the end of the tube, the fragments get detected by a microchannel plate (MCP) detector whose front plate is set to -2100 V. The total flight length from the collision center to the detector is 1.13 m. The MCP detector is connected to a pick-off amplifier followed by a constant-fraction-discriminator (CFD) to amplify and filter the signals. The output of the discriminator is fed to a multi-hit time-to-digital converter (TDC, FAST P7888) in order to record the ToF spectrum.
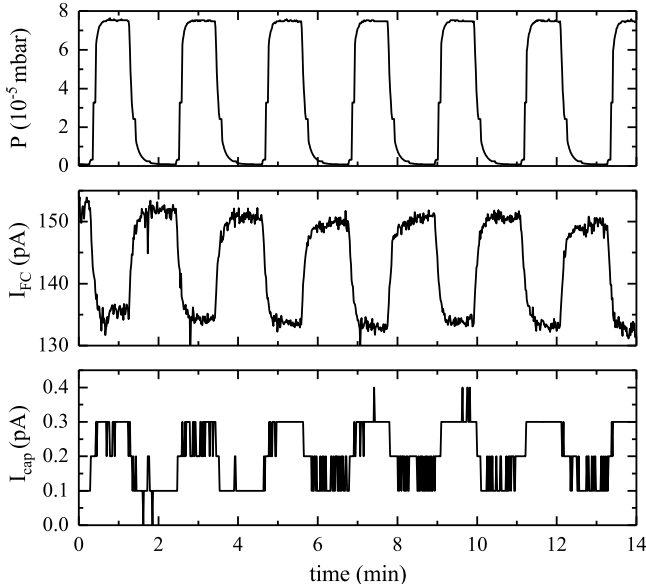
Figure 2.2: Typical time trace: Variation of ion beam current measured at the Faraday cup (middle panel) and the cap (lower panel) with toggling H$_2$ flow rate between 0 and 0.5 ml/min. The top panel shows the associated time trace of the pressure in the collision chamber.

2.2.2   Procedure of measuring charge exchange cross sections

Figure 2.2 shows the time trace of a typical measurement run. The flow controller is programmed to sequentially start and stop the flow of gas into the chamber. The top panel in the figure shows the variation of chamber pressure with acquisition time. When the gas flows from the capillary into the chamber, the ion beam crossing the gas may undergo charge exchange collisions. This leads to a decrease in the beam current measured by the FC as shown in the middle panel of the figure. The collision of the ions with the gas also results in angular scattering of the ion beam. If the scattered ions hit the cap, a current is generated and recorded as depicted in the bottom panel of the figure. The effect is small, however; the change in cap current is typically around 1% of the change in FC current.

The full set of differential equations describing the evolution of the charge state of the ions along their trajectory (z) through the collision chamber is as follows:

$$\frac{dN^{3+}}{dz} = -(\sigma_{32} + \sigma_{31})nN^{3+} \tag{2.3a}$$

$$\frac{dN^{2+}}{dz} = \sigma_{32}nN^{3+} - (\sigma_{21} + \sigma_{20})nN^{2+} \tag{2.3b}$$

$$\frac{dN^{1+}}{dz} = \sigma_{31}nN^{3+} + \sigma_{21}nN^{2+} - \sigma_{10}nN^{1+} \tag{2.3c}$$

$$\frac{dN^{0+}}{dz} = \sigma_{20}nN^{2+} + \sigma_{10}nN^{1+}. \tag{2.3d}$$

In the low-density, single-collision regime the set of equations is reduced to:

$$\frac{dN^{3+}}{dz} = -(\sigma_{32} + \sigma_{31})nN^{3+}. \tag{2.4}$$

Here, σ_{ij} denotes the cross section for electron capture by an ion in an initial charge state i leading to a final charge state j, n is the number density of the target, and N^{q+} denotes the number of Sn ions with charge state q. The numbers of ions are related to the ion current I measured in the FC via $I = qN^{q+} + (q-1)N^{(q-1)+} + (q-2)N^{(q-2)+}$. The differential equation for single-collision conditions, Eq. 2.4, can be solved analytically, yielding the following general relation between ion beam current and the single-capture cross section σ_{SC} (or $\sigma_{q,q-1}$)

$$\sigma_{SC} = \frac{-\ln\left(a\frac{I}{I_o} - b\right)}{(1+f)\int_0^L n(z)dz}, \tag{2.5}$$

where I_0 is the initial ion current, f the ratio between two- and one-electron capture ($f = \frac{\sigma_{BDC}}{\sigma_{SC}}$), $a = \frac{(1+f)q}{1+2f}$, $b = \frac{(1+f)q-(1+2f)}{1+2f}$, and L the path length the ions travel through the collision chamber. Here for Sn^{3+}, $q = 3$. As will be discussed in detail in Section 2.2.4, the bound double capture fraction f is estimated experimentally from ToF measurements on target fragments (H$^+$ and H$_2^+$). However, first in Section 2.2.3 the determination of the integral target density $\int_0^L n(x)dx$ is presented.

2.2.3 Calibration of the integral target density

Accurate, absolute target density measurements over the ion trajectory are difficult. Therefore, we determine the integral target density using a reference collision system for which the charge exchange cross sections are very well known: H$^+$ + H$_2$; see, e.g., the data review by Nakai *et al.* [32]. From the
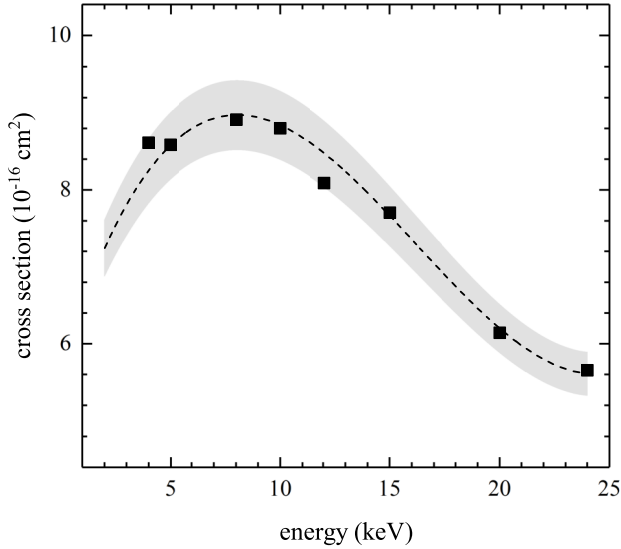
Figure 2.3: Single electron capture cross section for protons on H_2 (solid squares). Dashed curve: trend line through reference data [31]. The gray band depicts the $\pm 5\%$ systematic uncertainty associated with the McClure data.

review paper we see that for protons only single electron capture (σ_{10}) needs to be considered; in the energy range of 5 to 20 keV, double electron capture is approximately two orders of magnitude smaller than one-electron capture [32]. This implies that Eq. 2.5 for protons on H_2 simplifies significantly (with $f = 0$ and $q = 1$) and can be rewritten to:

$$\int_0^L n(z)dz = -\frac{\ln \frac{I}{I_o}}{\sigma_{10}} = \beta P \tag{2.6}$$

to extract the integral target density from a measurement of the change of proton current. Here β is introduced as the proportionality factor between the integral target density and the pressure P in the collision chamber. From the many studies reported in Nakai's review paper [32], we used the cross sections σ_{10} reported by McClure [31] for calibration. McClure's set of cross sections covers our range of interest, and at energies of 5 keV and lower, there is excellent agreement with the results of an elaborate joint experimental and theoretical study by Urbain *et al.* [30].

Figure 2.3 shows σ_{10} cross sections for $H^+ + H_2$. The dashed curve shows a trend line through the reference data of McClure [31] and the associated gray band depicts the systematic $\pm 5\%$-uncertainty on the McClure data. The solid

squares represent our measurements, which were fitted to the reference line with a single common factor. In this way, for the scaling factor β a value of $(1.03 \pm 0.07) \times 10^{18}$ cm^{-2} mbar^{-1} is determined.

The integral target density changes with the choice of gas. Therefore, we also measure β for D_2, the other target gas used in the experiments, and find a value of $(1.15 \pm 0.08) \times 10^{18}$ cm^{-2} mbar^{-1}. Here it is assumed that the cross sections for H_2 and D_2 are the same as their ionization potentials are equal and the proton velocities are rather high (0.4–1 a.u.) [33, 34].

2.2.4 Determination of two-electron capture contributions to the measurements

From Eq. 2.5 it is seen that one needs to know f, the ratio between BDC and SC, to obtain the SC cross sections. The distribution of target fragments allows for the assessment of the ratio between BDC and SC. SC (Eq. 2.1) generates molecular ions H_2^+ of ≈ 0 eV. The capture of two electrons (Eqs. 2.2a, 2.2b) leads to the dissociation of the H_2 molecule into two energetic protons of 9.7 eV. Figure 2.4 shows two typical ToF spectra, one for Sn^{3+} and one for N^{5+} colliding on H_2. In both cases, the strongest peak is the H_2^+ peak associated with SC (cf. Eq. 2.1). The contribution of protons to the ToF spectrum is weak.

As can be seen in the zoom in Figure 2.4, the proton "peak" consists of three peaks of which the central one is located at the expected ToF of H$^+$ fragments and represents protons of ≈ 0 eV stemming from gentle dissociation of H_2^+ molecular ions excited just above the dissociation limit (see e.g. [35]). The two peaks on either side of the 0-eV proton peak correspond to 9.7-eV protons from BDC where the peak at slightly shorter ToFs belongs to 9.7-eV protons emitted in the forward direction to the ToF spectrometer (H$_f^+$) and the one at longer ToFs is due to protons emitted backward, away from the ToF spectrometer (H$_b^+$). Backward emitted protons get reflected by the extraction field (see inset (a) in Figure 2.4) into the direction of the ToF spectrometer explaining the time difference between the forward and backward emitted 9.7-eV protons. The difference in ToF (ΔT) scales with the square root of the kinetic energy release (U_{KER}) of the dissociation process (e.g. [36]) and for singly charged fragments it is given by:

$$\Delta T = \frac{\sqrt{8\,\mu\,U_{\text{KER}}}}{E}, \tag{2.7}$$

with E being the extraction field (in the present experiment 40 V/cm), and
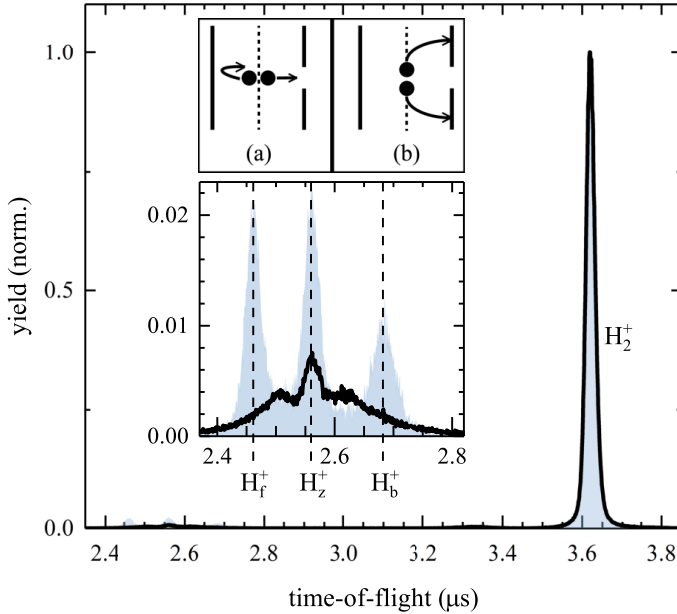
Figure 2.4: Time-of-flight (ToF) spectra of target fragments for 48 keV Sn^{3+} (line) and 50 keV N^{5+}(fill) colliding on H$_2$. For direct comparison, the spectra are normalized to the H$_2^+$ peak height. The enlargement shows the very weak proton peaks. Expected peak positions for 9.7-eV protons from BDC are marked by dashed lines. H$_f^+$ and H$_b^+$ refer to forward and backward emitted protons, respectively. The position of 0-eV protons, H$_z^+$, of course lying between H$_f^+$ and H$_b^+$, is also marked by a dashed line for reference.

with the reduced mass, μ, being 0.5 and 1 for H$_2$ and D$_2$, respectively.

The 9.7-eV protons emitted along the beam axis are intercepted by the entrance diaphragm of the ToF spectrometer, see Figure 2.4b. Therefore, in general, only 9.7-eV protons emitted in small cones towards or away from the ToF spectrometer are detected, leading to the two proton peaks labeled H$_f^+$ and H$_b^+$ in Figure 2.4, respectively. Using 50 keV N^{5+} and 60 keV O^{6+} ions colliding with H$_2$ as reference systems for which cross sections for single-electron capture and for bound and autoionizing double-electron capture have been measured [37–43], the percentage of the 9.7-eV protons that are detected in our experimental setup, α, is determined to be $(5 \pm 1)\%$.

Figure 2.4 compares the ToF spectra, normalized to their H$_2^+$ peak heights, of 48 keV Sn^{3+} and 50 keV N^{5+} colliding with H$_2$. While the 9.7-eV H$_f^+$ and H$_b^+$ are very prominent for N^{5+}, they are barely present for Sn^{3+}. This hints at

a significantly lower double capture contribution in the case of Sn^{3+} ions than for N^{5+} for which single and double capture are of similar magnitude. Over the energy range of 10–50 keV, the ratio f of double-over-single capture for Sn^{3+} is determined to be $(11 \pm 4)\%$. The uncertainty in f is quite considerable due to the low intensities of the 9.7-eV H_f^+ and H_b^+ peaks. Peak areas for H_f^+ and H_b^+ are assessed by fitting Gaussian peaks to the spectrum while applying the following constraints: i) the positions and separation (223 ns) between the 9.7-eV H_f^+ and H_b^+ peaks are fixed; ii) the ratio of the 9.7-eV H_f^+ and H_b^+ peak areas is set to 1.3; and iii) the width of the H_f^+ peak is fixed at 1.5 times the width of the H_b^+ peak. The fitting constraints for the 9.7-eV H_f^+ and H_b^+ peaks, which were determined on basis of the N^{5+} and O^{6+} spectra, were also observed in numerous ToF measurements with other ions e.g. Xe^{4+}, Sn^{5+}, and Ar^{6+}.

2.2.5 Contributions of double collisions

Finally, it is checked that the experiments are performed in the single-collision regime by varying the target pressure over one order of magnitude. Figure 2.5 shows as an example the dependence of the measured beam current of Sn^{3+} as a function of target pressure. In the figure, the curves are generated by solving Eqs. (2.3) taking only the significant cross sections, i.e., σ_{32}, σ_{31}, and σ_{21}, into account. The measured σ_{32} and f are used as inputs in the calculations; the multiple curves correspond to calculations taking different input values of σ_{21}. From the figure, it is seen that deviations from the single-collision approximation might start to show up at pressures of 1.5×10^{-4} mbar depending on the magnitude of the cross section for single-electron capture (σ_{21}) by Sn^{2+}. The data in Figure 2.5 suggest a σ_{21} cross section of about 5×10^{-16} cm^2. As the data used for the final determination of the single-electron capture cross sections σ_{32} have been taken at 1.5×10^{-4} mbar, the influence of double collisions is very small and might have been neglected. Nevertheless, we have chosen to correct the data for double collisions assuming a common σ_{21} cross section of $(5 \pm 5) \times 10^{-16}$ cm^2. Such inclusion of double collisions reduces the uncorrected σ_{32} cross sections by $\approx 3\%$ on average.
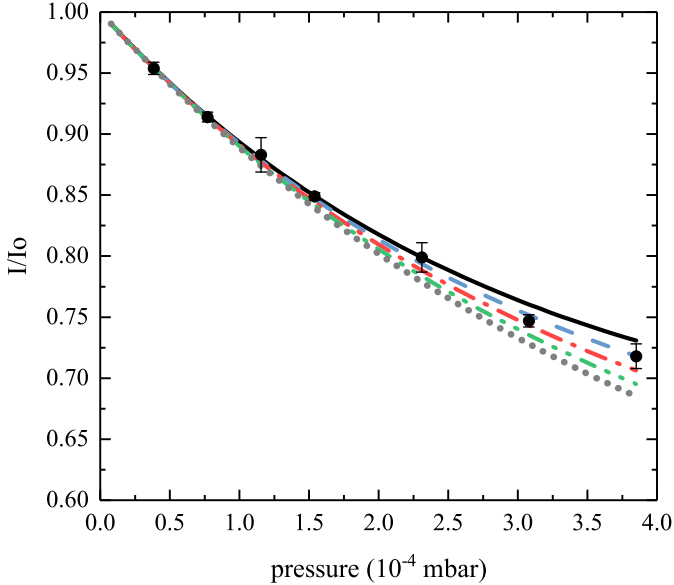
Figure 2.5: Comparison of the measured beam current of 39-keV Sn^{3+} ions (black symbols) as a function of the H$_2$ target pressure with simulated results (curves) taking different values for the σ_{21} cross section (Sn^{2+} → Sn^{1+}). For σ_{21}, the following cross sections are used (in units of 10^{-16} cm^2) for the lines of different colors and styles: black solid line = 0, blue dashed line = 2.5, red dashed-dotted line = 5, green dashed-dotted-dotted line = 7.5 and gray dotted line = 10.

2.3   Theory

We have calculated the SC cross sections using a semiclassical method with nuclear straight-line trajectories. The calculation assumes that the H–H internuclear distance, ρ, is fixed during the collision (Franck-Condon approximation). The electronic wave function has been expanded in terms of seven molecular functions of the SnH$_2^{3+}$ quasimolecule. The molecular wave functions are approximate eigenfunctions of the Born-Oppenheimer electronic Hamiltonian, obtained by means of a multireference configuration interaction method. In practice, the calculation explicitly considers the three valence electrons, which move in the field created by the H nuclei and the *ab initio* pseudopotential STUTTGART RLC ECP [44] that describes the electrons' interaction with the Sn^{4+} core. We have carried out the calculation of electronic wave functions by employing a three-center basis set of Gaussian-type-orbitals (GTO)
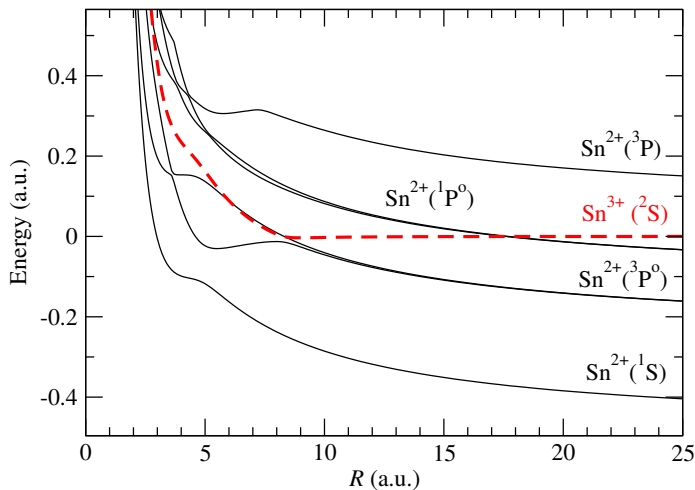
Figure 2.6: Potential energy curves of the $(Sn+H_2)^{3+}$ $^2A'$ electronic states as functions of the distance from the Sn nucleus to the midpoint of the H_2 axis. The spectroscopic terms of the Sn^{2+} or Sn^{3+} ions in the separate atom limit are indicated in the figure.

that includes the $(8s, 4p) \rightarrow [3s, 2p]$ basis [45] centered on the H nuclei and a $[4s, 4p, 3d, 2f]$ basis [46] on the Sn nucleus. In a first step, we have obtained a set of molecular orbitals (MOs) in a restricted Hartree-Fock calculation in this basis for the SnH_2^{3+} system, and we have created the configuration space by allowing single and double excitations from a set of eight reference configurations. The configuration space is restricted by allowing between one and three electrons in five MOs, the first four orbitals of A' symmetry and the first A'' MO. Up to two electrons can occupy the remaining orbitals. We have calculated the nonadiabatic couplings numerically as explained in Refs [47, 48] with a differentiation step of 10^{-4} a.u. The molecular expansion includes a common translation factor based on the switching function of Ref. [49].

The asymptotic energy differences between the entrance channel $Sn^{3+}(5s^1\,^2S)$ + $H_2(X\,^1\Sigma_g^+)$ and the exit channels $Sn^{2+}(5s^2\,^1S, 5s5p\,^3P^o, 5s5p\,^1P^o, 5p^2\,^3P)$ have been compared with NIST data [50], after subtracting the calculated ionization potential of H_2 at the equilibrium distance ($\rho = 1.4$ a.u.). The differences with the average energies of each multiplet are smaller than 0.03 a.u. In Figure 2.6, we show the energies of the seven lowest molecular states for a nuclear geometry with the angle between the vectors $\vec{R}$ ($\vec{R}$ is the position vector of the Sn nucleus with respect to the midpoint of the H–H internuclear axis) and $\vec{\rho}$ equal to $60°$, which has been found in previous calculations [51] to

be a representative geometry that leads to cross sections in good agreement with the orientation-averaged (OA) ones. In the nonrelativistic approach, only transitions to doublet states are allowed. Also, transitions to A'' are forbidden, and we have plotted only the energies of the molecular states $^2A'$. The energy of the entrance channel exhibits avoided crossings with those of the states dissociating into $Sn^{2+}(5s5p\,^1P^o)+H_2^+(X\,^2\Sigma_g^+)$ and $Sn^{2+}(5s5p\,^3P^o)+H_2^+(X\,^2\Sigma_g^+)$. The first one takes place at a very large distance, $R \approx 17.5$ a.u., and is very narrow. In practice, it is traversed diabatically, as plotted in Figure 2.6. At not too high collision energies, the transitions in the neighborhood of the second avoided crossing, $R \approx 8.5$ a.u., furnish the main mechanism of the electron capture process. As the collision energy increases, the transitions in the wide avoided crossing between the energies of the ground and the first excited state at $R \approx 5$ a.u., become more important, and are responsible for the population of the channel $Sn^{2+}(5s^2\,^1S)+H_2^+(X\,^2\Sigma_g^+)$.

The numerical solution of the eikonal equation leads to the probabilities for transitions to the different capture channels, $P_k(b)$ and the corresponding integral cross sections,

$$\sigma_k = 2\pi \int_0^\infty bP_k(b)\mathrm{d}b, \tag{2.8}$$

where b is the impact parameter.

In Figure 2.7 we plot the opacity functions, bP_k, for the electron capture into $Sn^{2+}(^1S)+H_2^+(X^2\Sigma_g^+)$, $Sn^{2+}(^3P^o)+H_2^+(X^2\Sigma_g^+)$ and $Sn^{2+}(^1P^o)+H_2^+(X^2\Sigma_g^+)$ for the collision energies of 250 eV/u and 500 eV/u. One can note that the charge transfer channel, $Sn^{2+}(^3P^o)+H_2^+(X^2\Sigma_g^+)$, is populated for relatively large impact parameters, which are coherent with the predicted transitions in the avoided crossing at $R \approx 8.5$ a.u. At these energies, the transitions near the avoided crossing between the two first energy curves give rise to the observed transitions at $b \lesssim 5.5$ a.u. to the electronic state dissociating in $Sn^{2+}(^1S)+H_2^+(X^2\Sigma_g^+)$, which are more important as E increases. On the contrary, the probabilities for capture to $Sn^{2+}(^3P^o)+H_2^+(X^2\Sigma_g^+)$ are less important as E increases, which corresponds to a more diabatic crossing of the avoided crossing near $R \approx 8.5$ a.u.

A more elaborate treatment of the orientation average is provided by the trajectory average where the energies and couplings are calculated along the projectile trajectory (see [29]). In the present case, we have carried out cross section calculations with three trajectory orientations as explained in Ref. [52].
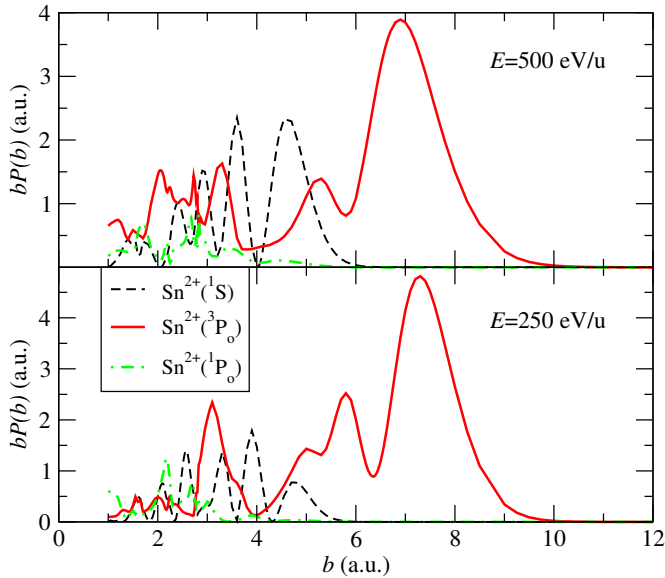
Figure 2.7: Opacity functions for the main three CX channels at $E = 250$ eV/u (bottom) and $E = 500$ eV/u (top).

2.4 Results and Discussion

The experimental results for Sn^{3+} colliding with H_2 are presented in Figure 2.8 (solid black dots). The measured cross sections range between $(25$–$50) \times 10^{-16}$ cm^2 and increase in magnitude with decreasing ion energy. For instance, on moving down from 0.43 keV/u to 0.08 keV/u in ion energy, the cross sections increase by a factor of ≈ 2. The cross sections are compared to our semiclassical calculations shown by the full black curve labeled OA in Figure 2.8. The experiments and the theory agree fairly well at higher energies but as one move towards lower impact energies, a discrepancy emerges. In the case of the calculated cross sections, the increase towards lower energy is much weaker with the cross-section increasing by only a factor of ≈ 1.2 on going down from 0.43 keV/u to 0.08 keV/u in impact energy. In search of the prospective cause of this discrepancy, experiments with the heavier isotopologue D_2 have been conducted, the results of which are given by the red solid squares in Figure 2.8. A remarkable isotope effect is observed in the experiments. Also, the calculations, which are independent of the molecular mass, evidently show better agreement (even at lower energies) with the experiments performed with D_2.
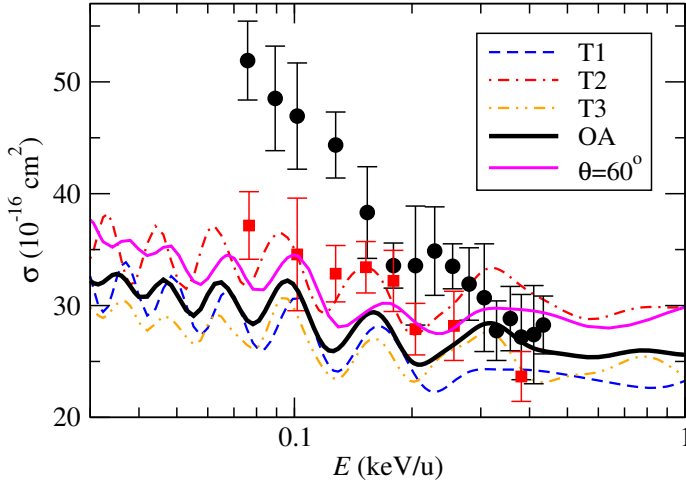
Figure 2.8: Comparison of experimental data with different semiclassical calculations of single electron capture cross sections in Sn^{3+} collisions with H$_2$ (black circles) and D$_2$ (red squares) as functions of the ion energy. The semiclassical results for the seven molecular states are obtained along three trajectory orientations (T1, T2, and T3) and their average (OA). The result of an isotropic calculation with the energies and couplings calculated for a fixed angle, 60°, between $\boldsymbol{v}$ and $\boldsymbol{\rho}$ is also included.

At relatively high impact energies, the main difficulty of the semiclassical calculation comes from the need to perform calculations for different orientations of the molecule with respect to the projectile trajectory or, equivalently, for different trajectory orientations with respect to a fixed molecule. We show in Figure 2.8 the cross sections calculated for three trajectory orientations (T1, T2, and T3), where T1 is a trajectory with $\boldsymbol{v} \parallel \boldsymbol{\rho}$ and $\boldsymbol{b} \perp \boldsymbol{\rho}$, T2 with $\boldsymbol{v} \perp \boldsymbol{\rho}$ and $\boldsymbol{b} \parallel \boldsymbol{\rho}$, and T3 with $\boldsymbol{v} \perp \boldsymbol{\rho}$ and $\boldsymbol{b} \perp \boldsymbol{\rho}$, with [52]

$$\sigma_{OA} = \frac{1}{3}\left[\sigma(\mathrm{T1}) + \sigma(\mathrm{T2}) + \sigma(\mathrm{T3})\right]. \tag{2.9}$$

In this system, the orientation effects are expected to be small because the main transitions take place at large internuclear separations. This is confirmed by the small differences between the three orientation-dependent results, and also between the OA cross section and that obtained using the energies and couplings calculated for $\theta = 60°$ ($\approx 6\%$). It can be noted in this figure that the oscillatory behavior of the cross section is similar in all calculations. The origin of these oscillations can be traced back to the interferences between transitions in the avoided crossing at $R \approx 8.5$ a.u. and those at $R \approx 3.6$ a.u.
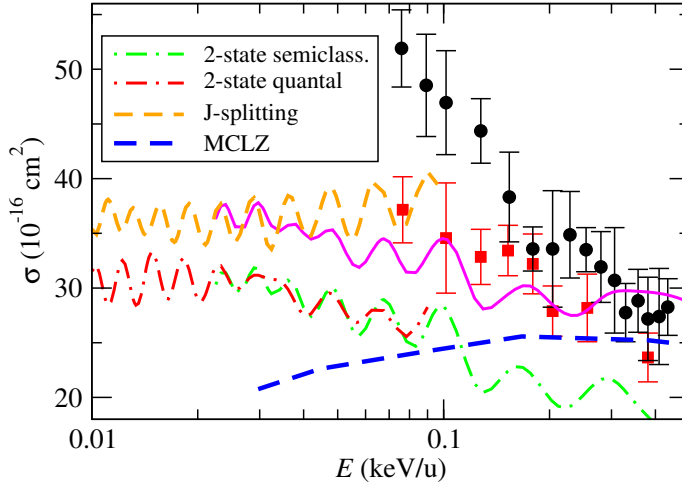
Figure 2.9: Comparison of the isotropic seven-state semiclassical calculation with $\theta = 60°$ (solid pink line) with a two-state quantal calculation and a two-state semiclassical calculation without rotational couplings (dashed-dotted lines). The dashed lines are the estimates including the effect of the L-S coupling (labeled J-splitting) in a four-state quantal calculation and in the Multi-Channel Landau-Zener (MCLZ) model. The experimental results are also included as in Figure 2.8.

(see Figure 2.6), which also appear in the calculations along the trajectories T1-T3. Since the transitions take place at relatively large values of R, the oscillations are similar and they do not disappear in the OA cross section.

The seven-state molecular calculation has been carried out within the framework of the semiclassical method, which may limit the validity of the calculation at relatively low collision energies. To estimate the limitation of this approximation, we have carried out exploratory full quantal calculations with a basis set of two molecular states, those involved in the avoided crossing at $R \approx 8.5$ a.u.: $Sn^{3+}(^2S)+H_2$ and $Sn^{2+}(^3P^o)+H_2^+(^2\Sigma_g^+)$. The semiclassical and the quantal two-state calculations show good agreement in the energy region $20 \text{ eV/u} < E < 100 \text{ eV/u}$ (Figure 2.9), which indicates that the differences found with the experimental values are not due to the use of the semiclassical formalism. In this respect, one must note that in the semiclassical method, the two molecular states are coupled by the two components of the nuclear gradient in the collision plane. However, in the quantal formalism (see [30]) only the component in the radial direction is included. In Figure 2.9, we have plotted the semiclassical cross section calculated without the coupling that comes from the gradient component perpendicular to the radial direction, which is identical

to the quantal one. Therefore, trajectory and quantal effects can be neglected in the energy range of the experiment.

A second approximation of the semiclassical calculation is the neglect of the spin-orbit coupling. An estimate of the influence of this effect is obtained in both the quantal and the Multi-Channel Landau-Zener (MCLZ) calculations with the Hamiltonian matrix elements given by the formulae of Ref. [53] and adding the asymptotic splitting of the $Sn^{2+}(^3P^o)$ term [50] to the diagonal matrix elements. The ensuing cross section has similar values to the experimental ones for $E > 0.2$ keV/u, but it decreases at lower energies. To further check this model, we have carried out a similar estimate by performing a four-state quantal calculation with the numerical H data previously employed in the two-state calculation and adding the asymptotic L-S splitting at all ion-molecule separations. At low energies, the cross section is dominated by transitions at large R to the highest state with $J = 2$ and it is increased with respect to that from the two-state calculation by up to 10%, because the avoided crossing is moved to a larger R as a consequence of the energy shift. For $E > 500$ eV/u (not shown in Figure 2.9), the model cross section shows an increase that is due to transitions to the lowest level ($J = 0$) that take place at smaller R, where the approximation of keeping the two-state interaction is not valid. We have also carried out a numerical experiment by integrating numerically the matrix elements of Ref. [53] with the asymptotic splitting, as in the MCLZ estimate. For the sake of clarity, the results are not included in Figure 2.9; they are similar to those using the numerical data, but without the oscillations, because the matrix elements of Ref. [53] do not include the modeling of the inner avoided crossing.

Finally, the increasing difference between the experimental cross sections for collisions with H_2 and D_2, as energy decreases, can be due to vibrational effects. In this respect, a similar isotopic dependency was found in the experiment of Kusakabe et al. [33] for $H^+ + (H_2, D_2)$. It is expected that the Franck-Condon calculation shows better agreement with D_2 data than with H_2 because it assumes that the target bond length remains fixed during the collision and this is a more realistic description for D_2 than for H_2, given that the larger reduced mass of the first is linked to a more localized initial vibrational wave function. Nevertheless, as the collision energy decreases, the vibrational effects will also start to be relevant for D_2 and we expect that the OA Franck-Condon calculation will not be valid for D_2 at energies below the experimental ones. Calculations of charge transfer beyond the Franck-Condon approximation [34] for $H^+ + (H_2, D_2)$ found indeed good agreement with experiments for both isotopic targets.

2.5 Conclusion

In this work we have presented both an experimental determination and a theoretical calculation of the absolute single electron capture cross section for Sn^{3+} on H_2 in the energy range 1–100 keV. The experiments are based on measuring a reduction in ion beam current due to the charge exchange interaction. The calculations are done in a semiclassical way using molecular orbitals. At the higher energies, there is a fair agreement between the experimentally determined and the theoretically calculated values. However, the experimental cross sections show a considerable increase towards lower energies, whereas this effect is only weakly present in the calculated values. Exploratory full quantal calculations have been performed and these show good agreement with the semiclassical calculations. From this, we conclude that the discrepancy is not due to the invalidity of the semiclassical approach in our energy regime. The effect of spin-orbit coupling has been found to be small ($\approx 15\%$) and it does not explain the rise of the cross section for the collision with H_2 at $E < 200$ eV/u. The experiments have also been performed for the heavier isotopologue D_2 and show a less strong increase of cross section towards the lower energies and are in good agreement with the semiclassical Franck-Condon calculations. This leads us to conclude that the increase for H_2 is due to vibrations in the target molecule. This effect is weaker in D_2 because of the higher mass and it is not included in the calculations, which make use of the Franck-Condon approximation.

2.6 Acknowledgements

References

[1]   R. Geller, "Electron cyclotron resonance sources: Historical review and future prospects (invited)", *Rev. Sci. Instrum.* **69**, 1302–1310 (1998).

[2]   R. K. Janev and H. Winter, "State-selective electron capture in atom-highly charged ion collisions", *Phys. Rep.* **117**, 265–387 (1985).

[3]   M. Barat and P. Roncin, "Multiple electron capture by highly charged ions at keV energies", *J. Phys. B: At. Mol. Opt. Phys* **25**, 2205 (1992).

[4]   W. Fritsch and C. D. Lin, "The semiclassical close-coupling description of atomic collisions: Recent developments and results", *Phys. Rep.* **202**, 1–97 (1991).

[5]   I. Čadež, J. B. Greenwood, J. Lozano, R. J. Mawhorter, M. Niimura, S. J. Smith, and A. Chutjian, "Absolute cross sections for single and double charge-exchange in Fe^{q+} impacting on He", *J. Phys. B: At. Mol. Opt. Phys.* **36**, 3303 (2003).

[6]   J. Simcic, D. R. Schultz, R. J. Mawhorter, I. Čadež, J. B. Greenwood, A. Chutjian, C. M. Lisse, and S. J. Smith, "Measurement and calculation of absolute single- and multiple-charge-exchange cross sections for Fe^{q+} ions impacting CO and CO$_2$", *Phys. Rev. A* **81**, 062715 (2010).

[7]   I. Y. Tolstikhina, M. S. Litsarev, D. Kato, M. Song, J. Yoon, and V. P. Shevelko, "Collisions of Be, Fe, Mo and W atoms and ions with hydrogen isotopes: Electron capture and electron loss cross sections", *J. Phys. B: At. Mol. Opt. Phys.* **47**, 035206 (2014).

[8]   V. I. Azarov and Y. N. Joshi, "Analysis of the 4d^7-4d^{6}5p transition array of the eighth spectrum of tin: Sn VIII", *J. Phys. B: At. Mol. Opt. Phys.* **26**, 3495 (1993).

[9]   R. D'Arcy, H. Ohashi, S. Suda, H. Tanuma, S. Fujioka, H. Nishimura, K. Nishihara, C. Suzuki, T. Kato, F. Koike, J. White, and G. O'Sullivan, "Transitions and the effects of configuration interaction in the spectra of Sn XV–Sn XVIII", *Phys. Rev. A* **79**, 042509 (2009).

[10] A. Windberger, F. Torretti, A. Borschevsky, A. Ryabtsev, S. Dobrodey, H. Bekker, E. Eliav, U. Kaldor, W. Ubachs, R. Hoekstra, J. R. Crespo López-Urrutia, and O. O. Versolato, "Analysis of the fine structure of Sn^{11+} - Sn^{14+} ions by optical spectroscopy in an electron-beam ion trap", *Phys. Rev. A* **94**, 012506 (2016).

[11] F. Torretti, A. Windberger, A. Ryabtsev, S. Dobrodey, H. Bekker, W. Ubachs, R. Hoekstra, E. V. Kahl, J. C. Berengut, J. R. Crespo López-Urrutia, and O. O. Versolato, "Optical spectroscopy of complex open-4d-shell ions Sn^{7+}- Sn^{10+}", *Phys. Rev. A* **95**, 042503 (2017).

[12] J. Scheers, C. Shah, A. Ryabtsev, H. Bekker, F. Torretti, J. Sheil, D. A. Czapski, J. C. Berengut, W. Ubachs, J. R. Crespo López-Urrutia, R. Hoekstra, and O. O. Versolato, "EUV spectroscopy of highly charged Sn^{13+}-Sn^{15+} ions in an electron-beam ion trap", *Phys. Rev. A* **101**, 062511 (2020).

[13] N. R. Badnell, A. Foster, D. C. Griffin, D. Kilbane, M. O'Mullane, and H. P. Summers, "Dielectronic recombination of heavy species: the tin $4p^6 4d^q$ - $4p^6 4d^{(q-1)} 4f$ + $4p^5 4d^{(q+1)}$ transition arrays for q = 1-10", *J. Phys. B: At. Mol. Opt. Phys.* **44**, 135201 (2011).

[14] A. Borovik Jr, M. F. Gharaibeh, P. M. Hillenbrand, S. Schippers, and A. Müller, "Detailed investigation of electron-impact single-ionization cross sections and plasma rate coefficients of N-shell tin ions", *J. Phys. B: At. Mol. Opt. Phys.* **46**, 175201 (2013).

[15] G. G. van Eden, T. W. Morgan, D. U. B. Aussems, M. A. van den Berg, K. Bystrov, and M. C. M. van de Sanden, "Self-Regulated Plasma Heat Flux Mitigation Due to Liquid Sn Vapor Shielding", *Phys. Rev. Lett.* **116**, 135002 (2016).

[16] R. E. Nygren and F. L. Tabarés, "Liquid surfaces for fusion plasma facing components—A critical review. Part I: Physics and PSI", *Nucl. Mater. Energy* **9**, 6–21 (2016).

[17] G. G. van Eden, V. Kvon, M. C. M. van de Sanden, and T. W. Morgan, "Oscillatory vapour shielding of liquid metal walls in nuclear fusion devices", *Nat. Commun.* **8**, 1–10 (2017).

[18] G. O'Sullivan, B. Li, R. D'Arcy, P. Dunne, P. Hayden, D. Kilbane, T. McCormack, H. Ohashi, F. O'Reilly, P. Sheridan, E. Sokell, C. Suzuki, and T. Higashiguchi, "Spectroscopy of highly charged ions and its relevance to EUV and soft X-ray source development", *J. Phys. B: At. Mol. Opt. Phys.* **48**, 144025 (2015).

[19] W. Svendsen and G. O'Sullivan, "Statistics and characteristics of xuv transition arrays from laser-produced plasmas of the elements tin through iodine", *Phys. Rev. A* **50**, 3710–3718 (1994).

[20] V. Bakshi (ed), *EUV lithography*, 2nd edn, Bellingham, WA: SPIE Press, 2018.

[21] O. O. Versolato, "Physics of laser-driven tin plasma sources of EUV radiation for nanolithography", *Plasma Sources Sci. Technol.* **28**, 083001 (2019).

[22] V. Y. Banine, K. N. Koshelev, and G. H. P. M. Swinkels, "Physical processes in EUV sources for microlithography", *J. Phys. D: Appl. Phys.* **44**, 253001 (2011).

[23] I. Fomenkov, D. Brandt, A. Ershov, A. Schafgans, Y. Tao, G. Vaschenko, S. Rokitski, M. Kats, M. Vargas, M. Purvis, R. Rafac, B. L. Fontaine, S. D. Dea, A. LaForge, J. Stewart, S. Chang, M. Graham, D. Riggs, T. Taylor, M. Abraham, and D. Brown, "Light sources for high-volume manufacturing EUV lithography: technology, performance, and power scaling", *Adv. Opt. Techn.* **6**, 173–186 (2017).

[24] F. Torretti, J. Sheil, R. Schupp, M. M. Basko, M. Bayraktar, R. A. Meijer, S. Witte, W. Ubachs, R. Hoekstra, O. O. Versolato, A. J. Neukirch, and J. Colgan, "Prominent radiative contributions from multiply-excited states in laser-produced tin plasma for nanolithography", *Nat. Commun.* **11**, 1–8 (2020).

[25] A. Bayerle, M. J. Deuzeman, S. van der Heijden, D. Kurilovich, T. de Faria Pinto, A. Stodolna, S. Witte, K. S. E. Eikema, W. Ubachs, R. Hoekstra, and O. O. Versolato, "Sn ion energy distributions of ns-and ps-laser produced plasmas", *Plasma Sources Sci. Technol.* **27**, 045001 (2018).

[26] D. J. Hemminga, L. Poirier, M. M. Basko, R. Hoekstra, W. Ubachs, O. O. Versolato, and J. Sheil, "High-energy ions from Nd:YAG laser ablation of tin microdroplets: comparison between experiment and a single-fluid hydrodynamic model", *Plasma Sources Sci. Technol.* **30**, 105006 (2021).

[27] L. Poirier, A. Bayerle, A. Lassise, F. Torretti, R. Schupp, L. Behnke, Y. Mostafa, W. Ubachs, O. O. Versolato, and R. Hoekstra, "Cross-calibration of a combined electrostatic and time-of-flight analyzer for energy-and charge-state-resolved spectrometry of tin laser-produced plasma", *Appl. Phys. B* **128** (2022).

[28] R. F. Welton, T. F. Moran, and E. W. Thomas, "Metastable state abundances in multiply charged ion beams", *J. Phys. B: At. Mol. Opt. Phys.* **24**, 3815–3823 (1991).

[29] I. Rabadán and L. Méndez, "Orientation effects in ion-molecule collisions", *J. Phys.: Conf. Ser.* **875**, 012009 (2017).

[30] X. Urbain, N. de Ruette, V. M. Andrianarijaona, M. F. Martin, L. Fernández Menchero, L. F. Errea, L. Méndez, I. Rabadán, and B. Pons, "New Light Shed on Charge Transfer in Fundamental H$^+$ + H$_2$ Collisions", *Phys. Rev. Lett.* **111**, 203201 (2013).

[31] G. W. McClure, "Electron transfer in proton-hydrogen-atom collisions: 2-117 keV", *Phys. Rev.* **148**, 47–54 (1966).

[32] Y. Nakai, T. Shirai, T. Tabata, and R. Ito, "Cross sections for charge transfer of hydrogen atoms and ions colliding with gaseous atoms and molecules", *At. Data Nucl. Data Tables* **37**, 69–101 (1987).

[33] T. Kusakabe, L. Pichl, R. J. Buenker, M. Kimura, and H. Tawara, "Isotope effect in charge-transfer collisions of slow H$^+$ and D$^+$ ions with H$_2$, HD, and D$_2$ molecules", *Phys. Rev. A* **70**, 052710 (2004).

[34] L. F. Errea, L. Fernández, L. Méndez, B. Pons, I. Rabadán, and A. Riera, "Vibronic treatment of vibrational excitation and electron capture in H$^+$ + H$_2$ (HD, D$_2$, ...) collisions at low impact energies", *Phys. Rev. A* **75**, 032703 (2007).

[35] S. Martínez, G. Bernardi, P. Focke, A. D. González, and S. Suárez, "H$_2$ dissociation by H$^+$ and He^{2+} projectiles at intermediate energies", *J. Phys. B: At. Mol. Opt. Phys.* **36**, 4813–4826 (2003).

[36] H. O. Folkerts, F. W. Bliek, M. C. de Jong, R. Hoekstra, and R. Morgenstern, "Dissociation of CO induced by ions: I. Fragmentation and kinetic energy release spectra", *J. Phys. B: At. Mol. Opt. Phys.* **30**, 5833 (1997).

[37] D. H. Crandall, M. L. Mallory, and D. C. Kocher, "Charge exchange between multicharged ions of C, N, and O and molecular hydrogen", *Phys. Rev. A* **15**, 61–69 (1977).

[38] D. Dijkkamp, D. Ciric, E. Vileg, A. de Boer, and F. J. de Heer, "Subshell-selective electron capture in collisions of C^{4+}, N^{5+}, O^{6+} with H, H_2 and He", *J. Phys. B: Atom. Mol. Phys.* **18**, 4763–4793 (1985).

[39] M. Mack and A. Niehaus, "Radiative and Auger decay channels in K-Shell excited Li-like ions (Z = 6–8)", *Nucl. Instrum. Methods Phys. Res., Sect. B* **23**, 109–115 (1987).

[40] M. Mack, "Electron spectroscopy in collisions with multiply charged ions", *Nucl. Instrum. Methods Phys. Res., Sect. B* **23**, 74–85 (1987).

[41] R. A. Phaneuf, I. Alvarez, F. W. Meyer, and D. H. Crandall, "Electron capture in low-energy collisions of C^{q+} and O^{q+} with H and H_2", *Phys. Rev. A* **26**, 1892–1906 (1982).

[42] G. Lubinski, Z. Juhász, R. Morgenstern, and R. Hoekstra, "State-selective electron-capture cross section measurements for low-energy collisions of He-like ions on H_2", *J. Phys. B: At. Mol. Opt. Phys.* **33**, 5275–5296 (2000).

[43] J. R. Machacek, D. P. Mahapatra, D. R. Schultz, Y. Ralchenko, A. Chutjian, J. Simcic, and R. J. Mawhorter, "Measurement and calculation of absolute single- and double-charge-exchange cross sections for O^{6+} ions at 1.17 and 2.33 keV/u impacting He and H_2", *Phys. Rev. A* **90**, 052708 (2014).

[44] A. Bergner, M. Dolg, W. Küchle, H. Stoll, and H. Preuß, "Ab-initio energy-adjusted pseudo potentials for elements of groups 13–17", *Mol. Phys.* **80**, 1431–1441 (1993).

[45] P.-O. Widmark, P.-Å. Malmqvist, and B. O. Roos, "Density matrix averaged atomic natural orbital (ANO) basis sets for correlated molecular wave functions", *Theor. Chim. Acta* **77**, 291 (1990).

[46] J. M. L. Martin and A. Sundermann, "Correlation consistent valence basis sets for use with the Stuttgart–Dresden–Bonn relativistic effective core potentials: The atoms Ga–Kr and In–Xe", *J. Chem. Phys.* **114**, 3408–3420 (2001).

[47] J. F. Castillo, L. F. Errea, A. Macías, L. Méndez, and A. Riera, "Ab initio calculation of nonadiabatic couplings using MELD", *J. Chem. Phys.* **103**, 2113–2116 (1995).

[48] L. F. Errea, L. Fernández, A. Macías, L. Méndez, I. Rabadán, and A. Riera, "Sign-consistent dynamical couplings between ab initio three-center wave functions", *J. Chem. Phys.* **121**, 1663–1669 (2004).

[49] L. F. Errea, L. Méndez, and A. Riera, "On the choice of translation factors for approximate molecular wavefunctions", *J. Phys. B: At. Mol. Phys.* **15**, 101–110 (1982).

[50]   A. Kramida, Y. Ralchenko, J. Reader, and NIST ASD Team, NIST Atomic Spectra Database (ver. 5.3), [Online]. Available: `http://physics.nist.gov/asd`. National Institute of Standards and Technology, Gaithersburg, MD. 2015.

[51]   L. F. Errea, A. Macías, L. Méndez, I. Rabadán, and A. Riera, "Anisotropy effects in H$^+$+H$_2$ collisions", *Int. J. Mol. Sci.* **3**, 142–161 (2002).

[52]   L. F. Errea, J. D. Gorfinkiel, A. Macías, L. Méndez, and A. Riera, "Implementation of the sudden approximation eikonal method in ion - diatom collisions", *J. Phys. B: At. Mol. Opt. Phys.* **30**, 3855–3872 (1997).

[53]   M. Kimura, T. Iwai, Y. Kaneko, N. Kobayashi, A. Matsumoto, S. Ohtani, K. Okuno, S. Takagi, H. Tawara, and S. Tsurubuchi, "Landau-Zener Model Calculations of One-Electron Capture from He Atoms by Highly Stripped Ions at Low Energies", *J. Phys. Soc. Jpn.* **53**, 2224–2232 (1984).

Evidence of production of keV Sn$^+$ ions in the H$_2$ buffer gas surrounding an Sn-plasma EUV source

Abstract

Charge-state-resolved kinetic energy spectra of Sn ions ejected from a laser-produced plasma (LPP) of Sn have been measured at different densities of the H$_2$ buffer gas surrounding a micro-droplet LPP. In the absence of H$_2$, energetic keV Sn ions with charge states ranging from 4+ to 8+ are measured. For the H$_2$ densities used in the experiments no appreciable stopping or energy loss of the ions is observed. However, electron capture by Sn ions from H$_2$ results in a rapid shift towards lower charge states. At the highest H$_2$ pressure of 6×10^{-4} mbar, only Sn^{2+} and Sn$^+$ ions are measured. The occurrence of Sn$^+$ ions is remarkable due to the endothermic nature of electron capture by Sn^{2+} ions from H$_2$. To explain the production of keV Sn$^+$ ions, it is proposed that their generation is due to electron capture by metastable Sn^{2+*} ions. The gateway role of metastable Sn^{2+*} is underpinned by model simulations using atomic collision cross sections to track the charge states of Sn ions while traversing the H$_2$ buffer gas.

3.1   Introduction

Sources of extreme ultraviolet (EUV) light are based on laser-produced plasma (LPP) of high temperatures (up to 50 eV) and high free electron densities (10^{19-21} cm^{-3}) in which highly charged ions are produced that are the atomic sources of the EUV radiation [1, 2]. For nanolithographic tools, the EUV wavelength of choice is 13.5 nm, which is dictated by the existence of high reflectivity multilayer optics [3, 4]. The element of choice for plasma generation of 13.5 nm radiation is Sn. Over a broad range of charge states (9+ to 15+), singly, doubly, and triply excited electronic configurations emit around 13.5 nm [5].

Subsequent to the desired production of EUV radiation, the plasma expands and generates energetic Sn ions [6], which if impacting on the EUV collector optics may affect the lifetime of the optics. The energy and charge state distributions of Sn ions coming from the LPP contain information on the expansion dynamics of the plasma itself [7–11]. Moreover, accurate data on the energy distributions facilitate the determination of the fraction of the total energy that is carried by the plasma ions [12].

Typically, the energy spectrum of the emitted Sn ions peaks at a few keV with tails that may extend to tens of keV [11], except for Sn$^+$ and Sn^{2+} which are barely observed at higher energies above 0.5 keV. When an LPP is embedded in a stopping gas, only low-charged Sn ions are observed at much lower energies, which is a direct signature of charge exchange and collisional stopping, energy transfer from the Sn particles to the stopping gas. In this paper, we address the initial stage of the charge and energy redistribution in which charge exchange is active but the energy loss to the stopping gas is still negligible. This separation can be made if the cross sections for charge exchange are much larger than the ones for significant kinetic-energy transfer. For Sn^{q+} ions with $q \geq 3$ this assumption is not debated but in the case of 1+ and 2+ ions, the charge transfer cross sections for the reactions

$$\text{Sn}^{2+} + \text{H}_2 \rightarrow \text{Sn}^+ + \text{H}_2^+, \tag{3.1}$$

and

$$\text{Sn}^+ + \text{H}_2 \rightarrow \text{Sn} + \text{H}_2^+, \tag{3.2}$$
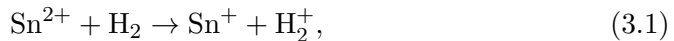
are conventionally expected to be negligible because of the low scaled kinetic energies of the Sn ions ($\ll$ 100 eV/u) and the considerable endothermicity of the reactions. The Franck Condon ionization potential of H$_2$ is 16.1 eV [13,

14], while the ionization potentials of Sn^+ and Sn are 14.6 eV and 7.3 eV [15], respectively. Thus, resonant electron capture by Sn^{2+} is endothermic by 1.5 eV and in the case of Sn^+ by no less than 8.7 eV.

Remarkable enough while indeed no appreciable signs of charge transfer by singly charged Sn ions (Eq. 3.2) are found we will show an efficient production of Sn^+ ions out of the population of doubly charged Sn ions. Based on all available data the case is made that the Sn^+ ions are produced by electron capture by metastable Sn^{2+*} ions in the excited $[Kr]4d^{10}5s5p$ ^3P_J levels (the ground state of Sn^{2+} is $[Kr]4d^{10}5s^2$ $^1S_0$).

From an EUV source perspective, the actual abundances of singly and doubly charged Sn ions and thus, whether Sn^{2+} ions get converted by electron capture into Sn^+, impacts the Sn ion mitigation because the penetration depth of the Sn ions into the H_2 buffer gas depends on the stopping cross sections. Recent stopping measurements [16] hint at appreciably larger stopping powers for Sn^+ than for Sn^{2+} ions.

This paper is organized as follows. First, the laser-produced plasma source installed at ARCNL is briefly introduced with emphasis on the methods used to measure the charge-state dependent energy distributions of Sn^{q+} ions coming from the expanding LPP plasma. Thereafter the energy distributions as a function of the H_2 buffer gas are presented with a focus on the Sn^+ ions, which present the evidence of the occurrence of charge exchange by Sn^{2+} ions. Finally based on potential-energy curves and Landau-Zener type calculations it is discussed that electron capture from H_2 by metastable $Sn^{2+*}(^3P_J)$ ions is exothermic and likely to happen given the effective production of metastable $Sn^{2+*}(^3P)$ in collisions of Sn^{3+} on H_2.

3.2 Experiment: methodology and data

The LPP EUV source used for the present set of experiments has been described in detail before [17]. The parts and features most relevant to this work are briefly recalled here. A tin reservoir, which is kept at a temperature of 260°C, is mounted on top of a vacuum chamber with a background vacuum of 10^{-7} mbar. In the H_2 buffer gas runs, molecular hydrogen pressures covering the range from 6×10^{-5} to 6×10^{-4} mbar have been used. At a repetition rate of 25 kHz droplets of pure, molten tin are pushed through a nozzle into the vacuum chamber. The stream of microdroplets with a diameter of 27 μm, first traverse a light sheet generated by a He-Ne laser. After frequency down-conversion to 10 Hz, the light scattered off the Sn droplets is used to trigger a 10-Hz Nd:YAG laser which creates the Sn plasma. The Nd:YAG laser system is operated at a
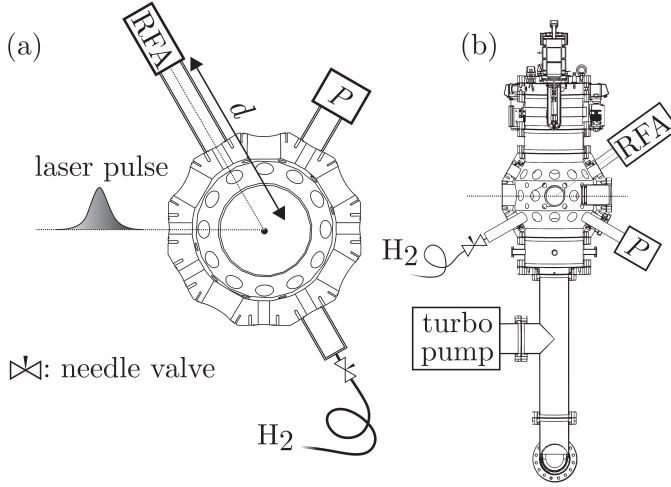
Figure 3.1: Schematic ((a): top view, (b): side view) of the LPP experiment to measure charge-state-specific ion spectra as a function of the pressure of the H_2 buffer gas embedding the LPP plasma. The distance d from plasma to the RFA type ion detector is 68.5 cm.

wavelength of 1064 nm and produces pulses of approximately 10 ns full-width at half-maximum (FWHM). The spatial beam profile is Gaussian and is focused to a spot size of 100 μm FWHM onto the droplets in the center of the chamber. A laser pulse energy of 200 mJ yielding a power density of 3×10^{11} W cm^{-2} has been used in all experimental data presented in the following.

The energy distributions of the Sn^{q+} ions from the LPP are measured with a retarding field analyzer (RFA), more specifically a 4-grid Kimball Physics FC-73 RFA. The RFA is positioned at a distance of 68.5 cm from the LPP and at an angle of 64° with respect to the laser beam as illustrated in Figure 3.1. The RFA is absolutely calibrated against an open, grid-less Faraday cup [18] to establish the integral transmission of the four grids. The same "bottom-up" method as introduced by Poirier *et al.* [19] is used to extract the kinetic-energy distributions for each individual charge state of tin ions from their joint overlapping energy distributions.

To interpret the ion energy spectra as a function of the H_2 pressure, one needs to know the relation between the pressure measured at the pressure gauge and the pressure (H_2 density) along the ions' trajectory from the LPP to the ion detector. With the Monte-Carlo package MOLFLOW+ [20] developed at CERN, we have calculated the H_2 density within the entire LPP vacuum
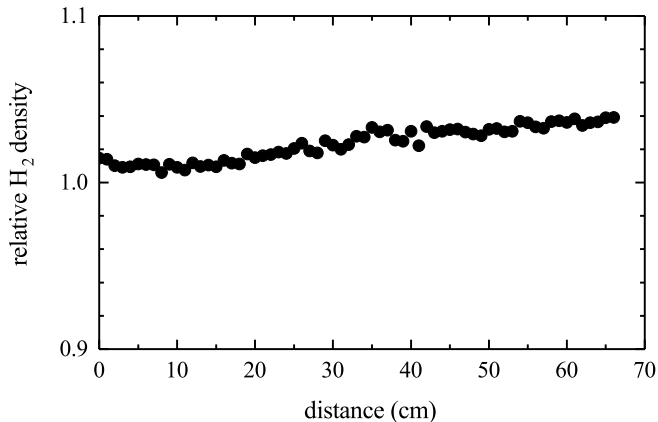
Figure 3.2: MOLFLOW+ Monte Carlo simulation results of the relative H_2 density, with respect to the density at the position of the pressure gauge, along the trajectory of Sn^{q+} ions flying from the laser-produced plasma in the center of the vacuum chamber to the RFA detector, positioned at 68.5 cm from that center.

chamber and all its additional vacuum tubing and equipment. The results of this simulation are shown in Figure 3.2. Along the ion path, the average relative H_2 density is seen to be just 3% higher than the density at the position of the pressure gauge and to change by a few percent only over the full distance of 68.5 cm. Therefore, taking a constant density along the ions' trajectory does not introduce significant errors when calculating charge state distributions along those trajectories. The largest uncertainty will stem from the absolute H_2 density calibration of the pressure gauge, which is given by the manufacturer as 30%.

The energy distributions for all eight charge states are presented in Figure 3.3 for five different H_2 pressures. Sn ions in charge states up to 8+ are observed in the RFA measurements. Note that the results labeled 10^{-6} mbar are the reference measurements with no H_2 gas surrounding the LPP plasma. The main points to be noted are that the spectra of Sn^{8+}, Sn^{7+}, and Sn^{6+} are rather narrow, peak at approximately 2 keV, and disappear with increasing H_2 pressure. In the absence of H_2 gas (grey spectra in Figure 3.3) the spectra of Sn^{3+}, Sn^{2+}, and Sn^+ are seen to extend to maximum kinetic energies of 1 keV for Sn^{3+} and ≈ 0.7 keV for Sn^{2+} and Sn^+. With increasing H_2 pressure a peak at 2 keV, similar to the 2-keV peak characterizing the Sn^{8+}, Sn^{7+}, and Sn^{6+} spectra, grows in into the Sn^{3+}, Sn^{2+}, and Sn^+ spectra. Therefore the keV ions of Sn^{3+}, Sn^{2+}, and Sn^+ observed in the energy spectra taken with a
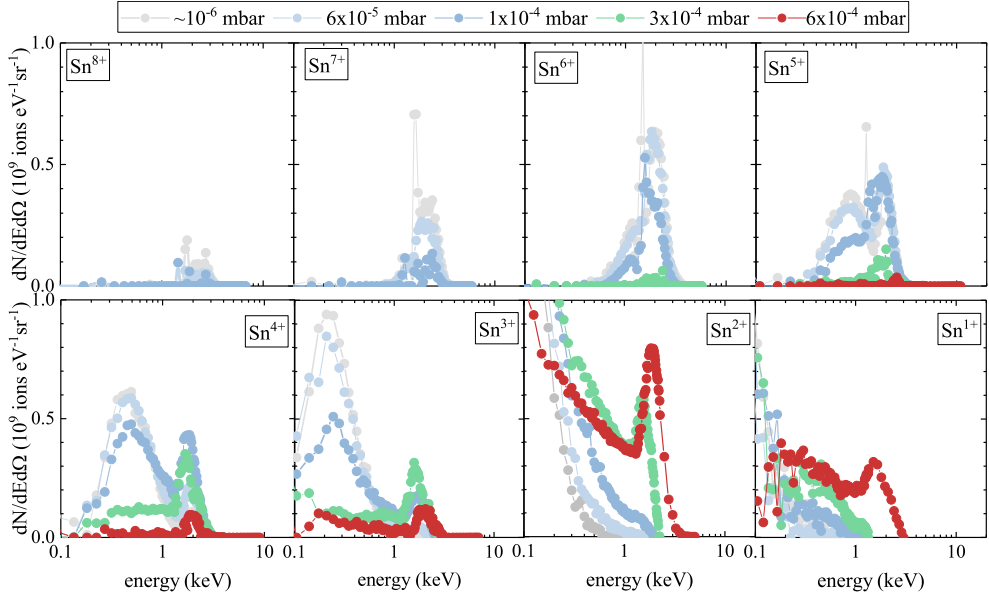
Figure 3.3: The yield of Sn^{q+} ions as a function of their kinetic energy in case of no H$_2$ gas and for H$_2$ buffer gas pressures in the range 6×10^{-5} to 6×10^{-4} mbar. The ions' flight path through the buffer gas is 68.5 cm.

H$_2$ stopping gas around the LPP plasma must originate from Sn^{q+} ions with $q \geq 4$ by means of consecutive electron capture reactions. Last but not least, the emergence of energetic (E $\geq$ 1 keV) Sn$^+$ ions with increasing H$_2$ pressure is a clear sign that one-electron capture by Sn^{2+} (Eq. 3.1) is not blocked by an anticipated endothermicity of the reaction and moreover even has a significant cross section.

3.3   Discussion

Before addressing the above points, one should realize that from an industrial source perspective, our experiments are performed at pressures representing the initial stages of the trajectories of Sn ions in the H$_2$ stopping gas after being ejected from the plasma. In this first phase, charge-exchange processes lower the average charge state of the ions rapidly before the ions have undergone appreciable energy loss. The validity of this approximation is implicit in the charge-state dependent energy spectra shown in Figure 3.3 where the high energy peak is seen to remain at 2 keV whilst the charge state of the high
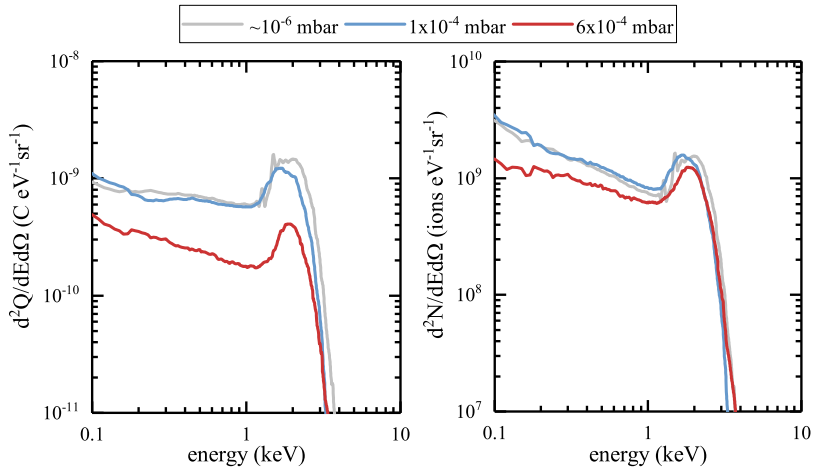
Figure 3.4: Left panel: Total amount of charge as a function of Sn ion energy. Right panel: Total number of ions as a function of Sn ion energy. Results are presented for no H_2 buffer gas present (labeled $\sim 10^{-6}$ mbar) and buffer gas pressures of 1×10^{-4} and 6×10^{-4} mbar. The path length through the buffer gas is 68.5 cm.

energy ions decreases.

The reduction of average charge state without significant energy loss is illustrated in Figure 3.4. This figure shows in its left panel the cumulative charge as a function of energy, while the right panel presents the number of particles as a function of energy. In the peak range (1–5 keV) the amount of charge measured at the RFA drops by approximately a factor of 4 when the H_2 pressure is raised to 6×10^{-4} mbar. In contrast to that the number of Sn ions having energies above 1 keV has not changed appreciably. The assumption that initially, charge transfer processes dominate over stopping and determine the changes in the charge-state dependent energy distributions therefore appears valid.

The pressure dependence of the particle-number distributions for all charge states from $q = 8$ down to $q = 1$ can be tracked by a set of eight differential equations of the type:

$$\frac{dN^{q+}}{dl} = n\sigma_{q+1 \rightarrow q}N^{(q+1)+} - n\sigma_{q \rightarrow q-1}N^{q+}, \qquad (3.3)$$

with N^{q+} the number of Sn ions in charge state $q+$, n the H_2 target density, $\sigma_{q \rightarrow q-1}$ the cross section for charge exchange from charge state $q+$ to $(q-1)+$,
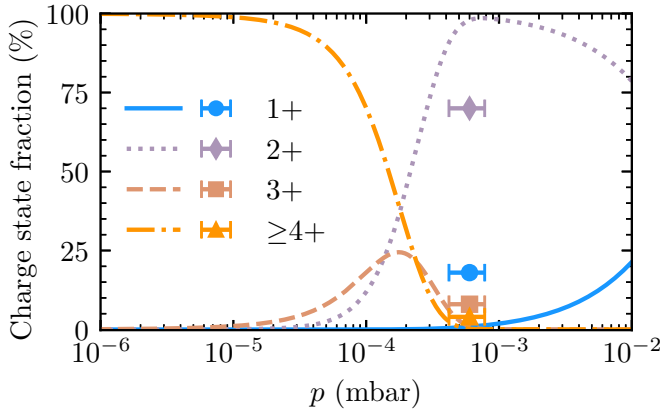
Figure 3.5: Simulated charge state fractions of energetic Sn^{q+} ions detected at a distance of 68.5 cm from the LPP plasma as a function of H$_2$ buffer pressure. For $q \geq 4$ the actual q specific fractions as measured at p=10^{-6} mbar (see Figure 3.3) were used as input in solving the set of differential equations (Eq. 3.3). Solid points show the experimental LPP data.

and l the position along the ion's trajectory. With the exception of Sn^{3+} [21] (Chapter 2), no charge exchange data is available for Sn^{q+} ions colliding on H$_2$. Therefore we decided to use the classical over-the-barrier model [22–24] to calculate estimates for $\sigma_{q \to q-1}$ cross sections for charge states $q \geq 4$ and which are found to be 62, 76, 88, 100, and 112 ($\times 10^{-16}$ cm^2) for 4+, 5+, 6+, 7+, and 8+ Sn ions, respectively. Cross sections obtained with the over-the-barrier model present typically an upper-limit cross section as the model assumes that for impact parameters smaller than a specific distance capture happens with 100% probability. For endothermic charge-transfer reactions cross sections are very small at low energies [25, 26], typically much smaller than 10^{-16} cm^2. To illustrate the contribution of a non-zero cross section for Sn^{2+} ions a cross section of 0.1$\times 10^{-16}$ cm^2 has been used in the simulations. The results of a particle-number simulation are shown in Figure 3.5. In line with the experimental data for energetic Sn ions ($E \geq 1$ keV) (see Figure 3.3) the charge-state fractions of energetic Sn ions swap from $q \geq 4$ to $q < 3$ over the pressure range of 10^{-4} to 10^{-3} mbar. In contrast to the experimental data, which show a considerable (20%) fraction of 1+ ions at a pressure of 6$\times 10^{-4}$ mbar, barely any Sn$^+$ ions are predicted. To obtain large Sn$^+$ populations matching the experimental data, a much larger cross section of order 10^{-15} cm^2 is required.

For an electron-capture reaction to have a large cross-section, the potential
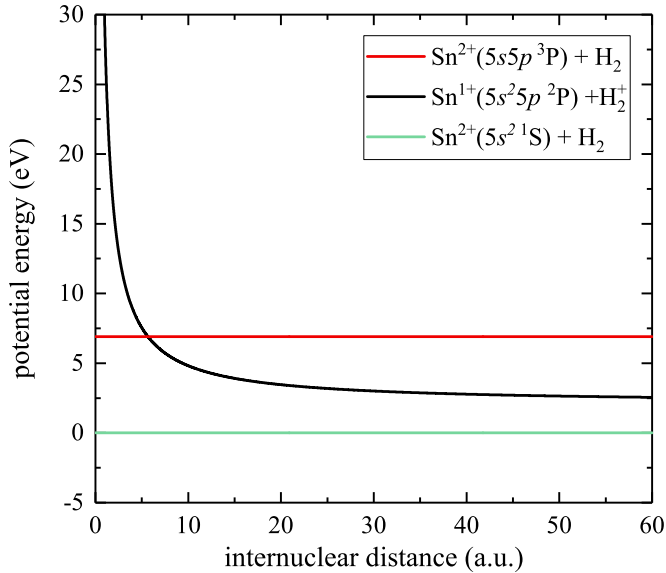
Figure 3.6: Schematic potential energy curves of relevant electronic channels in $Sn^{2+} - H_2$ collisions as a function of the internuclear distance between the Sn^{2+} ion and the H_2 molecule which is considered to be a point-like particle.

energy curves of the initial and final channels are required to cross one another at an internuclear distance between the ion and the target particle on the order of 10 a.u. A simplified picture, including only the Coulomb repulsion in the $Sn^+ - H_2^+$ exit channel, of the most relevant potential energy curves for $Sn^{2+} - H_2$ collisions is shown in Figure 3.6.

In Figure 3.6, the electronic potential energy of ground state $Sn^{2+}(5s^2 \ ^1S)$ and H_2 is taken as reference for all other channels. As mentioned in the introduction the electron-capture channel $Sn^+(5s^2 5p \ ^2P) + H_2^+$ is endothermic by 1.5 eV at infinite internuclear distance between the particles. At shorter distances, due to the Coulomb repulsion between Sn^+ and H_2^+ the difference between both curves increases, and thus both potential energy curves do not cross underpinning the original idea of resonant electron capture from H_2 by ground state $Sn^{2+}(5s^2 \ ^1S)$ not being possible.

For metastable $Sn^{2+}(5s5p \ ^3P)$ ions (Sn^{2+*}) the situation is very different. The $5s5p \ ^3P$ term lies about 7 eV (weighted average of the excitation energies of the $J = 0$, 1, and 2 levels of 6.64, 6.84, 7.34 eV, respectively [15]) above the ground state. Therefore at an internuclear distance R_c, there exists a curve crossing with the electron capture channel near 6 a.u., cf. Figure 3.6. Using

this distance, one might estimate using the 'absorbing sphere' approximation [27, 28] a maximum cross section of 1.4×10^{-15} cm^2 ($= 0.45 \, \pi \, R_c^2$). This cross section is of similar order of magnitude as the one for Sn$^{3+}-$ H$_2$ collisions [21], which indicates that one-electron capture by metastable Sn^{2+} ions is a potential gateway to produce singly charged Sn$^+$ ions.

Metastable Sn^{2+*} ions as a source for the production of Sn$^+$ ions by means of electron capture obviously requires large abundances of metastable Sn^{2+*} ions. In our earlier work on charge exchange in Sn^{3+} on H$_2$ [21], semiclassical calculations showed that electron capture populates directly, and at energies of a few keV almost solely ($\gg 95\%$), the metastable Sn$^{2+}(5s5p \, ^3$P) term. The latter point of the very high state selectivity of charge transfer in 1 to 10 keV Sn^{3+} on H$_2$ collisions was not explicitly discussed in that paper because then we focused on 10 to 100 keV collision energies. The predominant population of only one term is in line with existing data on other collision systems, all showing that at low energies well below 1 keV/u charge exchange becomes extremely state selective with a single state carrying almost all of the charge exchange cross section, e.g. [29–32]. As shown above, all keV Sn ions of high charge state get rapidly converted to Sn^{3+} ions and which, by subsequent charge transfer, create metastable Sn^{2+*} ions. Metastable Sn^{2+*} are therefore abundantly produced in the stopping gas.

Transitions from the populated metastable $5s5p \, ^3$P$_{0,1,2}$ levels to the ground state $5s^2 \, ^1$S are spin forbidden. However, how long are their lifetimes with respect to the time between subsequent collisions? For $J=0$ and $J=2$, the transitions are also symmetry forbidden and thus the levels are expected to be very long-lived. While $J=0$ to $J'=0$ are truly forbidden, $J=2$ to $J'=0$ transitions still exhibit small transition probabilities [33]. To get an order of magnitude estimate of the lifetime of the Sn$^{2+}5s5p \, ^3$P$_2$ level, we performed a basic FAC (Flexible Atomic Code [34]) calculation. The calculation predicts a lifetime of the order of 10-100 s. This lifetime is very long compared to typical flight times in the experiment which are in the range of a few to a few tens of μs. For a heavy species such as Sn where the spin-orbit coupling is very significant, the $J=1$ level is expected to have by far the shortest lifetime of the three levels of the ^{3}P term as it can decay via a $\Delta J=1$ transition to the ground state. For the ^{3}P$_1$ theoretical lifetimes are reported of approximately 100 [35], 150 [36] and 200 ns [37]. In a beam foil experiment [38], the decay was not observed indicating that the lifetime is much longer than 45 ns, consistent with the theoretical values.

During a period of one lifetime of 150 ns (average of the reported values), a 2 keV Sn particle travels a distance of approximately 0.8 cm. For a first

estimation of the role of $J=1$ metastables, we take three times the lifetime, a period after which 95% of the $J=1$ metastables has decayed to the ground state. The associated flight path of the 2 keV Sn particle is 2 cm. This path length should be compared to the mean free path (λ_F) of the particles which is equal to $(n\sigma_{21})^{-1}$. For the highest pressure used here of 6×10^{-4} mbar (1.5 $\times 10^{13}$ H_2 molecules per cm^3) and a σ_{21} of 10×10^{-16} cm^2 (discussed in the next paragraphs) one finds $\lambda_F \approx 67$ cm. Therefore only a very small fraction of the originally $J=1$ metastables will undergo a collision with a H_2 molecule before having decayed to the ground state. Thus, in the experiments presented here the $J=1$ metastables do not play an important role. Industrial sources operate at orders of magnitude higher H_2 pressures. For illustration, a pressure of say 1 mbar corresponds to a mean free path λ_F of ≈ 0.04 cm and therefore the opposite situation occurs where barely any of the $J=1$ metastables have decayed.

For each of the three J levels we performed a basic 2-state Landau-Zener model calculation [29] to obtain J-dependent cross sections for electron capture by metastable Sn^{2+*} ions. For the coupling matrix element the generic form of the expression derived for atomic hydrogen targets [27] was used. The correction for the different ionization potentials I_H and I_{H_2} of H and H_2, respectively, is done as in Refs. [27, 28] by scaling the coupling matrix element by $(I_{H_2}/I_H)^{1/2}$. The H_2 molecules are assumed all to be in the ground $\nu=0$ vibrational level, because for H_2 molecules the vibrational level spacing is much larger (about 0.5 eV between $\nu=0$ and $\nu=1$) than the thermal energy (0.03 eV) of H_2 gas at room temperature. However instead of the prefactor of 9.41 we used a prefactor of 5.48 as proposed by Kimura *et al.* [28] after optimization of Landau-Zener model calculations to their low-energy electron capture experiments on He. Other, early estimations more geared to lower charge state ions predicted even smaller prefactors [39, 40]. Therefore, we decided to use 5.48 as this value is in between those and it is experimentally benchmarked for another two-electron target. A different prefactor does not change the maximum cross section but shifts the position of the maximum cross section towards higher (larger prefactor) or lower (smaller prefactor) collision energy. The J-dependent cross section results are summarized in Figure 3.7.

To solve the set of differential equations, Eq. 3.3, the Sn^{2+*} population needs to be divided over its three J level populations. The J dependent populations are available from the theoretical studies in our earlier work ([21]). As that data was not explicitly shown in our earlier work, it is presented here in Figure 3.8. From the figure it is seen that the population is not statistical, only at the lowest collision energies the distribution tends towards a statistical
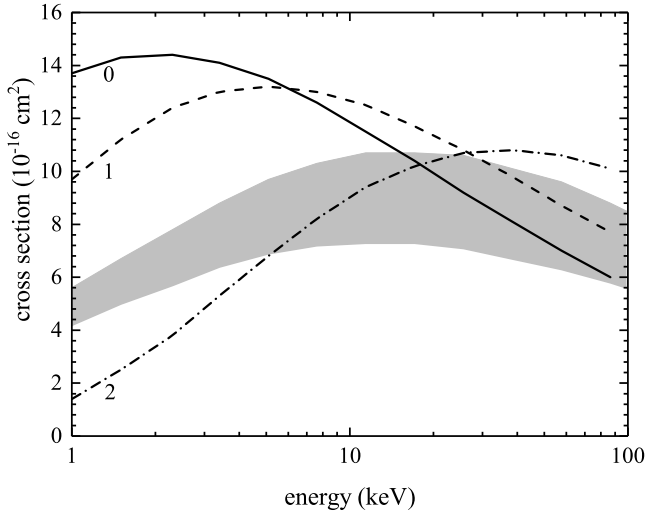
Figure 3.7: Cross sections for one-electron capture in 1 to 100 keV Sn^{2+}($5s5p\,^3$P$_J$) collisions with H$_2$ according to our Landau-Zener model calculations. The solid, dashed, and dashed-dotted lines correspond to the J levels, with J is 0, 1, and 2, respectively. The grey band represents $(2J+1)$ weighted average cross sections, with the upper limits of the band assuming the J=1 level fully contributing, and the lower limits of the band are defined by assuming no contribution by J=1.
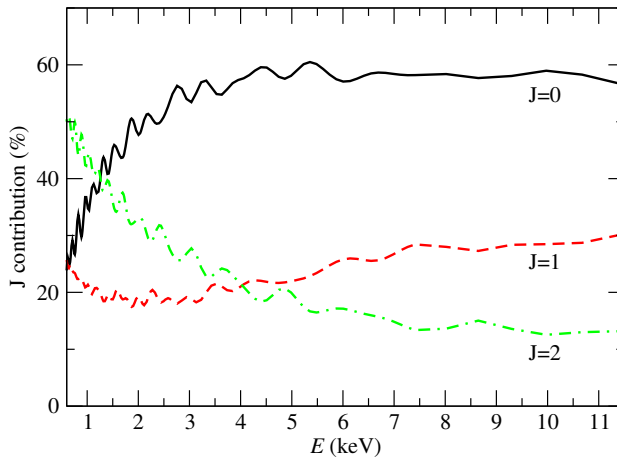
Figure 3.8: Calculated [21] J-dependent population fractions of the metastable Sn^{2+*}($5s5p\,^3$P$_J$) levels produced by one-electron capture in Sn^{3+} collisions on H$_2$.
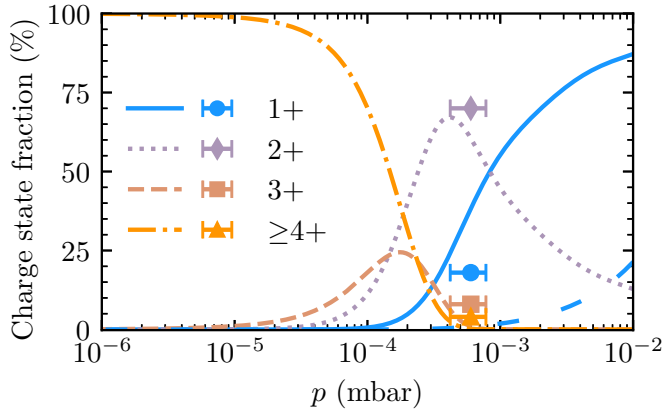
Figure 3.9: Simulated charge state distributions of energetic Sn^{q+} ions detected at a distance of 68.5 cm from the LPP plasma as a function of H_2 buffer pressures, assuming that all Sn^{2+} ions are produced in the metastable $5s5p$ ^3P term with a distribution over its J levels as shown in Figure 3.8. For $q \geq 4$ the actual q specific fractions as measured at $p=10^{-6}$ mbar (see Figure 3.3) were used as input in solving the set of differential equations. For ease of comparison, the dashed blue line shows the Sn^+ ion fraction if no metastables are included (taken from Figure 3.5). Solid points show the experimental LPP data.

one. For the simulations, an average energy of the Sn^{3+} ions of 2 keV is used, for which according to Figure 3.8 the population fractions of $J=0$, 1, and 2 are 45%, 20%, and 35%.

In addition, for the $J=1$ level it is assumed that it decays to the ground state before a next charge-changing collision occurs, thus with this $J=1$ level we associate the Sn^{2+} ground state capture cross section. For $J=0$ and 2 the calculated cross sections depicted in Figure 3.7 are used. Figure 3.9 shows the results of the simulations which now explicitly include metastable Sn^{2+*} ions. As can be seen from the figure, a rapid increase of the fraction of Sn^+ is predicted. Now with the inclusion of Sn^{2+*} metastables the charge state fractions at 6×10^{-4} mbar are in line with the experimental data. The simulations appear to indicate that the singly charged Sn ions get produced at pressures somewhat lower than seen in the experiment. However, this is likely a result of the fact that we have used upper limits for the electron capture cross sections for Sn ions in charge states of $q \geq 4$. Smaller cross sections will shift the curves in Figure 3.9 to the right to higher pressures for as Eq. 3.3 indicates it is the product of target density and cross section that factors into

the differential equations. For an optimal comparison between experiment and simulation, charge exchange cross sections for Sn^{q+} ions in charge states of $q \geq 4$ are called for. Nevertheless, the present simulations clearly highlight the key role of metastable Sn^{2+*} ions in the production of energetic keV Sn^+ ions by means of consecutive charge exchange starting from energetic highly charged Sn^{q+} ions with charge states of $q \geq 4$ ejected from the laser-produced plasma into the surrounding H_2 buffer gas.

3.4   Conclusion

We have investigated the evolution of charge-state-resolved kinetic energy spectra of Sn ions ejected from a LPP of Sn as a function of the density of the H_2 buffer gas surrounding the plasma. Without H_2 being present, energetic 1 to 5 keV Sn ions in charge states of 4+ to 8+ are detected. Sn ions in lower charge states are absent at energies above 1 keV. However, at the highest H_2 pressure of 6×10^{-4} mbar, no highly charged Sn ions are measured anymore at energies above 1 keV, only Sn^{2+} and Sn^+ ions are observed. The low-charged energetic Sn ions are produced by a series of consecutive electron capture processes. Therefore, in particular, the presence of Sn^+ ions is remarkable because electron capture by Sn^{2+} ions from H_2 is endothermic and thus very unlikely to happen at keV energies, which from an atomic collision perspective are very low-energies. To explain the production of keV Sn^+ ions, electron capture by metastable Sn^{2+*} ions is inferred. Previous work on $Sn^{3+} - H_2$ collisions [21] indicates that one-electron capture by Sn^{3+} ions populates primarily Sn^{2+} ions in metastable states. Using 2-state Landau Zener model cross sections for capture by the metastables, the key role of metastable Sn^{2+} is highlighted by model simulations using atomic collision cross sections to track the charge states of Sn ions while traversing the H_2 buffer gas.

The production of Sn^+ ions in the buffer gas is of relevance from an industrial EUV source perspective. It shifts the charge state balance away from Sn^{2+} towards Sn^+. As Sn^+ ions have a larger stopping cross section than Sn^{2+} ions [16], the production of Sn^+ ions is beneficial to stopping Sn ions escaping from an LPP plasma in a high charge state.

3.5   Acknowledgements

References

[1] G. O'Sullivan, B. Li, R. D'Arcy, P. Dunne, P. Hayden, D. Kilbane, T. McCormack, H. Ohashi, F. O'Reilly, P. Sheridan, E. Sokell, C. Suzuki, and T. Higashiguchi, "Spectroscopy of highly charged ions and its relevance to EUV and soft X-ray source development", *J. Phys. B: At. Mol. Opt. Phys.* **48**, 144025 (2015).

[2] O. O. Versolato, "Physics of laser-driven tin plasma sources of EUV radiation for nanolithography", *Plasma Sources Sci. Technol.* **28**, 083001 (2019).

[3] S. Bajt, J. B. Alameda, T. W. Barbee Jr., W. M. Clift, J. A. Folta, B. Kaufmann, and E. A. Spiller, "Improved reflectance and stability of Mo-Si multilayers", *Opt. Eng.* **41**, 1797 (2002).

[4] Q. Huang, V. Medvedev, R. van de Kruijs, A. Yakshin, E. Louis, and F. Bijkerk, "Spectral tailoring of nanoscale EUV and soft X-ray multilayer optics", *Appl. Phys. Rev.* **4**, 011104 (2017).

[5] F. Torretti, J. Sheil, R. Schupp, M. M. Basko, M. Bayraktar, R. A. Meijer, S. Witte, W. Ubachs, R. Hoekstra, O. O. Versolato, A. J. Neukirch, and J. Colgan, "Prominent radiative contributions from multiply-excited states in laser-produced tin plasma for nanolithography", *Nat. Commun.* **11**, 1–8 (2020).

[6] D. J. Hemminga, L. Poirier, M. M. Basko, R. Hoekstra, W. Ubachs, O. O. Versolato, and J. Sheil, "High-energy ions from Nd:YAG laser ablation of tin microdroplets: comparison between experiment and a single-fluid hydrodynamic model", *Plasma Sources Sci. Technol.* **30**, 105006 (2021).

[7] S. Fujioka, H. Nishimura, K. Nishihara, M. Murakami, Y.-G. Kang, Q. Gu, K. Nagai, T. Norimatsu, N. Miyanaga, Y. Izawa, K. Mima, Y. Shimada, A. Sunahara, and H. Furukawa, "Properties of ion debris emitted from laser-produced mass-limited tin plasmas for extreme ultraviolet light source applications", *Appl. Phys. Lett.* **87**, 241503 (2005).

[8] M. Murakami, Y. Kang, K. Nishihara, S. Fujioka, and H. Nishimura, "Ion energy spectrum of expanding laser-plasma with limited mass", *Phys. Plasmas* **12**, 062706 (2005).

[9]   A. Z. Giovannini, N. Gambino, B. Rollinger, and R. S. Abhari, "Angular ion species distribution in droplet-based laser-produced plasmas", *J. Appl. Phys.* 033302 (2015).

[10] M. J. Deuzeman, A. S. Stodolna, E. E. B. Leerssen, A. Antoncecchi, N. Spook, T. Kleijntjens, J. Versluis, S. Witte, K. S. E. Eikema, W. Ubachs, R. Hoekstra, and O. O. Versolato, "Ion distribution and ablation depth measurements of a fs-ps laser-irradiated solid tin target", *J. Appl. Phys.* **121**, 103301 (2017).

[11] A. Bayerle, M. J. Deuzeman, S. van der Heijden, D. Kurilovich, T. de Faria Pinto, A. Stodolna, S. Witte, K. S. E. Eikema, W. Ubachs, R. Hoekstra, and O. O. Versolato, "Sn ion energy distributions of ns-and ps-laser produced plasmas", *Plasma Sources Sci. Technol.* **27**, 045001 (2018).

[12] V. Bakshi (ed), *EUV lithography*, 2nd edn, Bellingham, WA: SPIE Press, 2018.

[13] T. E. Sharp, "Potential-energy curves for molecular hydrogen and its ions", *At. Data Nucl. Data Tables* **2**, 119–169 (1971).

[14] M. Wacks, "Franck-Condon factors for ionization of H_2, HD and D_2", *J. Res. Natl. Bur. Stand., Sect. A* **68**, 631 (1964).

[15] A. Kramida, Y. Ralchenko, J. Reader, and NIST ASD Team, NIST Atomic Spectra Database (ver. 5.3), [Online]. Available: `http://physics.nist.gov/asd` [2022, October 21]. National Institute of Standards and Technology, Gaithersburg, MD. 2015.

[16] D. Abramenko, M. Spiridonov, P. Krainov, V. Krivtsun, D. Astakhov, V. Medvedev, M. van Kampen, D. Smeets, and K. Koshelev, "Measurements of hydrogen gas stopping efficiency for tin ions from laser-produced plasma", *Appl. Phys. Lett.* **112**, 164102 (2018).

[17] D. Kurilovich, A. L. Klein, F. Torretti, A. Lassise, R. Hoekstra, W. Ubachs, H. Gelderblom, and O. O. Versolato, "Plasma propulsion of a metallic microdroplet and its deformation upon laser impact", *Phys. Rev. Appl.* **6**, 014018 (2016).

[18] L. Poirier, A. Bayerle, A. Lassise, F. Torretti, R. Schupp, L. Behnke, Y. Mostafa, W. Ubachs, O. O. Versolato, and R. Hoekstra, "Cross-calibration of a combined electrostatic and time-of-flight analyzer for energy-and charge-state-resolved spectrometry of tin laser-produced plasma", *Appl. Phys. B* **128** (2022).

[19] L. Poirier, A. Lassise, Y. Mostafa, L. Behnke, N. Braaksma, L. Assink, R. Hoekstra, and O. O. Versolato, "Energy-and charge-state-resolved spectrometry of tin laser-produced plasma using a retarding field energy analyzer", *Appl. Phys. B* **128**, 135 (2022).

[20] R. Kersevan and M. Ady, "Recent developments of Monte-Carlo codes MolFlow+ and SynRad+", in Proc. 10th Int. Particle Accelerator Conf. (IPAC'19), Melbourne, Australia (2019).

[21] S. Rai, K. I. Bijlsma, I. Rabadán, L. Méndez, P. A. J. Wolff, M. Salverda, O. O. Versolato, and R. Hoekstra, "Charge exchange in collisions of 1–100-keV Sn^{3+} ions with H_2 and D_2", *Phys. Rev. A* **106**, 012804 (2022), Note: this publication forms Chapter 2 of this thesis.

[22] R. Mann, F. Folkmann, and H. F. Beyer, "Selective electron capture into highly stripped Ne and N target atoms after heavy-ion impact", *J. Phys. B: At. Mol. Phys.* **14**, 1161 (1981).

[23] H. Ryufuku, K. Sasaki, and T. Watanabe, "Oscillatory behavior of charge transfer cross sections as a function of the charge of projectiles in low-energy collisions", *Phys. Rev. A* **21**, 745 (1980).

[24] A. Niehaus, "A classical model for multiple-electron capture in slow collisions of highly charged ions with atoms", *J. Phys. B: At. Mol. Phys.* **19**, 2925–2937 (1986).

[25] M. Imai, Y. Iriki, and A. Itoh, "Target Dependence of Single-Electron-Capture Cross Sections for Slow Be, B, C, Fe, Ni, and W Ions Colliding with Atomic and Molecular Targets", *Fusion Sci. Tech.* **63**, 392 (2013).

[26] R. Lomsadze, M. Gochitashvili, and R. Kezerashvili, "Inelastic processes in Na^+-Ne, Na^+-Ar, Ne^+-Na, and Ar^+-Na collisions in the energy range 0.5-14 keV", *Phys. Rev. A* **92**, 062703 (2015).

[27] R. E. Olson and A. Salop, "Electron transfer between multi charged ions and neutral species", *Phys. Rev. A* **14**, 579 (1976).

[28] M. Kimura, T. Iwai, Y. Kaneko, N. Kobayashi, A. Matsumoto, S. Ohtani, K. Okuno, S. Takagi, H. Tawara, and S. Tsurubuchi, "Landau-Zener Model Calculations of One-Electron Capture from He Atoms by Highly Stripped Ions at Low Energies", *J. Phys. Soc. Jpn.* **53**, 2224–2232 (1984).

[29] R. K. Janev and H. Winter, "State-selective electron capture in atom-highly charged ion collisions", *Phys. Rep.* **117**, 265–387 (1985).

[30] W. Fritsch and C. D. Lin, "The semiclassical close-coupling description of atomic collisions: Recent developments and results", *Phys. Rep.* **202**, 1–97 (1991).

[31] P. C. Stancil, A. R. Turner, D. L. Cooper, D. R. Schultz, M. J. Rakovic, W. Fritsch, and B. Zygelman, "Electron capture in collisions of S4+ with atomic hydrogen", *J. Phys. B: At. Mol. Opt. Phys.* **34**, 2481 (2001).

[32] R. Hoekstra, H. Anderson, F. W. Bliek, M. von Hellermann, C. F. Maggi, R. E. Olson, and H. P. Summers, "Charge exchange from D(n = 2) atoms to low-Z receiver ions", *Plasma Phys. Controlled Fusion* **40**, 1541 (1998).

[33] I. I. Sobelman, *Atomic spectra and radiative transitions* (Springer-Verlag, Berlin Heidelberg New York, 1979).

[34] M. F. Gu, "The flexible atomic code", *Can. J. Phys.* **68**, 675 (2008).

[35] K. Haris and A. Tauheed, "Revised and extended analysis of doubly ionized tin: Sn III", *Phys. Scr.* **85**, 055301 (2012).

[36] L. J. Curtis, R. Matulioniene, G. Ellis, and C. Froese Fischer, "Predictive data-based exposition of $5s5p$ ^{1,3}P$_1$ lifetimes in the Cd isoelectronic sequence", *Phys. Rev. A* **62**, 052513 (2000).

[37] C. Colón and A. Alonso-Medina, "Calculation of oscillator strengths, transition probabilities and radiative lifetimes of levels in Sn III", *J. Phys. B: At. Mol. Opt. Phys.* **43**, 165001 (2010).

[38] J. A. Kernahan, E. H. Pinnington, W. Ansbacher, and J. L. Bahr, "Experimental mean lives for levels in Sn III and Sn IV", *Nucl. Instrum. Methods Phys. Res., Sect. B* **9**, 616 (1985).

[39] R. E. Olson, F. T. Smith, and E. Bauer, "Estimation of the Coupling Matrix Elements for One-Electron Transfer Systems", *Appl. Opt.* **10**, 1848–1855 (1971).

[40] S. E. Butler and A. Dalgarno, "Charge transfer of multiply charged ions with hydrogen and helium Landau-Zener calculations", *Astrophys. J.* **241**, 838–843 (1980).

CHAPTER 4

Single and double electron capture in low-energy collisions of Sn^{3+} ions with molecular hydrogen

Abstract

We report experimental single and double electron capture cross sections for Sn^{3+} ions impacting on H$_2$ molecules at low projectile energies, ranging from 0.4 eV/u to 153 eV/u. The data is obtained by means of a crossed-beam type experiment with a decelerated Sn^{3+} ion beam and an H$_2$ gas jet. Charge-state resolved Sn ion numbers are measured with a retarding field analyzer. After an extensive description of the setup and measurement procedure we present and discuss the results. The single capture cross section is found to have values in the range 20–40 × 10^{-16} cm^2 with a shallow maximum around 20 eV/u. We compare the results to semiclassical calculations down to 10 eV/u and find good agreement. The double capture cross section shows a remarkable sharp increase by an order of magnitude upon decreasing the energy from 100 to 10 eV/u. We propose a mechanism that could explain the unexpectedly large cross sections for this process at low energies. We also performed the experiments for a D$_2$ target and find marginal differences compared to a H$_2$ target.

This chapter forms the experimental basis of a future joint experimental and theoretical publication in collaboration with professors Rabadán and Méndez.

4.1　Introduction

Electron capture, also known as charge transfer or charge exchange, is the process in which a projectile ion colliding with a neutral atomic or molecular target takes one or more target electrons. The process is relevant in several research areas, from fusion (e.g. [1–5]) to astrophysics (e.g. [6, 7]) and lately also in nanolithography research [8, 9]. The particular collision system of Sn ions on H_2 molecules is highly relevant for the latest generation of nanolithography machines, which use 13.5-nm extreme ultraviolet (EUV) light for printing fine features on silicon wafers [10, 11]. This light is emitted by highly charged Sn ions in a Sn laser-produced plasma (LPP) [12, 13] and subsequently collected and focused to the reticle and wafer by Mo/Si-multilayer mirrors. Fast Sn ions (keV energy) coming from the LPP [14–16] have the potential to cause damage to the collector mirror by sputtering and implantation and therefore need to be slowed down [17]. A buffer gas of H_2 has been chosen for this purpose because of its low absorptivity of EUV light and its ability to etch Sn particles from a surface [18]. Stopping cross sections in this collision system are needed for optimization models, however fundamental data is scarce. To our knowledge, only one paper is available that reports stopping cross sections for Sn ions on H_2 [19]. The results there show that the stopping cross section depends on the charge state of the Sn ion. Even though Sn ions with charge states of 9+ – 15+ are responsible for EUV emission [12, 13, 20], energetic (> 1 keV) ions coming from the LPP have charge states of 3+ – 8+ [9, 16]. Electron capture in collisions of these ions with hydrogen molecules will bring the charge state further down. Therefore not only stopping, but also electron capture cross sections are needed for accurate EUV-source models. According to the classical over-barrier model, the single capture cross section scales with the projectile's initial charge state q [21]. Electron capture cross sections for the higher charge states are therefore expected to be large, such that the lower charge states are dominantly present in the stopping gas. We are therefore mainly interested in the lower charge states.

Recently, we published a joint experimental and theoretical paper on single electron capture in collisions of Sn^{3+} ions with H_2 and D_2 molecules [22] (Chapter 2). We presented experimental cross sections in the energy range of 76 – 430 eV/u (9 – 51 keV) and cross sections from semiclassical calculations in the energy range 10 – 1000 eV/u (1 – 120 keV). Experimentally, we observed a strong energy dependence of the cross section, with the cross section growing larger when moving to lower energies. Also, the difference in cross section between H_2 and D_2 (higher values for H_2) increased at lower

energies. At 76 eV/u however, we reached a lower limit to the energy that could be experimentally obtained because of inefficient ion beam extraction and transportation at low energies. The observed behaviour raises the question whether the trends of an increasing cross section and growing isotope effect continue to even lower energies. This energy regime of total energies from 10 keV down to several tens of eV is especially relevant for industrial EUV sources as most of the Sn ions that are emitted from the LPP have an energy in that range [14].

Electron capture by multiply charged ions of sub-keV energy colliding with neutral species is hard to study experimentally as highly charged ion sources (e.g. [23]) are operated at several kV to produce the required intense beams of multiply charged ions. A way to achieve low relative velocities could be the technique of merged beams [24]. This technique has been successfully applied to systems in which neutral beams can be produced by electron detachment of negative ions, e.g. neutral atomic hydrogen produced by laser irradiation of H^- [25, 26]. However, many atoms and molecules do not have suitable negative ions and thus are not available to merged beam experiments. Neutral molecular hydrogen is for example not available to merged-beams experiments. For H_2 as target, to get to energies well below 1 keV/u, attempts in crossed-beam type of experiments were therefore made by means of putting the collision region on high voltage [27] or having the collision center inside an RF ion guide floating at high voltage [28]. However, to overcome issues with field penetration into the collision region and changing potentials in the collision chamber along the ion beam, which would hamper total charge-transfer measurements, in the present experimental study we have put our whole crossed beam apparatus on high voltage and used an electrostatic lens system for efficient deceleration and focusing of the decelerated beam of multi-charged ions.

The new apparatus is used to measure absolute cross sections for single and bound double electron capture (SC and BDC, respectively) from H_2 (and D_2) by Sn^{3+} ions, i.e. for the reactions

$$Sn^{3+} + H_2 \rightarrow Sn^{2+} + H_2^+, \tag{4.1}$$

$$Sn^{3+} + H_2 \rightarrow Sn^+ + 2H^+. \tag{4.2}$$
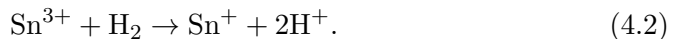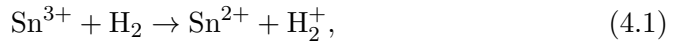
In the experiments, Sn^{3+} ions in the low energy range of 0.4 – 153 eV/u (50 eV – 18 keV) are used as projectiles, corresponding to velocities of $(4 - 78) \times 10^{-3}$ a.u.
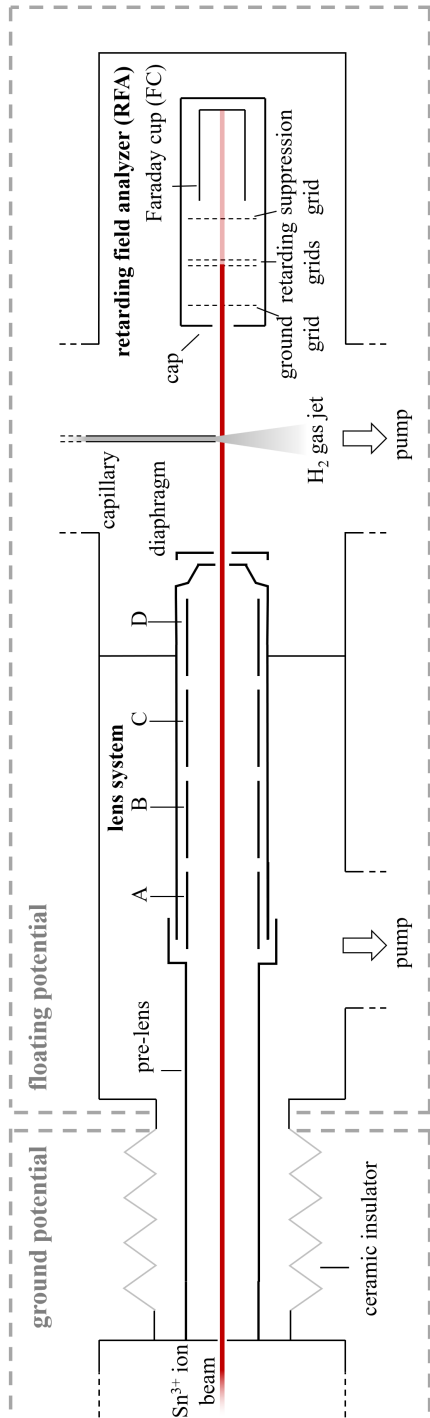
Figure 4.1: Schematic of the crossed beam setup. Dashed partial rectangles indicate the separation between the setup on a floating potential and the beamline on ground potential. Energy-, charge- and mass-selected ions come in from the left, are decelerated by the lens system, traverse the gas target created by a gas flow from the capillary, and are finally analyzed by the retarding field analyzer (RFA). The six-element lens system consists of a pre-lens on ground potential, four equal-length cylindrical elements A–D to which variable voltages can be applied, and a final tapered element with a ϕ 1.5 mm diaphragm on setup potential. The RFA has four grids: a ground grid preventing field penetration into the collision region, two retarding grids to which a high voltage can be applied, thereby creating a homogeneous potential barrier to block ions based on their energy-to-charge ratio and finally a negatively biased suppression grid preventing secondary electrons to escape the Faraday cup (FC). Ions hitting this FC get neutralized. This creates a current, proportional to the number of ions and their charge state, which is measured with a picoammeter. The background pressure in the chamber is $\approx 1 \times 10^{-8}$ mbar.

4.2 Experimental methods

4.2.1 Experimental setup

For our charge transfer experiments we employ a crossed-beam setup in which a beam of mono-energetic Sn^{3+} ions crosses a gas jet of molecular hydrogen. We have severely modified our setup compared to our previous work [22]. The main differences are the use of decelerated Sn^{3+} beams to cover the low-energy regime below 9 keV and the use of a retarding field analyzer (RFA) to determine the charge state distribution of the Sn ions after crossing the molecular hydrogen target. Before discussing these two experimental upgrades the ion beam facility will be recalled briefly.

The experiments use ion beams generated with the ZERNIKELEIF low-energy ion beam facility at the University of Groningen. Sn^{q+} ions are generated in a 14 GHz electron cyclotron resonance ion source (ECRIS), operated on a high potential V_{source}. Sn atoms are introduced into the ECRIS plasma by heating a crucible oven filled with solid pure tin. After extraction from the ECRIS, the primary ion beams are mass-over-charge (m/q) selected using a 110° analyzing magnet with a resolution of about 0.5%, allowing for selecting Sn ion beams of one specific isotope only. Although ^{120}Sn is the most abundant isotope of Sn, ions of the second most abundant isotope are used in the experiments, i.e. ^{118}Sn, because ^{120}Sn^{3+} has the same m/q ratio as Ar$^+$ and thus a possible (small) Ar$^+$ contamination cannot *a priori* be excluded for ^{120}Sn^{3+}. The m/q-analysed ^{118}Sn^{3+} ion beam is transported through a 10-m central beamline and steered into the crossed-beam setup by a 45° bending magnet. On the way from the bending magnet to the gas jet, the ion beam is collimated by a set of six apertures, the smallest one with a diameter of 1.5 mm.

Primary Sn^{q+} ion beams can be extracted efficiently from the ECRIS with energies in the range of $3q$ to $25q$ keV. The low-energy ion beams used in the experiments are generated by decelerating primary Sn^{3+} ion beams of typically 21 keV just before they enter the crossed-beam setup. To do so, the entire setup is floated on a high potential. A six-element deceleration lens is used to prevent ion losses due to beam broadening upon deceleration. More details about the deceleration process are given in Section 4.2.2.

The crossed-beam setup is schematically depicted in Figure 4.1. At the center of the collision chamber, the ion beam traverses a jet of H$_2$ gas that is flowing from a capillary of 1.0 mm internal diameter that is situated 1.0 mm above the ion beam. A Bronkhorst FG-200CV high precision mass flow controller is used to regulate the gas flow. Flowrates of 1, 2.5, and 4 ml/min are

used in the experiments, which correspond to chamber pressures of (0.46, 1.14, and 1.81) $\times 10^{-4}$ mbar, respectively. The pressure in the chamber is measured by a Pfeiffer HPT 100 gauge. The background pressure in the chamber is $\approx 1 \times 10^{-8}$ mbar. During experiments, the base pressure is higher due to the presence of H_2: $\approx 2 \times 10^{-7}$ mbar.

After traversing the gas jet, the Sn ions are analyzed and collected by a retarding field analyzer (RFA), which consists of a Faraday cup (FC) with grids in front onto which potentials are applied to generate a well-defined retarding potential V_{ret}. Ions can only pass through the central grids if the ratio E/q of their kinetic energy to their charge state is larger than V_{ret}. The ions that pass, finally land in the FC. There, neutralization of the ions causes a current, proportional to the number of ions and their charge state, which is read by a Keithley 6485 picoammeter. Our RFA is a modified four-grid Kimball FC73-A type of RFA. Wirings are altered such that it can be operated at higher voltages, up to 10 kV. The entrance of the RFA is covered with a so-called 'cap', which has a 2.6-mm diaphragm. The retarding voltage is applied to the two center grids, whereas the first grid is grounded and a suppressing voltage V_S of -100 V is applied to the final grid to prevent secondary electrons from escaping the FC. By choosing appropriate retarding voltages, we can obtain charge-state resolution in the measured current which enables us to obtain N^+, N^{2+}, and N^{3+}, the number of Sn^+, Sn^{2+}, and Sn^{3+} particles, respectively.

4.2.2   Ion beam deceleration

As explained in the previous section, the primary ion beam needs to be decelerated in order to perform experiments at low energies. For that, the experimental chamber, including all auxiliary equipment and electronics, is floated on a high potential. To eliminate the detrimental effect of ripples in high-voltage power supplies, this is accomplished by connecting the setup with the ECRIS and using an offset voltage V_{bias}, such that the setup potential equals $V_{source} - V_{bias}$. Consequently, the ion energy is reduced from qV_{source} to qV_{bias} ($q = 3$ here). Additionally, a small intrinsic plasma potential V_{plasma} on the order of 10 V is generated in the ECRIS [29], which contributes qV_{plasma} to the final energy. For low collision energies, this contribution becomes considerable, and is therefore corrected for by reducing the set V_{bias} appropriately.

Except for the case of very mild deceleration to total energies larger than 12 keV, the sudden step in potential causes strong beam divergence which leads to large ion beam losses. To overcome this problem, an electrostatic deceleration and focusing lens system is used. The same lens system has been

used previously by Bodewits *et al.* [30] and has a design based on similar designs which have been used successfully in the past [31, 32]. The six-element lens system consists of a pre-lens on ground potential, four equal-length cylindrical elements A–D, and a final tapered element with a ϕ 1.5 mm diaphragm on setup potential (see Figure 4.1).

The potentials on lens elements A–D were determined by an optimization process. The values were iteratively changed while reading the FC current, I_{FC}, as well as the current on the cap (including a current contribution from the ground grid), I_{cap}, with the goal of maximizing I_{FC} while having the ratio I_{FC}/I_{cap} as large as possible, at least larger than unity. For ion energies ≥ 150 eV it was found optimal to use a potential scheme such that the ions undergo a brief acceleration in between two deceleration steps. For the lowest energies a gradual deceleration scheme was found to be optimal.

4.2.3 Measurement procedure

Extracting single and double electron capture cross sections

In electron capture of Sn^{3+} from H_2, either one or both of the electrons of H_2 can be captured, reaction 4.1 (SC) and 4.2 (BDC), respectively. We first assume to operate in the single-collision regime. A correction for double collisions is applied later, see Section 4.2.4. The differential equation describing N^{3+} as a function of distance through the collision chamber z is given by the following equation:

$$\frac{dN^{3+}}{dz} = -(\sigma_{32} + \sigma_{31})n(z)N^{3+}, \qquad (4.3)$$

where $n(z)$ is the target density and σ_{32} and σ_{31} are the SC and BDC cross sections, respectively. Let us now define the double capture fraction f:

$$f \equiv \frac{\sigma_{31}}{\sigma_{32}}. \qquad (4.4)$$

Using this double capture fraction, Eq. 4.3 can be solved for σ_{32}, yielding:

$$\sigma_{32} = -\frac{\ln(\frac{N^{3+}}{N_0^{3+}})}{(1+f)\int_0^L n(z)dz}, \qquad (4.5)$$

where L is the length over which the ion beam overlaps with the gas target and N_0^{3+} is the initial number of Sn^{3+} ions. Note that the RFA enables us to obtain N^+, N^{2+}, and N^{3+} (see next subsection). Conservation of particles

dictates that $N_0^{3+} = N^+ + N^{2+} + N^{3+}$. In the single-collision regime, we can write:

$$f = \frac{N^+}{N^{2+}}. \tag{4.6}$$

Note that this is an easier and more direct method to asses the bound double capture fraction as compared to our previous study [22], where we had to use time-of-flight spectroscopy on the target fragments to determine this quantity. The integral target density $\int_0^L n(z)dz$ is proportional to the pressure P in the collision chamber. The proportionality factor β is calibrated using O^{6+} ions, see Section 4.2.5. Equation 4.5 now becomes:

$$\sigma_{32} = -\frac{\ln(\frac{N^{3+}}{N^+ + N^{2+} + N^{3+}})}{(1 + \frac{N^+}{N^{2+}})\beta P}. \tag{4.7}$$

To conclude, from the experimental data we calculate f and σ_{32} following Eq. 4.6 and Eq. 4.7, respectively, and from their multiplication we get σ_{31} (see Eq. 4.4).

Obtaining charge-state resolved Sn ion numbers

Contrary to our previous work [22], the gas flows continuously from the capillary during a measurement. As can be seen from reactions 4.1 and 4.2, the ion beam that arrives at the RFA consists of Sn^{3+}, Sn^{2+}, and Sn^+ particles. The spread in ion energy due to the plasma potential of the ECR source is on the order of 10 eV [29]. The energy transfer in one charge-exchange collision is of roughly the same magnitude. Both variations in energy are small compared to our projectile energies, such that we can safely assume all ions arriving in the RFA to have approximately equal energy. For our lowest probed energy of 50 eV, this might however not be the case and it could lead to an error in separating charge states. Since the RFA selects on E/q, we can obtain charge-state resolution in the measured current by choosing appropriate retarding voltages. To illustrate this, Figure 4.2 shows the Faraday cup current as a function of retarding voltage for a 4 keV Sn^{3+} ion beam traversing the H_2 target at intermediate flow ($P_{chamber} = 1.14 \times 10^{-4}$ mbar). The red arrows indicate the voltages at which 3+, 2+, and 1+ particles of 4 keV energy are expected to be stopped by the RFA. Indeed, we see clear drops in the current at those voltages. Interestingly, after the 4 keV Sn^+ ions are blocked, a positive current remains visible until it drops to zero at around 4800 V. This is an artifact of the deceleration process. The ion beam is decelerated from a primary ion beam of 21 keV. Some hydrogen molecules diffuse out of the collision chamber
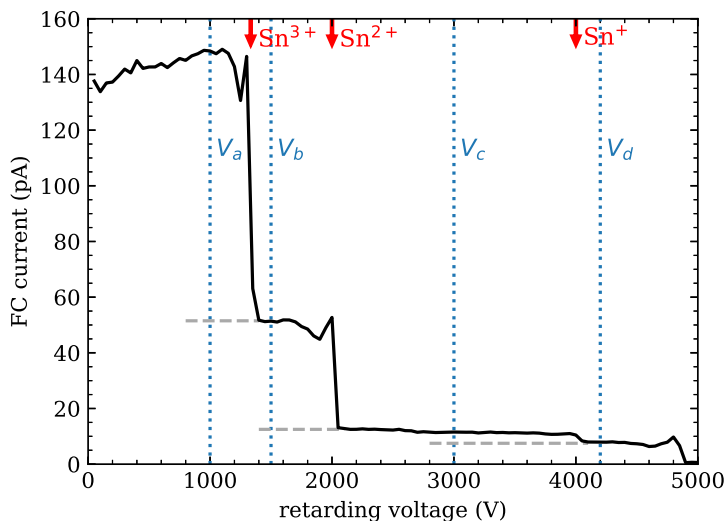
Figure 4.2: The Faraday cup current as a function of retarding voltage for a 4 keV Sn^{3+} ion beam traversing the H_2 target at intermediate flow ($P_{chamber} = 1.14 \times 10^{-4}$ mbar). The ion beam is decelerated from a primary ion beam of 21 keV. Red arrows indicate the voltages at which 3+, 2+, and 1+ particles of 4 keV energy are expected to be stopped by the RFA. Vertical dotted blue lines indicate typical voltages that were used for determination of electron capture cross sections. Light-gray dashed lines are drawn at the approximate value of the current after a charge state is stopped, to indicate the "zero" levels for each of the three individual charge states.

into the deceleration lens and accumulate in the pre-lens. This latter part is still on ground potential. If a 21 keV Sn^{3+} ion undergoes single capture there, it results in a 21 keV Sn^{2+} ion. When this ions climbs 5.67 kV in potential in the deceleration process ($\frac{(21-4)\text{ keV}}{3e}$, as determined for a Sn^{3+} ion), it loses 11.33 keV of energy in this step and therefore has an energy of 9.67 keV in the collision chamber. A retarding voltage of 4.83 kV is needed to stop this particular ion. So Sn^{2+} (and possibly some Sn^{+}) ions of a higher energy constitute the "artifact" current that is seen to remain as the 4 keV Sn^{+} ions are stopped. We correct our measurements for this artifact.

In an actual measurement, we do not scan the retarding voltage as shown in Figure 4.2 but instead we take current measurements at four carefully chosen voltages. The first voltage V_a is chosen to be below the voltage where the

Sn^{3+} ions are expected to be blocked, see Figure 4.2. The second voltage V_b is chosen beyond the voltage where the Sn^{3+} ions are blocked, but before the voltage where Sn^{2+} ions are blocked and similarly the third voltage V_c is in between the voltages where the Sn^{2+} and Sn^+ ions are blocked. Finally, a measurement is performed at V_d, above the voltage where Sn^+ ions are blocked but before the next drop, as to determine the artifact current. The three aforementioned currents are corrected for this artifact current by subtracting it from the currents measured at V_a, V_b, and V_c. A measured current I can be written as

$$I = e \sum_{q=1}^{3} (qN^{q+})/\Delta t, \tag{4.8}$$

where e is the elementary charge, q the charge state of the Sn ion, N^{q+} the number of Sn ions with that charge state, and Δt the time interval over which the ions are measured. By taking differences of measured currents we can obtain N^+, N^{2+}, and N^{3+}.

Returning to Figure 4.2, it can be seen that as the retarding voltage increases from 0 to roughly 1 kV, the FC current shows a gradual increase of about 10%. Then, as it nears the point where the Sn^{3+} ions are stopped, it shows an oscillation. This behaviour can be attributed to an electrostatic lens effect in the RFA which is most prominent when the ions are slowed down to low velocity [33]. We correct our measurements for this voltage-dependent RFA transmission in the following way. Next to performing the measurement described above, we do record a scan of the retarding voltage for the case when the H_2 gas flow is turned off such that the ion beam consists purely of Sn^{3+} ions. A five-point rolling average is applied to remove measurement noise. The resulting curve is used to determine transmission coefficients for the three charge states at the voltages V_a, V_b, and V_c. These coefficients are used to make corrections when transforming the currents into ion numbers. The effect of this correction is small. In the measurements, care is also taken that the voltages V_a, V_b, V_c, and V_d are outside of the region where the curve shows oscillatory behaviour.

4.2.4   Correction for double collisions

The expressions for f and σ_{32} (Eq. 4.6 and Eq. 4.7, respectively) hold in the single-collision regime. Therefore, low gas flows are used such that the majority of the Sn ions after traversing the gas are still in the 3+ charge state. However, at these gas flows it could still be the case that a small fraction of the ions
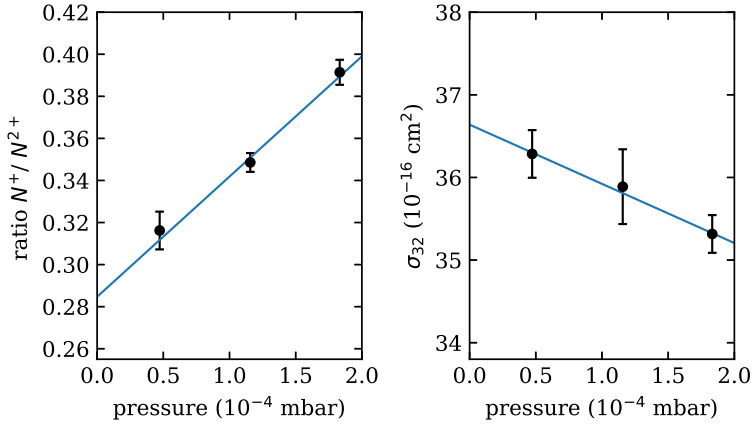
Figure 4.3: Ratio N^+/N^{2+} (left panel) and single capture cross section (right panel) measured at three H_2 pressures for an incoming Sn^{3+} ion of 0.7 keV. Both panels show a linear fit through the data, taking data uncertainties into account. To eliminate the effect of double collisions, the value obtained by extrapolating the fit to zero pressure is taken as final value.

undergo two (or more) consecutive charge transfer collisions. To correct for this effect, the measurements are performed at three different flows of H_2 gas and the results are extrapolated to zero pressure.

Figure 4.3 shows the situation and illustrates the procedure for a Sn^{3+} ion beam of 0.7 keV. The left panel shows the ratio N^+/N^{2+} at three different pressures corresponding to the three gas flows that are used in the experiment. It clearly shows that the ratio increases at higher pressures. This can be explained by more second collisions happening at the higher densities, which turn a Sn^{2+} ion into a Sn^+ ion. It also shows that the effect is linear with pressure, which shows that we are not in the pressure regime of tertiary (or even more) collisions. The observed increase in the N^+/N^{2+} ratio is with roughly 30% over our pressure range substantial and hints at a considerable single electron capture cross section for Sn^{2+} ions, which is in line with findings by Rai *et al.* [9] (Chapter 3), which could only be explained by inferring large single capture cross sections for Sn^{2+} ions. The value of the ratio obtained by extrapolating the fit to zero pressure is taken as the true double capture fraction f and is used to calculate σ_{31}. The ratio N^+/N^{2+} also appears in the equation for σ_{32} (see Eq. 4.7), and therefore double collisions are also expected to influence this measured cross section. The right panel of Figure 4.3 shows

that the measured cross section indeed decreases linearly with pressure, but the effect is small (less than 3%). Nevertheless, here we also take the value obtained from extrapolating the fit to zero pressure as final value.

4.2.5 Calibration of the integral target density

The general expression for the single capture cross section (Eq. 4.5) contains the integral target density $\int_0^L n(z)dz$. The exact profile of the gas jet, and even more its overlap with the ion beam, is hard to determine accurately. Therefore a different approach is used. The charge transfer experiment is performed with a projectile of known electron capture cross section on H_2 such that the unknown integral target density can be determined. In fact, the proportionality factor β between the integral target density and the measured pressure P is determined, such that the integral target density can be obtained at any value of the gas flow.

In our previous study we used proton projectiles for such a calibration. However, they are not suited for the measurement procedure employed here, which relies on measuring N^{q+}, $N^{(q-1)+}$, and $N^{(q-2)+}$ for a projectile of charge state q. We therefore need a projectile with $q \geq 3$ and for which double electron capture cross sections are available. We have chosen the system O^{6+} on H_2 and used the experimental cross section at 21 keV reported by Machacek *et al.* [34].

The full experimental procedure, including correction for double collisions, has been performed with O^{6+} projectiles. For the H_2 target, an undecelerated O^{6+} beam was used, giving a β of $(75 \pm 3) \times 10^{16}$ cm^{-2} mbar^{-1}. For undecelerated beams, the integral target density is expected to be larger compared to when decelerated beams are used, because the gas that is present in the pre-lens also contributes to the density, whereas this part is excluded for decelerated beams (see Section 4.2.3). By using Sn^{3+} projectiles (and a fixed β), it was found that the cross sections measured with direct beams are $(16\pm5)\%$ larger than with decelerated beams. In the actual measurements we always use decelerated beams. This means that the aforementioned β obtained with undecelerated O^{6+} should be scaled by the factor $1/1.16$. In this way, a value for β of $(65 \pm 4) \times 10^{16}$ cm^{-2} mbar^{-1} for H_2 has been determined.

For the case of D_2 as target gas, β has been determined with a decelerated O^{6+} beam, resulting in a value of $(83 \pm 2) \times 10^{16}$ cm^{-2} mbar^{-1}.

4.2.6 Uncertainties

A typical measurement for a certain ion energy and gas flow goes as follows. In one so-called cycle, ten current samples are recorded at each of the four voltages V_a, V_b, V_c, and V_d. From this data, four average currents are obtained which are subsequently converted to particle numbers as described in Section 4.2.3. These are used to calculate the double capture fraction and the single capture cross section according to Eq. 4.6 and Eq. 4.7, respectively. In total, four cycles are performed. If a plasma instability in the ECRIS causes a spike or dip in the current, that cycle is removed. An average and standard deviation for the two quantities of interest are then calculated over these cycles. For one energy, the above procedure is performed for three values of the gas flow. As described in Section 4.2.4, the final value is obtained from the y-intercept of a linear fit made through the three data points, taking standard deviations into account. A (partial) statistical uncertainty Δ_f is quantified by the standard deviation on the fitted y-intercept.

Other effects, e.g. the effect of temperature fluctuations, of mass flow controller and pressure gauge stabilities and of beam focusing effects due to deceleration, are more difficult to quantify. Therefore, we repeated measurements at different days under different circumstances and looked at the reproducibility of obtained cross sections. For the single capture cross section a reproducibility Δ_r of 5% was found, whereas for the case of double capture a value of 10% was found.

The total statistical uncertainty Δ_S is obtained by taking the quadratic sum of Δ_f and Δ_r. This total statistical uncertainty defines the error bars presented in the figures shown in the results section. Note that the uncertainty due to the calibration by the reference O^{6+} data is not included in the error bars, because it is a systematic uncertainty which could lead to a shift of all points, either up or down. This uncertainty has two contributions. First, the total uncertainty reported for the reference data is 3.4% [34]. Second, our experimental determination of β has an uncertainty of 6%. Combined, this leads to a systematic uncertainty of 7%.
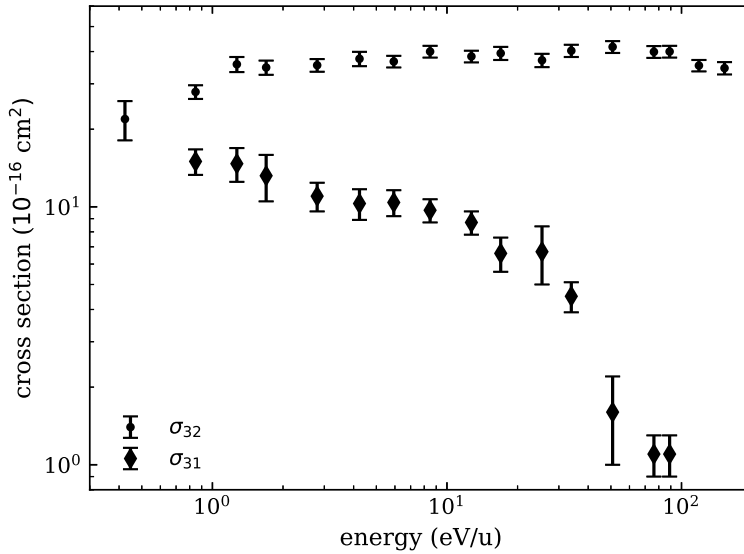
Figure 4.4: Measured single (σ_{32}) and double (σ_{31}) electron capture cross sections for Sn^{3+} ions colliding with H_2 molecules, as a function of ion energy in eV/u.

4.3   Results and Discussion

Figure 4.4 shows the experimentally obtained single and double electron capture cross sections as a function of ion energy. The single capture cross section is dominant, and relatively energy independent over the energy range of 1 to 100 eV/u with a value around 4×10^{-15} cm^2. For higher and especially for lower energies, the cross section decreases. The double capture cross section exhibits a striking energy dependence. At energies just below 100 eV/u, this cross section is small with a value around 1×10^{-16} cm^2. Upon decreasing the energy, the cross section has a sharp increase around 40 eV/u and continues to increase steadily all the way down to 1 eV/u, where it attains a value of 15×10^{-16} cm^2.

At the lowest energy (0.4 eV/u), the signal-to-noise ratio was worse than it was at the other measurements, due to an unstable and low-intensity ion beam caused by the strong deceleration. This causes the relatively large uncertainty in σ_{32} at that energy. From Figure 4.2 it can be seen that the current caused by only Sn^+ ions (and higher-energy "artifact" ions) is much smaller than the currents including Sn^{3+} and Sn^{2+} ions. At the abovementioned lowest

energy, with an already weak ion beam, this leads to a very large uncertainty in the extracted quantity N^+. The double capture cross section σ_{31} reacts stronger to a change in N^+ than the single capture cross section σ_{32} (compare Eq. 4.6 to Eq. 4.7). All this leads to a very large uncertainty in σ_{31} at 0.4 eV/u $((11.7 \pm 9.5) \times 10^{-16} \text{ cm}^2)$ and this data point is therefore not plotted. For the highest two energies (above 100 eV/u), σ_{31} is also not plotted because it could not reliably be determined. At these energies, the retarding voltages V_c and V_d (see Figure 4.2) are high (≈ 10 kV). Significant fluctuations in the measured current were observed at these high voltages, possibly caused by electrons emitted from the grids and by discharges between the grids. These fluctuations made a reliable determination of f, and thereby of σ_{31}, impossible. The effect on the single capture cross section was however small and is included in the plotted uncertainties.

Similarly to our previous work, we also performed the experiments for a D_2 target. In the following, we will compare our H_2 data to the D_2 data and also to our previous work.

First we focus on the single electron capture cross section. Figure 4.5 shows the present experimental results for both H_2 and D_2 targets as well as the experimental results obtained in Chapter 2 and two curves from semiclassical calculations. It can be seen that the cross sections obtained for H_2 and for D_2 are in general very similar. When only looking at the present D_2 data, one may conclude that the cross section is rather energy dependent. It maximizes around 20 eV/u and decreases fast for lower energies and more slowly for higher energies. However, most of the data points lie within, or close to, the error bars of the H_2 data, for which the maximum is much more shallow. With the present uncertainties, it is hard to say if the difference is real. There could be an isotope effect, but it cannot be a large effect.

The comparison of the present "new" data to the "old" data of Chapter 2 is very interesting. First of all, for a D_2 target, the new and old data are in excellent agreement with each other. For H_2, the present data also aligns very well with the old data in the energy range 150–430 eV/u, but does not support the remarkable increase of the old data points in the range 80–130 eV/u. The lowest-energy old data point even exceeds the cross section predicted by the classical over-barrier model [21] $(51 \times 10^{-16} \text{ cm}^2)$, which is considered a hard upper limit for the cross section as the model assumes 100% capture probability within a certain capture radius. Because of that, and because for D_2 there is agreement over the full energy range, and for H_2 the new data does align well with the old higher energy points, we believe that the four old data points between 80 and 130 eV/u are outliers. The old method relies on measuring
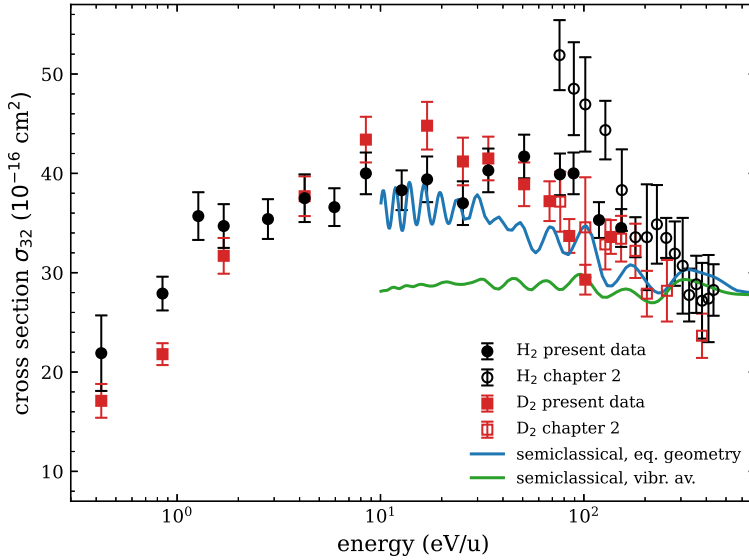
Figure 4.5: Single electron capture cross section for Sn^{3+} ions colliding with hydrogen molecules, as a function of ion energy in eV/u. Experimental values, for both H_2 and D_2 targets, obtained from the present experiment as well as from Chapter 2 are plotted. Results of two semiclassical calculations for Sn^{3+}–H_2 are included as solid lines. The first (blue) is obtained with the H–H internuclear distance fixed at the equilibrium distance, and is identical to the calculation of Chapter 2. The second curve (green) is obtained by taking an average of calculations over the range of internuclear distances of a vibrating H_2 molecule.

the difference in beam current with and without the gas target present, and is therefore much more reliant on exact beam alignment to the Faraday cup. Beam broadening and scattering could have influenced the measurements in case of a broad or off-centered ion beam. That means that the remarkable strong increase in cross section upon decreasing energy as seen in Chapter 2 is most likely an artifact of the old measurement procedure. Instead, we believe that upon decreasing the energy starting from 400 eV/u, the cross section does increase until it reaches a shallow maximum around 20 eV/u, and then increasingly falls off again upon going down to lower energies.

This observed behaviour is in rather good agreement with the semiclassical calculation of Chapter 2, also plotted in Figure 4.5. The increase there is however not as strong as seen in the experiments. As explained in Chapter 2, this calculation makes use of the Franck-Condon approximation, meaning
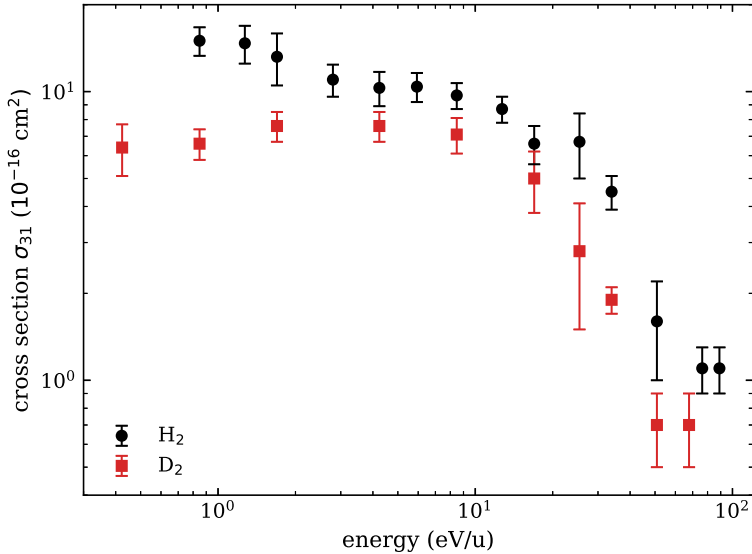
Figure 4.6: Double electron capture cross section for Sn^{3+} ions colliding with H_2 and D_2 molecules, as a function of ion energy in eV/u.

that the H–H internuclear distance remains fixed at the equilibrium distance during the interaction. Motivated by the findings in Chapter 2, a preliminary attempt to improve on this calculation is also plotted in the figure. It attempts to include the effect of vibrational motion in the H_2 molecule by taking the average of several Franck-Condon calculations, each with a different H–H internuclear distance sampled from the distribution of internuclear distances of a H_2 molecule in the vibrational ground state. The resulting cross sections show almost no dependence on energy. This method clearly shows worse agreement with the experimental data than the initial calculation. We therefore believe that the attempted method is not suitable for including vibrational effects. It seems however, that it is not needed to do so yet. At least down until 10 eV/u, the semiclassical method with Franck-Condon approximation is in rather good agreement with the experimental data. At the time of writing this thesis, there are no theoretical data yet at lower energies.

Next, we take a closer look at the double capture cross section. Figure 4.6 shows the results for both H_2 and D_2 targets. The cross sections for D_2 show a similar sharp and large increase upon decreasing energy as already seen for H_2 in Figure 4.4, although a few small differences are visible. First of all, the cross sections for D_2 are all approximately 25% smaller than for H_2. Second,
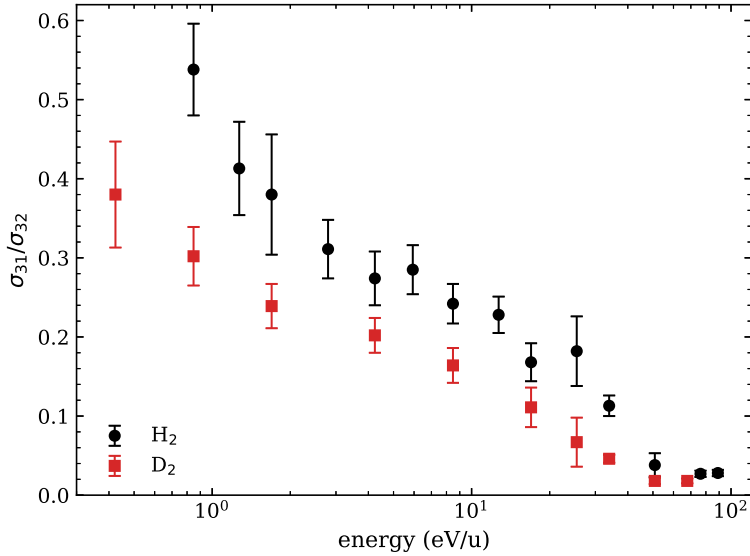
Figure 4.7: Ratio of the single to the double electron capture cross section for Sn^{3+} ions colliding with H_2 and D_2 molecules, as a function of ion energy in eV/u.

the cross section does not keep increasing towards lower energies but saturates. Third, and most interesting, is that the sharpest increase seems to occur at a slightly lower energy than for H_2, but it could also be caused by the D_2 data points lying below the H_2 points. Therefore, in Figure 4.7 we plot the ratios of the single capture to the double capture cross section for both H_2 and D_2 targets. For both targets, the ratio is constant at a very small value at the highest energies, and monotonically increases towards lower energies. The ratio is consistently larger for H_2. It might be that the ratio starts to increase at a slightly higher energy for H_2 compared to D_2, but more accurate measurements are needed to confirm this.

From Figures 4.6 and 4.7 it is clear that the double capture cross section is low for energies of approximately 80 eV/u. In Chapter 2, the double capture fraction f was estimated over the energy range 80–430 eV/u to be $(11 \pm 4)\%$. In the current work we find a much lower value of f at 80 eV/u, namely 2–3%. The number from Chapter 2 was obtained via a rather complicated method of fitting Gaussian peaks in a ToF spectrum (see Section 2.2.4). Since the present measurement technique directly measures the number of Sn^+ particles, we have more confidence in the present results.

The experimental finding that the double capture cross section can attain

substantial values is both important and remarkable. It is important because it identifies another channel for higher-charged ions emitted by the LPP to become singly charged, next to the channel found in Chapter 3 (through single capture from metastable Sn^{2+*}). This is relevant for ion mitigation simulations, since the stopping cross sections of Sn^+ ions seem to be larger than for Sn^{2+} ions [19]. The observation is unexpected, because the process is not exothermic but endothermic by no less than 6 eV and is therefore expected to have only a very small cross section ($< 10^{-16}$ cm^2). The electronic structure of Sn^{3+}, $[Kr]4d^{10}5s$, is such that excited states can always cascade back to the ground state (with $\Delta l = \pm 1$), typically within 10 ns. That means that no metastable states exist for Sn^{3+} that could change the process from endothermic to exothermic, as was the case for Sn^{2+} in Chapter 3.

The other way in which this process could become exothermic is when less energy is needed for removing both electrons from the H_2 molecule. In the Franck-Condon picture, this energy is determined by the vertical transition from the potential well of ground state H_2 to the repulsive $H^+ + H^+$ Coulomb curve, depicted by the blue and red arrows in Figure 4.8. Now, if the internuclear distance increases slightly after capture of the first electron, it can be seen that less energy is needed for the capture of the second electron. The figure shows that an increase from 0.74 Å to 1.1 Å is enough to make the process exothermic. This mechanism might explain the remarkable large double capture cross sections observed in the experiments at low energies. If the projectile velocity is low, there could be enough time during the interaction for the H–H internuclear distance to change. After removal of the first electron, the two positive nuclei are only bound by a single electron. The screening is thus reduced. The internuclear distance can then be expected to increase due to enhanced Coulomb repulsion, making the transition depicted by the green arrow possible. The bottom of the potential energy curve of the transient H_2^+ ion indeed lies around an internuclear separation of 1.1 Å [35]. Moreover, by assuming a separation of 10 a.u. between the two consecutive capture events, it can be calculated that the time between them becomes equal to the period of vibration of the H_2 molecule (8 fs) at a Sn projectile energy of 23 eV/u. This shows that there is indeed time for the molecule to relax at projectile energies below a few tens of eV/u. More involved calculations and more detailed potential energy curves, including the effect of the nearby Sn^{3+} ion, are required to determine whether this process is really the mechanism by which double electron capture in Sn^{3+}– H_2 collisions occurs. At the time of writing this thesis, theoretical efforts are made to include this effect in the framework of the semiclassical calculations. Measuring the energy of the
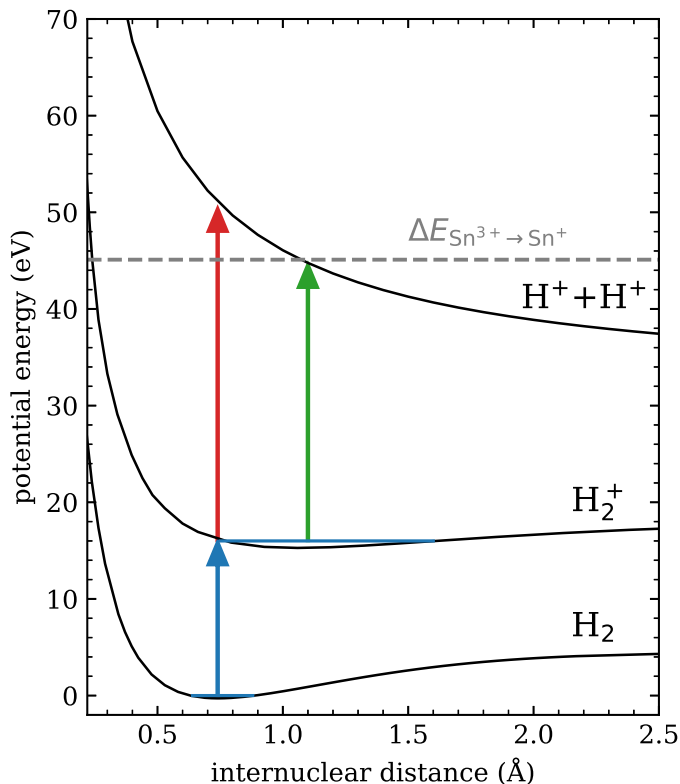
Figure 4.8: Potential energy curves for H_2, H_2^+, and $H^+ + H^+$, plotted from data tables of Ref. [35], together with an intuitive illustration of our proposed mechanism for double electron capture by Sn^{3+}. The dashed horizontal line indicates the amount of energy released when a Sn^{3+} ion takes two electrons to become Sn^+. The blue arrow depicts a vertical transition from the ground state of H_2 to a vibrational state of H_2^+, at the H_2 equilibrium internuclear distance. The red arrow depicts a vertical transition from the latter state to the Coulomb curve of the two protons, at the same internuclear distance. It can be seen that according to this vertical transition at fixed internuclear distance, double electron capture by Sn^{3+} from H_2 is endothermic by no less than 6 eV. However, if after the capture of the first electron, depicted by the blue arrow, the resulting H_2^+ ion would expand, less energy would be required for the capture of the second electron. The green arrow illustrates that from an internuclear distance of 1.1 Å onwards, this capture process becomes exothermic.

protons released by the double capture process could also provide information about the capture mechanism.

4.4 Conclusion

We have upgraded our crossed-beam setup with a deceleration stage and a retarding field analyzer and used it to measure single and double electron capture cross sections for low-energy Sn^{3+} ions impacting on H_2 (and D_2) molecules. The single capture cross section is found to have a shallow maximum of 40×10^{-16} cm^2 around an energy of 20 eV/u. The differences between the results for H_2 and D_2 are small. We do not see a strong energy dependence in the range 80–130 eV/u, as we saw in our previous study (Chapter 2). Our results are in good agreement with the semiclassical calculation of the previous study. An attempt to improve on that calculation, by including more H–H internuclear distances, shows worse agreement. The double capture cross section shows a remarkable, sharp increase by an order of magnitude upon decreasing the energy from 100 to 10 eV/u and keeps growing towards lower energies. The large cross sections are unexpected given that the process is substantially endothermic. We propose that at these low energies, the H–H internuclear distance could increase during the charge transfer interaction, which could make the capture of the second electron energetically favourable. More calculations and experiments are needed to confirm that this mechanism is the cause of the large double electron capture cross section at low energies.

References

[1] H. Weisen, M. von Hellermann, A. Boileau, L. D. Horton, W. Mandl, and H. P. Summers, "Charge exchange spectroscopy measurements of ion temperature and toroidal rotation in JET", *Nucl. Fusion* **29**, 2187 (1989).

[2] R. C. Isler, "An overview of charge-exchange spectroscopy as a plasma diagnostic", *Plasma Phys. Controlled Fusion* **36**, 171 (1994).

[3] R. Hoekstra, H. Anderson, F. W. Bliek, M. von Hellermann, C. F. Maggi, R. E. Olson, and H. P. Summers, "Charge exchange from D(n = 2) atoms to low-Z receiver ions", *Plasma Phys. Controlled Fusion* **40**, 1541 (1998).

[4] M. Reich, E. Wolfrum, J. Schweinzer, H. Ehmler, L. Horton, J. Neuhauser, and A. U. Team, "Lithium beam charge exchange diagnostic for edge ion temperature measurements at the ASDEX Upgrade tokamak", *Plasma Phys. Controlled Fusion* **46**, 797 (2004).

[5]   O. P. Ford, L. Vanó, J. A. Alonso, J. Baldzuhn, M. N. A. Beurskens, C. Bieder-
      mann, S. A. Bozhenkov, G. Fuchert, B. Geiger, D. Hartmann, R. J. E. Jaspers,
      A. Kappatou, A. Langenberg, S. A. Lazerson, R. M. McDermott, P. McNeely,
      T. W. C. Neelis, N. A. Pablant, E. Pasch, N. Rust, R. Schroeder, E. R. Scott,
      H. M. Smith, T. Wegner, F. Kunkel, R. C. Wolf, and W7-X Team, "Charge
      exchange recombination spectroscopy at Wendelstein 7-X", *Rev. Sci. Instrum.*
      91, 023507 (2020).

[6]   T. E. Cravens, "Comet Hyakutake x-ray source: Charge transfer of solar wind
      heavy ions", *Geophys. Res. Lett.* **24**, 105–108 (1997).

[7]   D. Bodewits, R. Hoekstra, B. Seredyuk, R. W. McCullough, G. H. Jones, and
      A. G. G. M. Tielens, "Charge Exchange Emission from Solar Wind Helium Ions",
      Astrophys. J. **642**, 593 (2006).

[8]   O. O. Versolato, "Physics of laser-driven tin plasma sources of EUV radiation
      for nanolithography", *Plasma Sources Sci. Technol.* **28**, 083001 (2019).

[9]   S. Rai, K. I. Bijlsma, L. Poirier, E. de Wit, L. Assink, A. Lassise, I. Rabadán,
      L. Méndez, J. Sheil, O. O. Versolato, and R. Hoekstra, "Evidence of production
      of keV Sn^+ ions in the H_2 buffer gas surrounding an Sn-plasma EUV source",
      Plasma Sources Sci. Technol. **32**, 035006 (2023), Note: this publication forms
      Chapter 3 of this thesis.

[10] V. Y. Banine, K. N. Koshelev, and G. H. P. M. Swinkels, "Physical processes in
      EUV sources for microlithography", *J. Phys. D: Appl. Phys.* **44**, 253001 (2011).

[11] V. Bakshi (ed), *EUV lithography*, 2nd edn, Bellingham, WA: SPIE Press, 2018.

[12] G. O'Sullivan, B. Li, R. D'Arcy, P. Dunne, P. Hayden, D. Kilbane, T. McCormack,
      H. Ohashi, F. O'Reilly, P. Sheridan, E. Sokell, C. Suzuki, and T. Higashiguchi,
      "Spectroscopy of highly charged ions and its relevance to EUV and soft X-ray
      source development", *J. Phys. B: At. Mol. Opt. Phys.* **48**, 144025 (2015).

[13] F. Torretti, J. Sheil, R. Schupp, M. M. Basko, M. Bayraktar, R. A. Meijer, S.
      Witte, W. Ubachs, R. Hoekstra, O. O. Versolato, A. J. Neukirch, and J. Colgan,
      "Prominent radiative contributions from multiply-excited states in laser-produced
      tin plasma for nanolithography", *Nat. Commun.* **11**, 1–8 (2020).

[14] A. Bayerle, M. J. Deuzeman, S. van der Heijden, D. Kurilovich, T. de Faria Pinto,
      A. Stodolna, S. Witte, K. S. E. Eikema, W. Ubachs, R. Hoekstra, and O. O.
      Versolato, "Sn ion energy distributions of ns-and ps-laser produced plasmas",
      Plasma Sources Sci. Technol. **27**, 045001 (2018).

[15] D. J. Hemminga, L. Poirier, M. M. Basko, R. Hoekstra, W. Ubachs, O. O.
      Versolato, and J. Sheil, "High-energy ions from Nd:YAG laser ablation of tin
      microdroplets: comparison between experiment and a single-fluid hydrodynamic
      model", *Plasma Sources Sci. Technol.* **30**, 105006 (2021).

[16] L. Poirier, A. Lassise, Y. Mostafa, L. Behnke, N. Braaksma, L. Assink, R. Hoekstra, and O. O. Versolato, "Energy-and charge-state-resolved spectrometry of tin laser-produced plasma using a retarding field energy analyzer", *Appl. Phys. B* **128**, 135 (2022).

[17] D. Nakamura, K. Tamaru, Y. Hashimoto, T. Okada, H. Tanaka, and A. Takahashi, "Mitigation of fast ions generated from laser-produced Sn plasma for extreme ultraviolet light source by H_2 gas", *J. Appl. Phys.* **102**, 123310 (2007).

[18] I. Fomenkov, D. Brandt, A. Ershov, A. Schafgans, Y. Tao, G. Vaschenko, S. Rokitski, M. Kats, M. Vargas, M. Purvis, R. Rafac, B. L. Fontaine, S. D. Dea, A. LaForge, J. Stewart, S. Chang, M. Graham, D. Riggs, T. Taylor, M. Abraham, and D. Brown, "Light sources for high-volume manufacturing EUV lithography: technology, performance, and power scaling", *Adv. Opt. Techn.* **6**, 173–186 (2017).

[19] D. Abramenko, M. Spiridonov, P. Krainov, V. Krivtsun, D. Astakhov, V. Medvedev, M. van Kampen, D. Smeets, and K. Koshelev, "Measurements of hydrogen gas stopping efficiency for tin ions from laser-produced plasma", *Appl. Phys. Lett.* **112**, 164102 (2018).

[20] J. Scheers, C. Shah, A. Ryabtsev, H. Bekker, F. Torretti, J. Sheil, D. A. Czapski, J. C. Berengut, W. Ubachs, J. R. Crespo López-Urrutia, R. Hoekstra, and O. O. Versolato, "EUV spectroscopy of highly charged Sn^{13+}-Sn^{15+} ions in an electron-beam ion trap", *Phys. Rev. A* **101**, 062511 (2020).

[21] A. Niehaus, "A classical model for multiple-electron capture in slow collisions of highly charged ions with atoms", *J. Phys. B: At. Mol. Phys.* **19**, 2925–2937 (1986).

[22] S. Rai, K. I. Bijlsma, I. Rabadán, L. Méndez, P. A. J. Wolff, M. Salverda, O. O. Versolato, and R. Hoekstra, "Charge exchange in collisions of 1–100-keV Sn^{3+} ions with H_2 and D_2", *Phys. Rev. A* **106**, 012804 (2022), Note: this publication forms Chapter 2 of this thesis.

[23] R. Geller, "Electron cyclotron resonance sources: Historical review and future prospects (invited)", *Rev. Sci. Instrum.* **69**, 1302–1310 (1998).

[24] R. A. Phaneuf, C. C. Havener, G. H. Dunn, and A. Müller, "Merged-beams experiments in atomic and molecular physics", *Rep. Prog. Phys.* **62**, 1143 (1999).

[25] B. van Zyl, N. Utterback, and R. Amme, "Generation of fast atomic hydrogen", *Rev. Sci. Instr.* **47**, 814 (1976).

[26] C. C. Havener, M. S. Huq, H. F. Krause, P. A. Schultz, and R. A. Phaneuf, "Merged-beams measurements of electron-capture cross sections for O^{5+}", *Phys. Rev. A* **39**, 1725 (1989).

[27] R. Hoekstra, J. P. M. Beijers, A. R. Schlatmann, R. Morgenstern, and F. J. de Heer, "State-selective charge transfer in slow collisions of C^{4+} with H and H_2", *Phys. Rev. A* **41**, 4800 (1990).

[28] G. Lubinski, Z. Juhász, R. Morgenstern, and R. Hoekstra, "Low-energy state-selective charge transfer by multiply charged ions", *Phys. Rev. Lett.* **86**, 616 (2001).

[29] G. Lubinski, "Light - a fingerprint of astrophysical processes", English, PhD thesis (University of Groningen, 2001).

[30] E. Bodewits, H. Bekker, A. de Nijs, R. Hoekstra, D. Winklehner, B. Daniel, G. Kowarik, K. Dobes, and F. Aumayr, "Electron emission yields from boron-like Ar ions impinging on Au(100)", *Nucl. Instrum. Methods Phys. Res., Sect. B* **269**, 1203–1207 (2011).

[31] S. T. de Zwart, A. G. Drentje, A. L. Boers, and R. Morgenstern, "Electron emission induced by multiply charged Ar ions impinging on a tungsten surface", *Surf. Sci.* **217**, 298–316 (1989).

[32] J. Rajput, A. Roy, D. Kanjilal, R. Ahuja, and C. P. Safvan, "An electrostatic deceleration lens for highly charged ions", *Rev. Sci. Instrum.* **81**, 043301 (2010).

[33] Y. Sakai and I. Katsumata, "An Energy Resolution Formula of a Three Plane Grids Retarding Field Energy Analyzer", *Jpn. J. Appl. Phys.* **24**, 337 (1985).

[34] J. R. Machacek, D. P. Mahapatra, D. R. Schultz, Y. Ralchenko, A. Chutjian, J. Simcic, and R. J. Mawhorter, "Measurement and calculation of absolute single- and double-charge-exchange cross sections for O^{6+} ions at 1.17 and 2.33 keV/u impacting He and H_2", *Phys. Rev. A* **90**, 052708 (2014).

[35] T. E. Sharp, "Potential-energy curves for molecular hydrogen and its ions", *At. Data Nucl. Data Tables* **2**, 119–169 (1971).

Electron capture from molecular hydrogen by metastable Sn^{2+*} ions

Abstract

Over a wide and partly overlapping energy range, the single electron capture cross sections for collisions of metastable $Sn^{2+}(5s5p\ ^3P^o)$ (Sn^{2+*}) ions with H_2 molecules have been measured (0.1–10 keV) and calculated (0.3–1000 keV). The semiclassical calculations use a close-coupling method in a basis of electronic wavefunctions of the $(SnH_2)^{2+}$ system. The experimental cross sections are extracted from double collisions in a crossed-beam experiment of Sn^{3+} with H_2. The measured capture cross sections for Sn^{2+*} show good agreement with the calculations between 2 and 10 keV, but increase towards lower energies whereas the calculations decrease. Additional Landau-Zener calculations were performed and show that inclusion of spin-orbit splitting cannot explain the large cross sections at the lowest energies which we now assume to be likely due to vibrational effects in the molecular hydrogen target.

5.1   Introduction

Latest-generation photolithography tools employ a laser-produced plasma (LPP) to generate extreme ultraviolet (EUV) light for writing the smallest features on silicon wafers in the production of computer chips [1–3]. In particular, a dense Sn plasma of about 40 eV in temperature is created in which Sn ions with charge states between 9+ and 15+ are the atomic sources of EUV light at 13.5 nm [4–8]. Energetic Sn ions are emitted from the plasma in lower charge states, typically from 4+ to 8+ [9–11], which is attributed to recombination in the peripheral part of the plasma [12]. To protect the plasma-facing optics from these energetic and highly charged ions, an H_2 buffer gas is introduced [2, 13]. Collisions of the Sn^{q+} ions with the H_2 molecules give rise to one- and two-electron capture reactions stepping down the average charge state of the ions. The initial steps down till Sn^{3+} are expected to happen rapidly due to the large cross sections for the higher charge states [11]. In the whole series of consecutive scattering events while travelling through the buffer gas, the ions' kinetic energy is reduced to values that allow for efficient mitigation of the Sn ions. Since it seems that the stopping power of Sn^+ is larger than that of Sn^{2+} ions [14], it is key to know whether the charge state lowering stops at 1+ or 2+. Given that the production of singly charged Sn ions by charge exchange from the Sn^{2+} ground state, i.e.

$$Sn^{2+}(5s^2\,{}^1S) + H_2({}^1\Sigma_g^+) \rightarrow Sn^+(5s^25p\,{}^2P^o) + H_2^+({}^2\Sigma_g^+), \qquad (5.1)$$
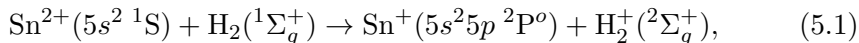
is endothermic with an energy difference of 1.3 eV for the Franck-Condon ionization of H_2 at its equilibrium distance, it has been believed that the consecutive charge state lowering basically stops at 2+. However, in a recent study [11] (Chapter 3), we have shown that the successive capture reactions do lead to the formation of Sn^+ ions. The work of Rai *et al.* [11] explains the high production of Sn^+ as a consequence of the preceding single capture reaction between Sn^{3+} and H_2, which was shown [15] (Chapter 2) to mainly produce long-lived metastable $Sn^{2+}(5s5p\,{}^3P^o)$ ions, i.e.

$$Sn^{3+}(5s\,{}^2S) + H_2({}^1\Sigma_g^+) \rightarrow Sn^{2+}(5s5p\,{}^3P^o) + H_2^+({}^2\Sigma_g^+), \qquad (5.2)$$
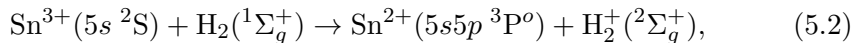
and just a very small fraction of ground state $Sn^{2+}(5s^2\,{}^1S)$ ions. For the metastable $Sn^{2+}(5s5p\,{}^3P^o)$ ions, single electron capture from H_2, i.e.

$$Sn^{2+}(5s5p\,{}^3P^o) + H_2({}^1\Sigma_g^+) \rightarrow Sn^+(5s^25p\,{}^2P^o) + H_2^+({}^2\Sigma_g^+), \qquad (5.3)$$
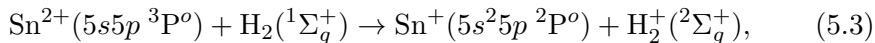
is not endothermic, but exothermic by 5.8 eV.

To underpin that very long-lived $Sn^{2+}(5s5p\ ^3P^o)$ metastable ions, later on denoted in short by Sn^{2+*} ions, are the gateway to produce singly charged Sn ions, Landau-Zener calculations of the capture cross section of Reaction 5.3 were performed by Rai *et al.* [11], leading to considerable cross sections on the order of 10^{-15} cm^2. In general, the collision energy at which the Landau-Zener cross section maximizes depends on the prefactor of the coupling matrix element. The prefactors of Olson and Salop [16] (determined for atomic hydrogen targets) and Kimura *et al.* [17] (from experiments on He) differ significantly and the associated energies at which the cross section maximizes differ by a factor of 8. There is no hard objective argument to prefer the H or He prefactor when having molecular hydrogen as a target. In the present work, we therefore present concerted theoretical and experimental efforts in obtaining more reliable cross sections.

We have carried out a close-coupling calculation of total cross sections for Reactions 5.1 and 5.3 using the method previously applied in [15] for $Sn^{3+} + H_2$ collisions. At energies which are most relevant for EUV plasma source applications, i.e., below 20 keV, we find that the cross section for electron capture by Sn^{2+*} is an order of magnitude larger than the one for ground state Sn^{2+}. Experimentally, to prevent issues with not well known metastable fractions in a Sn^{2+} ion beam, we performed crossed-beam studies with Sn^{3+} and H_2. By looking at double collision events, we effectively created a crossed-beam experiment of metastable Sn^{2+*} with H_2. In this way, we obtained total single electron capture cross sections for reaction (5.3) over the energy range from 0.1 to 10 keV.

5.2 Theoretical approach

The calculation method has been explained in Ref. [15]. Briefly, we employ a semiclassical treatment with nuclear straight-line trajectories, and the calculation assumes that the H–H internuclear distance is fixed during the collision (Franck-Condon approximation). This method is appropriate for intermediate collision energies. At low energies, the vibrational excitation of H_2 during the collision may be relevant. This effect is not included in the calculation method. At even lower energies, the nuclear motion of the projectile may need to be described with a wavefunction within a quantal formalism. In this respect, previous calculations on electron capture by doubly charged ions (O^{2+}, N^{2+}) from H, which also involved transitions at avoided crossings at relatively large internuclear distances, showed that the semiclassical method is appropriate

for energies higher than about 50 eV/u [18]. Accordingly, we have calculated the cross sections for $Sn^{2+*} + H_2$ at energies higher than 5 keV. However, to compare with the experiment and two-state models, we have extended the calculation down to 0.3 keV.

In the semiclassical approximation, the vector position of the ion with respect to the target center of mass, $\boldsymbol{R}(t)$, is a rectilinear trajectory $\boldsymbol{R} = \boldsymbol{b} + \boldsymbol{v}t$, where $\boldsymbol{b}$ is the impact parameter and $\boldsymbol{v}$ the ion–molecule relative velocity. The electronic wavefunction is the solution of the eikonal equation:

$$\left[H_{\text{el}} - i\frac{\partial}{\partial t} \right] \Psi = 0, \tag{5.4}$$

where H_{el} is the clamped-nuclei non-relativistic electronic Hamiltonian of the quasimolecule $(SnH_2)^{2+}$. In our treatment, the electronic motion is described by the wavefunction Ψ, which is expanded in terms of the (approximate) eigenfunctions, χ_k, of H_{el}:

$$\Psi(\boldsymbol{r}, t; \boldsymbol{v}, \boldsymbol{b}) = D(\boldsymbol{r}, t) \sum_k c_k(t) \chi_k(\boldsymbol{r}; \boldsymbol{R}) \exp\left(-i \int_0^t E_k(\boldsymbol{R}) \mathrm{d}t \right), \tag{5.5}$$

where $\boldsymbol{r}$ are electronic coordinates and E_k the energies of the electronic wavefunctions χ_k. In the present calculation, the wavefunctions χ_k have been obtained in a multi-reference configuration interaction calculation, with the Gaussian basis set and the pseudopotential of the calculation of Ref. [15] for $(SnH_2)^{3+}$. The electronic wavefunctions were multiplied by a common translation factor, D [19], to ensure that the wavefunction (5.5) fulfills the initial condition.

In practice, to calculate the total cross sections for the processes (5.1) and (5.3), we have employed basis sets of three and six molecular electronic states, respectively, as seen in Figure 5.1. Due to the conservation of the total spin, both cases were run in independent calculations. For both systems, the basis includes the electronic states dissociating into $Sn^{2+}(5s^2\ ^1S) + H_2(X^1\Sigma_g^+)$ and $Sn^{2+}(5s5p\ ^3P^o) + H_2(X^1\Sigma_g^+)$, which correspond to the entrance channels of collisions (5.1) and (5.3), respectively. The basis set also includes the molecular states dissociating into $Sn^+(5s^25p\ ^2P^o) + H_2^+(X^2\Sigma_g^+)$ and $Sn^+(5s5p^2\ ^4P) + H_2^+(X^2\Sigma_g^+)$, the main capture channels, and the electronic state that correlates to $Sn^{2+}(5s^2\ ^1S) + H_2(^3\Sigma_u^+)$, which leads to dissociative excitation.

To evaluate orientation-averaged cross sections, we have considered ion trajectories with different orientations $(\hat{\boldsymbol{b}}, \hat{\boldsymbol{v}})$ with respect to the H_2 internuclear axis. As explained in previous works, for ion collisions with H_2, the symmetry
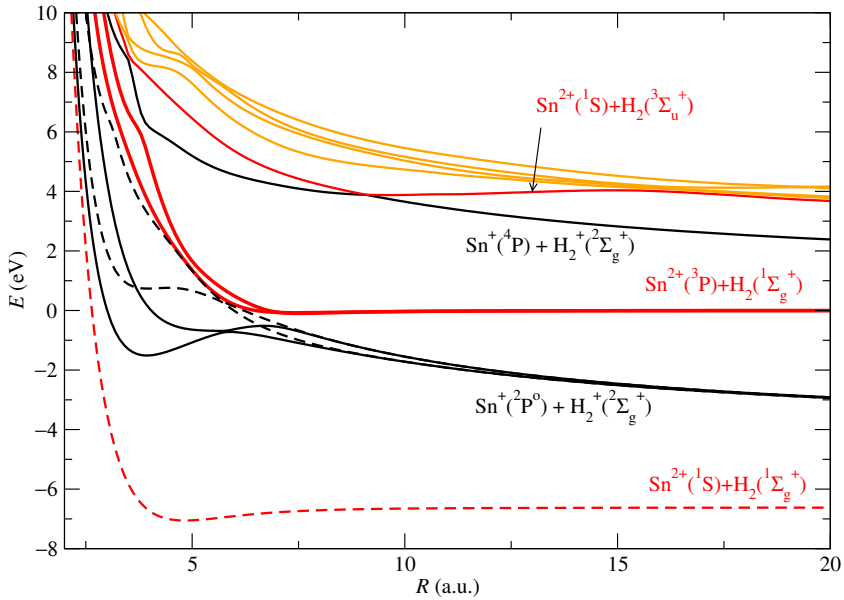
Figure 5.1: Potential energy curves of the $(SnH_2)^{2+}$ system as functions of the distance of the Sn nucleus to the midpoint of the H–H internuclear axis. The red lines are the energies of the electronic states correlating to $Sn^{2+} + H_2$. The black lines represent the energy curves of the states dissociating into $Sn^+ + H_2^+$. The orange lines are the energies of other states not included in the dynamical calculation. Solid and dashed lines correspond to triplet and singlet subsystems, respectively.

of the molecular target allows us to perform the orientation-average with three trajectory orientations [20]. In the first one (t1), the ion velocity is parallel to the H–H internuclear axis; for the second one (t2), the impact parameter is along the H–H internuclear axis; and the third one (t3) has both the impact parameter and the velocity perpendicular to the H–H internuclear axis. For each orientation, and for each value of the impact parameter, we substitute the expansion (5.5) into the eikonal equation, which yields a system of first order differential equations for the coefficients c_k. They are solved with the initial condition $c_k(t = -\infty) = \delta_{ik}$, where the index i corresponds to the collision entrance channel. The populations of the different electronic states of $(SnH_2)^{2+}$ are $|c_k|^2$, and the asymptotic values of these populations are the probabilities for transition to the collision channels. For $k \neq i$, they are:

$$P_{ik}(\boldsymbol{v}, \boldsymbol{b}) = \lim_{t \to \infty} |c_k|^2. \qquad (5.6)$$

The total cross section for a trajectory orientation is

$$\sigma_{ik}(v) = 2\pi \int_0^\infty b P_{ik}(v,b)\mathrm{d}b. \tag{5.7}$$

As mentioned above, our calculation employs potential energy cuts of the potential energy surfaces and non-adiabatic couplings obtained along the projectile trajectories t1, t2, and t3 [21]; the orientation-averaged total cross section is simply the mean value of the cross sections obtained with (5.7) for each trajectory orientation.

To illustrate the collision mechanism, we show in Figure 5.1 the cut of the electronic energies along a line that forms an angle of $60°$ with the H$-$H internuclear axis. Reaction (5.3) takes place through transitions from the degenerate entrance channels, $\mathrm{Sn}^{2+}(^3\mathrm{P}^o) + \mathrm{H}_2(\mathrm{X}^1\Sigma_g^+)$, to the capture channels $\mathrm{Sn}^+(^2\mathrm{P}^o)$ in the neighborhood of the avoided crossings at $R \approx 7$ a.u. The transitions at inner avoided crossings will populate the molecular state dissociating into $\mathrm{Sn}^+(5s5p^2\ ^4\mathrm{P}) + \mathrm{H}_2^+(\mathrm{X}^2\Sigma_g^+)$. One can note the very narrow avoided crossing between the energy curve of the $\mathrm{Sn}^+(^4\mathrm{P})$ channel with the curve of the dissociative excitation channel at $R \approx 9$ a.u. The energy of the ground state, correlating to the entrance channel $\mathrm{Sn}^{2+}(5s^2\ ^1\mathrm{S})$, is very low compared to those of the other electronic states and does not exhibit any avoided crossing.

Figure 5.2 shows the total cross sections for Sn^{2+} and Sn^{2+*}, for collision energies between 0.3 and 1000 keV. The cross sections for the individual trajectories t1, t2, and t3, not shown in the figure, differ by less than 10%, which reflects the quasi-isotropy of the projectile–target interaction at the distances where electron capture takes place. It should be noted that the lower part of the energy range, up to roughly 20 keV, is representative for Sn ions ejected from an LPP in an industrial photolithography machine. In this energy range, the cross sections for metastable Sn^{2+*} are an order of magnitude larger than the ones for ground state Sn^{2+}. Therefore, we focus our attention on Sn^{2+*}, i.e., reaction (5.3). Due to the endothermic nature of electron capture by ground state Sn^{2+} ions, their contribution only becomes relevant at high collision energies.

5.3   Experimental approach

An intuitive experimental approach to measure cross sections for Sn^{2+} and Sn^{2+*} would entail generating beams of Sn^{2+} ions in the ground ($5s^2\ ^1\mathrm{S}$) and metastable ($5s5p\ ^3\mathrm{P}^o$) state, separately, and measure their change in charge
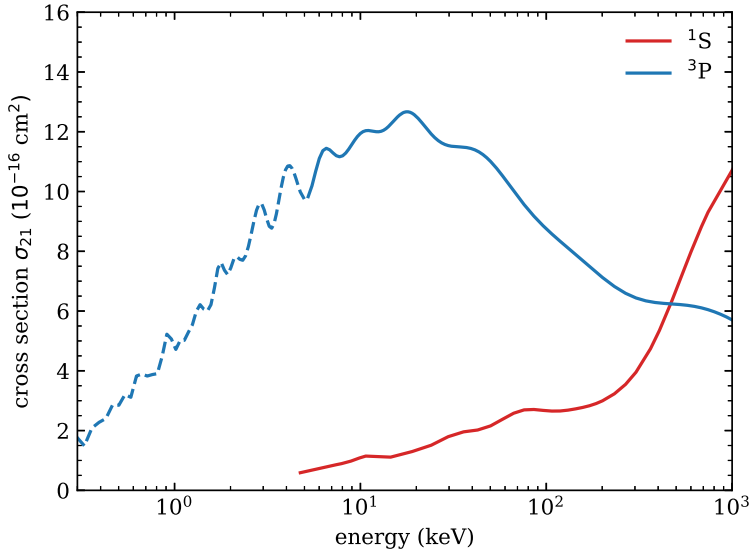
Figure 5.2: Total single electron capture cross section in collision of Sn^{2+} with H_2, as a function of the collision energy, both for ground state (^1S) and metastable (^3P) Sn^{2+}. The dashed line shows the extension of the ^3P calculation to lower energies where vibrational and nuclear quantum effects could be important.

state composition after traversing through a region of H_2 gas. However, it is very difficult to know and control the metastable fractions in an ion beam [22]. But, as mentioned in the introduction, we do know that in the energy regime relevant for EUV-LPPs, Sn^{3+} ions undergoing single electron capture with H_2 lead to Sn^{2+} ions almost exclusively in the $5s5p$ $^3P^o$ term. Therefore, in this work, we use a Sn^{3+} ion beam and extract the cross section for Sn^{2+*} from ions that undergo two collisions, capturing one electron each time, i.e., $Sn^{3+} \rightarrow Sn^{2+*} \rightarrow Sn^+$.

Recently, we measured single and double electron capture cross sections for Sn^{3+} ions colliding with molecular hydrogen [23] (Chapter 4), using an upgraded version of the crossed-beam setup used by Rai *et al.* [15]. The upgrade consists of a deceleration platform and the replacement of the Faraday cup by a retarding field analyzer (RFA), which allows us to measure individual charge states. In the current work, we make use of this upgraded setup. This setup and some parts of the measurement procedure are explained in detail in references [15, 23]. Here, the key points will be repeated and new elements of the data analysis procedure will be explained in more detail.

5.3.1 Experimental setup

The ZERNIKELEIF facility is used to generate a beam of 21 keV Sn^{3+} ions, which is subsequently transported to the crossed-beam setup. The latter is on an elevated potential to decelerate the ions to a desired energy just before entering the collision chamber. A six-element deceleration lens improves transmission. The ion beam traverses a jet of molecular hydrogen flowing from a capillary. Three values of gas flow are used, namely 1, 2.5, and 4 mL/min. These flows are high enough that measurable fractions of the ions undergo two charge exchange collisions. We are interested in the ions that undergo single electron capture twice. The ion beam is finally collected and analyzed by an RFA, which provides charge state resolution in the beam current. The next section explains how we extract the cross section for the second capture event from our measurements.

5.3.2 Measurement procedure

Starting from a Sn^{3+} beam, the relevant processes are described by the following differential equations:

$$\frac{dN^{3+}}{dz} = -(\sigma_{32} + \sigma_{31})nN^{3+} \tag{5.8a}$$

$$\frac{dN^{2+}}{dz} = \sigma_{32}nN^{3+} - (\sigma_{21} + \sigma_{20})nN^{2+} \tag{5.8b}$$

$$\frac{dN^{1+}}{dz} = \sigma_{31}nN^{3+} + \sigma_{21}nN^{2+} - \sigma_{10}nN^{1+} \tag{5.8c}$$

$$\frac{dN^{0+}}{dz} = \sigma_{20}nN^{2+} + \sigma_{10}nN^{1+}, \tag{5.8d}$$

where N^{q+} is the number of Sn^{q+} ions ($q = 0, 1, 2, 3$) as a function of distance z through a target of H_2 gas with number density n, and σ_{ij} denotes the cross section for charge exchange from Sn^{i+} to Sn^{j+}. Note that, with N^{2+}, we in fact mean the number of Sn^{2+*} ions here. Due to the absence of potential-energy curve crossings, $\sigma_{20} = \sigma_{10} = 0$, and we can exclude these processes from the analysis. The initial number of ions in the Sn^{3+} beam is N_0 and leads to the following initial condition: $N^{3+}(z = 0) = N_0$. The analytical solution to the initial value problem is given by the following expressions:

$$N^{3+} = N_0 e^{-(\sigma_{32}+\sigma_{31})nz}, \tag{5.9a}$$

$$N^{2+} = N_0 \frac{\sigma_{32}}{\sigma_{32}+\sigma_{31}-\sigma_{21}} \left(e^{-\sigma_{21}nz} - e^{-(\sigma_{32}+\sigma_{31})nz} \right), \tag{5.9b}$$

$$N^{+} = N_0 \frac{\sigma_{31}-\sigma_{21}}{\sigma_{32}+\sigma_{31}-\sigma_{21}} \left(1 - e^{-(\sigma_{32}+\sigma_{31})nz} \right) + N_0 \frac{\sigma_{32}}{\sigma_{32}+\sigma_{31}-\sigma_{21}} \left(1 - e^{-\sigma_{21}nz} \right).$$
$$\tag{5.9c}$$

We are interested in so-called double collision events, which turn a Sn^{2+} ion into a Sn^+ ion by reaction (5.3). We therefore define the following ratio:

$$f = \frac{N^+}{N^{2+}}, \tag{5.10}$$

which can be expected to increase with target density due to the occurence of more double collisions. To see how f scales with target density, we take a second-order Taylor expansion of Eqs. 5.9b and 5.9c and subsequently take the ratio. By ignoring quadratic terms in n in the resulting expression, we obtain:

$$f = \frac{\sigma_{31}}{\sigma_{32}} + \frac{1}{2} \frac{\sigma_{21}(\sigma_{32}+\sigma_{31})}{\sigma_{32}} nz. \tag{5.11}$$

In our experimental setup, we measure the ion numbers N^{q+} with the RFA. The position of the RFA in the chamber determines the total length L over which the ions traverse the molecular target. As in the previous studies [15, 23], we make use of the fact that the integral target density $nL = \int_0^L n(z)dz$ is proportional to the pressure P in the collision chamber. The constant of proportionality β is determined by calibrating the system with ions of known cross sections, in this case O^{6+} of Ref. [24]. By defining $f_0 = \frac{\sigma_{31}}{\sigma_{32}}$, Eq. 5.11 can be rewritten as

$$f = f_0 + \frac{1}{2}\sigma_{21}(1+f_0)\beta P. \tag{5.12}$$

In the experiments, we measure the ratio f at several values of target density, i.e., pressure. Figure 5.3 shows the results of a typical measurement. It shows that the ratio f is linear with pressure over our pressure range, justifying the linear approximation of Eq. 5.12. Figure 5.3 also shows a least-squares linear fit to the data. From the y-intercept (f_0) and the slope ($\frac{df}{dP}$), we can determine the cross section for process (5.3) using Eq. 5.12:

$$\sigma_{21} = \frac{2\frac{df}{dP}}{(1+f_0)\beta}. \tag{5.13}$$
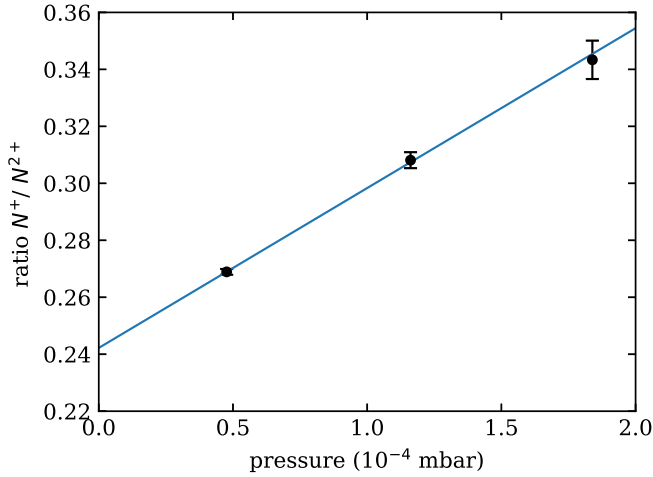
Figure 5.3: Ratio N^+/N^{2+}, i.e., f, measured at three H_2 pressures for incoming Sn^{3+} ions of 1 keV (black symbols). The blue line is a least-squares linear fit to the data. The resulting y-intercept and slope are used to calculate σ_{21} according to Eq. 5.13.

5.3.3   Uncertainties

The error bars in Figure 5.3 reflect the statistical uncertainty of one standard deviation in the measurement data. The fitting algorithm translates these into an uncertainty in f_0 and $\frac{df}{dP}$, which propagate into a (partial) uncertainty in σ_{21}. Another contribution to the uncertainty in σ_{21} is reproducibility. By repeating measurements on different days and with different ion beam settings, this contribution is found to be 20%. The quadratic sum of both contributions defines the total statistical uncertainty, and is depicted by the error bars plotted in the next section (Figure 5.4). The systematic uncertainty due to the calibration by the reference data, estimated to be 7%, is not included in the error bars.
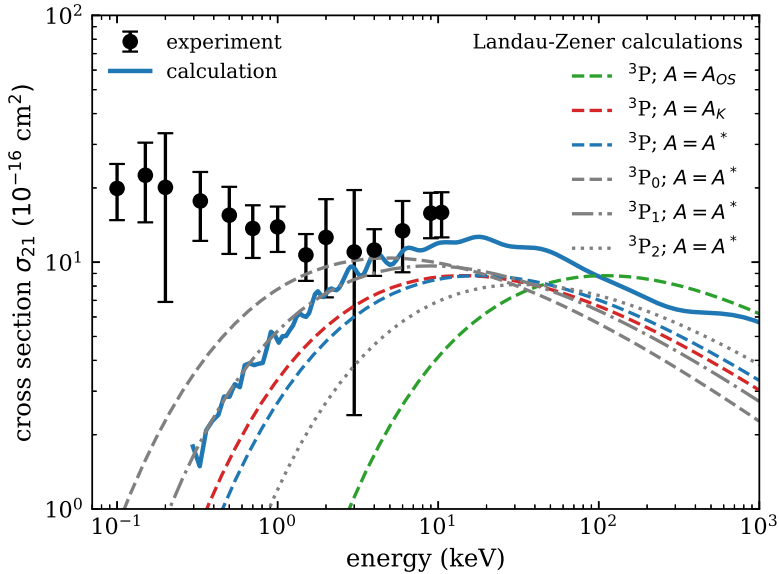
Figure 5.4: Single electron capture cross section for $Sn^{2+*}(^3P)$ + H_2. The solid blue line is the result of the semiclassical calculation, and the dots show the experimental results. The dashed green, red, and blue lines show the results of two-state Landau-Zener calculations of the ^3P term, assuming a statistical J distribution and capture into the $\nu' = 2$ vibrational state of H_2, which has the highest Franck-Condon factor. The green curve uses the prefactor of Olson and Salop [16], and the red curve uses the one from the work by Kimura *et al.* [17]. The prefactor was varied to match the semiclassical calculation best, resulting in a prefactor of 5.8 and the blue dashed line. This prefactor is subsequently used for Landau-Zener level-calculations, resulting in the lightgrey curves for $J = 0, 1, 2$.

5.4 Results and Discussion

Figure 5.4 shows both our calculated and measured cross sections for Sn^{2+*} (reaction (5.3)). In the energy range from 2 to 10 keV, there is good agreement, while below roughly 2 keV the experimental and calculated values start to diverge. The experimental values show an increasing trend when decreasing the energy down to 0.1 keV.

The entrance channel of the capture process (5.3) is a mixture of three spectroscopic levels $^3P^o_J$ with $J = 0, 1, 2$, while a single state, representing the ^3P term, has been considered in the non-relativistic theoretical description used in this paper. To determine the effect of the spin-orbit splitting, and to

investigate the possibility that a highly J-dependent cross section may explain the large experimental cross sections at low energies, exploratory Landau-Zener calculations have been performed. The results are also plotted in Figure 5.4. First, two-state calculations were performed with the ^{3}P term as entrance channel, assuming a statistical J distribution. Following Olson and Salop [16] as well as Magee [25], the coupling matrix element includes the Franck-Condon factor of the most probable vibrational state of H_2^+, which is $\nu' = 2$ [26], to account for the molecular nature of the target. As already mentioned in the introduction, the coupling matrix element has an empirical prefactor A. Commonly used values are $A_{OS} = 9.13$ proposed by Olson and Salop [16] and $A_K = 5.48$ proposed by Kimura *et al.* [17]. Calculations have been performed for both values. Both curves have a similar shape as the semiclassical calculation, but lie roughly 30% lower. The Kimura curve peaks at almost the same energy as the semiclassical curve, whereas the Olson-Salop curve peaks at one order of magnitude higher energy. This means that molecular hydrogen as a target is better approximated by a He atom than by a H atom. We however choose to optimize the prefactor such that it peaks at exactly the same energy as the semiclassical calculation, and find a value of 5.8, which we denote by A^*. This prefactor is subsequently used to perform Landau-Zener calculations for the three J levels. Because the spacing between those levels is smaller than the adiabatic splitting, we treat them independently instead of performing multichannel calculations. It can be seen from Figure 5.4 that the resulting curve for $J = 0$, and to a lesser extent also for $J = 1$, shifts up and its maximum moves to lower energies. From this, we may conclude that the J-distribution of the ^{3}P term is not statistical but has a preference for J equal to 0 and 1. However, the large experimental cross sections below 1 keV can still not be explained.

As already mentioned in Section 5.2, the semiclassical calculation does not take vibrational motion in the H_2 molecule into account. The vibrational period is equal to 8 fs. This should be compared to the interaction time between the projectile and the target. By assuming an interaction distance of 10 a.u., the interaction time of a 1 keV Sn ion is 13 fs, whereas it is 4 fs for a 10 keV Sn ion. This shows that, as the energy decreases from 10 keV, the limits of the applicability of the Franck-Condon approximation begin to be reached. We therefore believe that vibrational effects in the H_2 molecule are responsible for the increase in the cross section below 1 keV.

5.5 Conclusion

We have performed a joint theoretical and experimental study of single electron capture by Sn^{2+} ions from molecular hydrogen. Cross sections for this process are relevant for ion mitigation simulation codes used for modern EUV photolithography machines. The semiclassical calculations use a close-coupling method in a basis of electronic wavefunctions of the $(SnH_2)^{2+}$ system and make use of the Franck-Condon approximation (fixed H–H internuclear distance). Consistent with expectations based on binding energies, the calculations show that, at low energies relevant for EUV applications, the cross section for metastable $Sn^{2+}(5s5p\ ^3P^o)$ ions (Sn^{2+*}) is much larger compared to ground state $Sn^{2+}(5s^2\ ^1S)$ ions. The experimental cross sections for these Sn^{2+*} ions are extracted from double collisions in a crossed-beam experiment of Sn^{3+} with H_2. In the highest part of the overlapping energy range, i.e., from 2 to 10 keV, we find good agreement between calculation and experiment. For lower energies however, the measured cross sections increase whereas the calculated ones decrease. Additional Landau-Zener calculations were performed to investigate the role of the spin-orbit interaction. This interaction has a considerable effect on the cross sections for the three J levels, however it cannot explain the large measured cross sections at low energies. Since the interaction time becomes larger than the vibrational period of the H_2 molecule for a projectile energy below a few keV, we believe that vibrations become important at those energies. The break-down of the Franck-Condon approximation could be the reason for the discrepancy between theory and experiment at low energies.

5.6 Acknowledgements

References

[1] V. Y. Banine, K. N. Koshelev, and G. H. P. M. Swinkels, "Physical processes in EUV sources for microlithography", *J. Phys. D: Appl. Phys.* **44**, 253001 (2011).

[2] I. Fomenkov, D. Brandt, A. Ershov, A. Schafgans, Y. Tao, G. Vaschenko, S. Rokitski, M. Kats, M. Vargas, M. Purvis, R. Rafac, B. L. Fontaine, S. D. Dea, A. LaForge, J. Stewart, S. Chang, M. Graham, D. Riggs, T. Taylor, M. Abraham, and D. Brown, "Light sources for high-volume manufacturing EUV lithography: technology, performance, and power scaling", *Adv. Opt. Techn.* **6**, 173–186 (2017).

[3] V. Bakshi (ed), *EUV lithography*, 2nd edn, Bellingham, WA: SPIE Press, 2018.

[4] W. Svendsen and G. O'Sullivan, "Statistics and characteristics of xuv transition arrays from laser-produced plasmas of the elements tin through iodine", *Phys. Rev. A* **50**, 3710–3718 (1994).

[5] G. O'Sullivan, B. Li, R. D'Arcy, P. Dunne, P. Hayden, D. Kilbane, T. McCormack, H. Ohashi, F. O'Reilly, P. Sheridan, E. Sokell, C. Suzuki, and T. Higashiguchi, "Spectroscopy of highly charged ions and its relevance to EUV and soft X-ray source development", *J. Phys. B: At. Mol. Opt. Phys.* **48**, 144025 (2015).

[6] J. Colgan, D. Kilcrease, J. Abdallah, M. Sherrill, C. Fontes, P. Hakel, and G. Armstrong, "Atomic structure considerations for the low-temperature opacity of Sn", *High Energy Density Phys.* **23**, 133–137 (2017).

[7] O. O. Versolato, "Physics of laser-driven tin plasma sources of EUV radiation for nanolithography", *Plasma Sources Sci. Technol.* **28**, 083001 (2019).

[8] F. Torretti, J. Sheil, R. Schupp, M. M. Basko, M. Bayraktar, R. A. Meijer, S. Witte, W. Ubachs, R. Hoekstra, O. O. Versolato, A. J. Neukirch, and J. Colgan, "Prominent radiative contributions from multiply-excited states in laser-produced tin plasma for nanolithography", *Nat. Commun.* **11**, 1–8 (2020).

[9] S. Fujioka, H. Nishimura, K. Nishihara, M. Murakami, Y.-G. Kang, Q. Gu, K. Nagai, T. Norimatsu, N. Miyanaga, Y. Izawa, K. Mima, Y. Shimada, A. Sunahara, and H. Furukawa, "Properties of ion debris emitted from laser-produced mass-limited tin plasmas for extreme ultraviolet light source applications", *Appl. Phys. Lett.* **87**, 241503 (2005).

[10] L. Poirier, A. Bayerle, A. Lassise, F. Torretti, R. Schupp, L. Behnke, Y. Mostafa, W. Ubachs, O. O. Versolato, and R. Hoekstra, "Cross-calibration of a combined electrostatic and time-of-flight analyzer for energy-and charge-state-resolved spectrometry of tin laser-produced plasma", *Appl. Phys. B* **128** (2022).

[11] S. Rai, K. I. Bijlsma, L. Poirier, E. de Wit, L. Assink, A. Lassise, I. Rabadán, L. Méndez, J. Sheil, O. O. Versolato, and R. Hoekstra, "Evidence of production of keV Sn$^+$ ions in the H$_2$ buffer gas surrounding an Sn-plasma EUV source", *Plasma Sources Sci. Technol.* **32**, 035006 (2023), Note: this publication forms Chapter 3 of this thesis.

[12]   R. A. Burdt, Y. Ueno, Y. Tao, S. Yuspeh, M. S. Tillack, and F. Najmabadi, "Recombination effects during expansion into vacuum in laser produced Sn plasma", *Appl. Phys. Lett.* **97**, 041502 (2010).

[13]   D. Nakamura, K. Tamaru, Y. Hashimoto, T. Okada, H. Tanaka, and A. Takahashi, "Mitigation of fast ions generated from laser-produced Sn plasma for extreme ultraviolet light source by H_2 gas", *J. Appl. Phys.* **102**, 123310 (2007).

[14]   D. Abramenko, M. Spiridonov, P. Krainov, V. Krivtsun, D. Astakhov, V. Medvedev, M. van Kampen, D. Smeets, and K. Koshelev, "Measurements of hydrogen gas stopping efficiency for tin ions from laser-produced plasma", *Appl. Phys. Lett.* **112**, 164102 (2018).

[15]   S. Rai, K. I. Bijlsma, I. Rabadán, L. Méndez, P. A. J. Wolff, M. Salverda, O. O. Versolato, and R. Hoekstra, "Charge exchange in collisions of 1–100-keV Sn^{3+} ions with H_2 and D_2", *Phys. Rev. A* **106**, 012804 (2022), Note: this publication forms Chapter 2 of this thesis.

[16]   R. E. Olson and A. Salop, "Electron transfer between multi charged ions and neutral species", *Phys. Rev. A* **14**, 579 (1976).

[17]   M. Kimura, T. Iwai, Y. Kaneko, N. Kobayashi, A. Matsumoto, S. Ohtani, K. Okuno, S. Takagi, H. Tawara, and S. Tsurubuchi, "Landau-Zener Model Calculations of One-Electron Capture from He Atoms by Highly Stripped Ions at Low Energies", *J. Phys. Soc. Jpn.* **53**, 2224–2232 (1984).

[18]   P. Barragán, L. F. Errea, L. Méndez, I. Rabadán, and A. Riera, "Electron capture in collisions of N^{2+} and O^{2+} ions with $H(1s)$ at low impact energies", *Phys. Rev. A* **74**, 024701 (2006).

[19]   S. B. Schneiderman and A. Russek, "Velocity-Dependent Orbitals in Proton-On-Hydrogen-Atom Collisions", *Phys. Rev.* **181**, 311–321 (1969).

[20]   L. F. Errea, J. D. Gorfinkiel, A. Macías, L. Méndez, and A. Riera, "Implementation of the sudden approximation eikonal method in ion - diatom collisions", *J. Phys. B: At. Mol. Opt. Phys.* **30**, 3855 (1997).

[21]   I. Rabadán and L. Méndez, "Orientation effects in ion-molecule collisions", *J. Phys.: Conf. Ser.* **875**, 012009 (2017).

[22]   R. F. Welton, T. F. Moran, and E. W. Thomas, "Metastable state abundances in multiply charged ion beams", *J. Phys. B: At. Mol. Opt. Phys.* **24**, 3815–3823 (1991).

[23]   K. Bijlsma, L. Assink, L. Oltra, I. Rabadán, E. de Wit, A. Kleinsmit, E. Lalkens, M. Salverda, O. O. Versolato, L. Méndez, and R. Hoekstra, "Single and double electron capture in low-energy collisions of Sn^{3+} ions with molecular hydrogen", *in preparation* (2024), Note: this manuscript forms Chapter 4 of this thesis.

[24] J. R. Machacek, D. P. Mahapatra, D. R. Schultz, Y. Ralchenko, A. Chutjian, J. Simcic, and R. J. Mawhorter, "Measurement and calculation of absolute single- and double-charge-exchange cross sections for O^{6+} ions at 1.17 and 2.33 keV/u impacting He and H_2", *Phys. Rev. A* **90**, 052708 (2014).

[25] J. L. Magee, "Charge neutralization by reaction between positive and negative ions", *Discuss. Faraday Soc.* **12**, 33–44 (1952).

[26] M. Wacks, "Franck-Condon factors for ionization of H_2, HD and D_2", *J. Res. Natl. Bur. Stand., Sect. A* **68**, 631 (1964).

Conclusion and outlook

This thesis has established electron capture cross sections for doubly and triply charged Sn ions colliding with molecular hydrogen over the full energy range relevant for EUV source applications. Whereas upon straightforward calculation of a reaction energy balance one would expect that the conversion of highly charged Sn ions from the LPP to lower charged Sn ions by electron capture in the buffer gas would stop at Sn^{2+}, we have found two reaction pathways that efficiently produce Sn^+ particles. The first is double electron capture by Sn^{3+} ions and the second is single electron capture by metastable Sn^{2+*} ions. Both processes should be included in industrial simulation models of Sn ions traversing the H_2 buffer gas in an EUV source. By using the cross sections obtained in this thesis in such models, together with estimations for the higher charge states, one can predict at which positions in the source the ions convert from 3+ to 2+ and to 1+. Since the stopping power is different for these different charge states, this is important information for optimization of the hydrogen buffer gas conditions and thereby for the overall source performance.

The research initially motivated by an industrial application has revealed interesting fundamental physics. From an atomic physics perspective, a collision energy of a few keV is low. Because of the high mass of Sn, the collision velocity is very low at these energies. A consequence of this is that at energies below a few keV, the projectile-target interaction time becomes longer than the period of vibration of the H_2 molecule. We believe that this is the reason for the remarkably large double electron capture cross sections observed for Sn^{3+} and for the discrepancy between the experiment and the Franck-Condon calculation extended to lower energies for Sn^{2+*}.

Our experimental data, covering a wide energy range, are an ideal set of benchmark data for low-energy calculations. We can conclude that the semiclassical calculation framework described in this thesis is successful in describing electron capture in Sn–H_2 collisions down to energies of a few keV. At lower energies, the Franck-Condon approximation must be abandoned and

the motion of the hydrogen nuclei must be included.

Research is hardly ever finished. There are several topics and directions that would be interesting to study further. First of all, our experimental observations for double capture call for an extension of the calculation framework with the H–H internuclear distance being able to change during the interaction. With that, our proposed mechanism for double electron capture can be tested. In that respect, it would also be insightful to measure the energy of the protons released in the double capture event. Their energy is determined by the distance between them at the moment the second electron is captured. According to our proposed mechanism, their energy should be less than what would be expected from a pure vertical transition. It could also be interesting to refine the stepsize in projectile energy around the onset of the increase of the double capture cross section (see Figure 4.6 and 4.7). Since D_2 is heavier than H_2, its vibration period is longer. Therefore, we expect the increase towards lower energies to start at a lower energy. In our present data, this effect is however not conclusively visible.

The lifetime of the metastable $5s5p\ {}^3P_1$ level from Chapter 3 is not well known. For a better assessment of the contribution of this particular level, it is needed to measure this lifetime.

Now that the experimental setup and measurement procedure have been carefully developed and applied to the lower charge states of Sn, a natural next step would be to investigate the higher charge states of Sn coming from the LPP, i.e. 4+ to 8+. We expect the cross sections to be increasingly larger for higher charge states.

By improving the energy resolution of the ion detector in the crossed-beam setup, information about the energy transfer in a charge transfer interaction could be obtained. Possible ways to improve the energy resolution are to replace the grids in the retarding field analyzer by tubes, or to use an electrostatic analyzer instead of a retarding field analyzer. With the improved resolution, it would be possible to experimentally verify the important result of the semiclassical calculations that single capture by a keV Sn^{3+} ion populates the metastable $5s5p\ {}^3P$ term of Sn^{2+}. Moreover, the setup would be suited to measure stopping cross sections.

Summary

A large part of the technological progress that was seen over the last six decades may be partly attributed to integrated circuits having become more and more powerful and affordable. This has been made possible by ongoing innovations in the production process of the integrated circuits, and especially in the photolithography process. There, light is used for printing the fine structures constituting the semiconductor devices. Several times, industry has decreased the wavelength of the light used for this process, each time allowing smaller features to be patterned. The most advanced photolithography machines currently use extreme ultraviolet (EUV) light with a wavelength of 13.5 nm. This light is generated by firing a high-power laser pulse onto a microdroplet of Sn, creating a so-called laser-produced plasma of Sn. Under the right plasma circumstances, several multiply excited, highly charged Sn ions all emit light in a narrow bandwith around 13.5 nm. Carefully engineered multilayer mirrors are used for collecting and focusing the light. Energetic Sn ions emitted from the plasma need to be slowed down in order to prevent them from damaging the special hemispherical collector mirror. For that purpose, a hydrogen (H_2) buffer gas is used. A balance has to be found between maximal Sn ion stopping through collisional energy transfer to hydrogen molecules and minimal loss of EUV light through photo-absorption by the molecules. Simulation models are used to find optimal H_2 pressures and flows. Atomic data on collisions of Sn ions with H_2 molecules are required as input for these models, however, available data is scarce.

The ions emitted from the plasma typically have charges states of 4+ to 8+. Besides the transfer of energy, there can also be transfer of charge in a collision of a Sn ion with an H_2 molecule. The process in which a positively charged projectile particle moves past a neutral target particle and takes one or more target electrons is called electron capture and is also known as charge exchange or charge transfer. By capturing one or both of the electrons from the H_2 target, the charge state of the Sn ion reduces. The stopping power of the hydrogen

buffer gas is dependent on the charge state of the Sn ion. Electron capture is therefore an important process to include in above-mentioned optimization models, as the process influences which charge states are present at a given position in the buffer gas.

This thesis studies electron capture in collisions of Sn ions with H_2 molecules, a fundamental atomic physics process that occurs whenever Sn ions from a plasma are injected in a H_2 gas. For collisions of low-Z ions a wealth of data, both experimentally and theoretically is available, however for complex heavy ions, such as Sn, barely any data exists. We focus on the lower charge states, specifically the production of Sn^{2+} and Sn^+ ions out of Sn^{3+} ions, as the initial stages of charge state lowering in an EUV source are expected to happen quickly due to large electron capture cross sections.

Chapters 2 and 4 cover our study of electron capture in collisions of Sn^{3+} ions with H_2 molecules. By using direct (Chapter 2) and decelerated (Chapter 4) ion beams in our crossed-beam setup, we have measured over three orders of magnitude in ion energy, from 50 eV to 50 keV. The first series of experiments, described in Chapter 2, laid the foundation for this research and established the very first single electron capture cross sections for this collision system. Upon going down in energy from 50 to 10 keV, we observed an increasing cross section. Thereafter, to go to lower energies, a major upgrade of our complete setup was needed to work with decelerated ion beams, giving access to energies well below 10 keV. To do so, our complete setup was put on a high-voltage platform that allows us to decelerate incoming ions upon entering the setup. This required every single element of the setup to be operated remotely. At the same time, we replaced the Faraday cup as ion detector with a retarding field analyzer to improve and ease the measurement process by gaining charge state resolution. The follow-up research performed with this setup into the unexplored low-energy regime is described in Chapter 4. Overall, we find that the curve of the single electron capture cross section over our energy range has the shape of a shallow concave parabola, maximizing around an energy of 2 keV.

An important and remarkable finding is that the double electron capture cross section for Sn^{3+} attains high values at energies up to a few keV. At around 5 keV, the cross section sharply drops to values an order of magnitude smaller. The large cross section is unexpected given that the double capture process is substantially endothermic in this collision system. We propose the following mechanism that could explain the observations: at low projectile velocities, there may be enough time for the H–H internuclear distance to

increase enough after the capture of the first electron, to make the capture of the second electron by the same projectile also energetically favourable, due to a reduced Coulomb repulsion between the two protons.

In a collaboration with professors Rabadán and Méndez from the Theory of Atomic and Molecular Collisions group at the Autonomous University of Madrid, we could compare our experimental results for single electron capture to the results of semiclassical calculations. The calculation framework is described in Chapter 2 and the calculation covers the energy range 1–100 keV. For lower energies, the assumption of a fixed H–H internuclear distance (Franck-Condon approximation) is expected to become invalid. The calculated cross sections are in good agreement with our set of experimental results as presented in Chapter 4.

Chapter 3 reports ion measurements performed on an actual laser-produced plasma (LPP) from a Sn microdroplet. Charge-state resolved kinetic energy spectra of Sn ions coming from the plasma have been measured for different densities of the H_2 buffer gas surrounding the LPP. Without this buffer gas, energetic keV Sn ions in charge states from 4+ to 8+ are observed. Upon increasing the H_2 density, the charge state of the energetic ions shifts to lower values, down to only 2+ and 1+ at the highest measured density. Our observations are a clear sign of the occurrence of electron capture. However, it was beforehand expected that 2+ would be the lowest generated charge state, because from there on single electron capture from H_2 is no longer exothermic. The generation of Sn^+ through double capture from H_2 by Sn^{3+} is highly endothermic and was therefore not taken into consideration. With the knowledge of the later experiments with the upgraded crossed-beam setup, we now know that at energies below a few keV double capture can also generate Sn^+. We have proposed that the Sn^+ ions are generated through single electron capture not by ground state Sn^{2+} but by metastable Sn^{2+}: $Sn^{2+}(5s5p\ ^3P^o)$ (Sn^{2+*}). The theoretical work of Chapter 2 provides support for the required population of the metastable state. An estimate of the cross section for the single capture process by Sn^{2+*} is obtained through Landau-Zener calculations. After inclusion of the process in a simulation model of the Sn ions traversing the buffer gas, we find good agreement with the experimental observations.

In Chapter 5 we study the electron capture pathway identified in Chapter 3 more closely. Semiclassical calculations similar to the ones in Chapter 2 have been performed and show that at energies relevant for EUV applications, the single electron capture cross section for metastable Sn^{2+*} is indeed much larger than for ground state Sn^{2+}. By using our upgraded crossed-beam setup, we could extract the single electron capture cross section for Sn^{2+*} from double

collisions of Sn^{3+} ions with H_2. We find good agreement between experiment and calculation at the higher energies. However, at energies below 2 keV, where the validity of the Franck-Condon approximation is uncertain, they start to deviate. The measured cross sections increase whereas the calculated ones decrease. This hints at the vibrational motion as an ingredient that must be included in the low-energy calculations.

To conclude, this thesis has established electron capture cross sections for doubly and triply charged Sn ions colliding with molecular hydrogen over the full energy range relevant for EUV source applications. Whereas upon straightforward calculation of a reaction energy balance one would expect that the conversion of highly charged Sn ions from the LPP to lower charged Sn ions by electron capture in the H_2 buffer gas would stop at Sn^{2+}, we have found two reaction pathways that efficiently produce Sn^+ ions. The first is double electron capture by Sn^{3+} ions and the second is single electron capture by metastable Sn^{2+*} ions. Both processes should be included in industrial simulation models of Sn ions traversing the H_2 buffer gas in an EUV source.

At low collision energies, i.e., below a few keV, the projectile-target interaction time becomes longer than the period of vibration of the H_2 molecule. We believe that this is the reason for the remarkably large double electron capture cross sections observed for Sn^{3+} and for the discrepancy between the experiment and the Franck-Condon calculation extended to lower energies for Sn^{2+*}.

We can conclude that the semiclassical calculation framework described in this thesis is successful in describing electron capture in Sn–H_2 collisions down to energies of a few keV. At lower energies, the Franck-Condon approximation must be abandoned and the motion of the hydrogen nuclei must be included.

Samenvatting

Elektroneninvangst in botsingen van tin-ionen met moleculair waterstof

Een groot deel van de technologische vooruitgang van de laatste zes decennia kan deels toegeschreven worden aan het steeds krachtiger en goedkoper worden van geïntegreerde schakelingen. Dit is mogelijk gemaakt door voortdurende innovaties in het productieproces van geïntegreerde schakelingen, en in het bijzonder in de techniek genaamd fotolithografie. In deze techniek wordt licht gebruikt om de fijne structuren waaruit de geïntegreerde schakeling bestaat te "printen". De industrie heeft meerdere keren een stap gemaakt naar een kortere golflengte van het licht dat gebruikt wordt in dit proces, waarbij het elke keer mogelijk werd om kleinere structuren te printen. Tegenwoordig gebruiken de meest geavanceerde fotolithografiemachines extreem-ultraviolet (EUV) licht met een golflengte van 13.5 nm. Dit licht wordt gegenereerd door een zogenaamd lasergeproduceerdplasma van tin (Sn), welke gecreëerd wordt door het vuren van een hoogvermogenlaserpuls op een microdruppel van Sn. Onder de juiste plasmaomstandigheden zenden verschillende meervoudig aangeslagen en hooggeladen Sn-ionen licht uit met een golflengte van 13.5 nm. Een speciale hemisferische meerlaagse spiegel, de zogenaamde verzamelspiegel, wordt gebruikt voor het opvangen en focusseren van het licht. Om te voorkomen dat door het plasma uitgezonden energetische Sn-ionen de verzamelspiegel beschadigen wanneer ze deze raken, moeten deze ionen worden afgeremd. Om dat te bereiken wordt er een waterstof (H_2) buffergas gebruikt. Wanneer de Sn-ionen met hoge snelheid door het gas bewegen, zullen ze steeds een beetje energie verliezen wanneer ze met een waterstofmolecuul botsen. De keuze voor waterstofgas is onder andere gebaseerd op het feit dat het het gas is wat het minste EUV-licht absorbeert. Echter, de absorptie is niet nul. Er zal daarom een balans gevonden moeten worden tussen enerzijds het maximaal afremmen van Sn-ionen en anderzijds het minimaal verliezen van EUV-licht. Om de optimale H_2-druk en stroming te vinden worden simulatiemodellen

gebruikt. Voor deze modellen zijn fundamentele atomaire data over botsingen van Sn-ionen met H_2-moleculen nodig. Er zijn echter nauwelijks gegevens over deze processen bekend.

De door het plasma uitgezonden Sn-ionen hebben ladingstoestanden van 4+ tot 8+ en energieën variërend van sub-keV tot enkele keV's met uitschieters tot enkele tientallen keV's. Naast de overdracht van energie kan er ook lading worden overgedragen in een botsing van een Sn-ion met een H_2-molecuul. Het proces waarbij een positief geladen projectieldeeltje langs een neutraal doeldeeltje beweegt en daarbij één of meerdere elektronen van het doeldeeltje opneemt wordt elektroneninvangst genoemd en is ook bekend onder de termen ladingsoverdracht en ladingsuitwisseling. Door het invangen van één of beide elektronen van een H_2-molecuul zal de ladingstoestand van het Sn-ion afnemen. Het stopvermogen, de gemiddelde energieafname per eenheid lengte, van het waterstofbuffergas voor Sn-ionen hangt af van de ladingstoestand van het Sn-ion. Elektroneninvangst is daarom een belangrijk proces om op te nemen in bovengenoemde optimalisatiemodellen omdat het proces beïnvloedt welke ladingstoestanden aanwezig zijn op een bepaalde positie in het buffergas.

Het centrale thema van dit proefschrift is dan ook elektroneninvangst in botsingen van Sn-ionen met H_2-moleculen. Terwijl voor elektroneninvangst door ionen met een laag atoomnummer er veel data beschikbaar zijn, zowel experimenteel als theoretisch, zijn er voor complexe en zware ionen zoals Sn nauwelijks gegevens beschikbaar. Wij richten ons specifiek op de productie van Sn^{2+}- en Sn^{+}-ionen vanuit Sn^{3+}-ionen. Dit heeft meerdere redenen. Allereerst is de elektronische structuur van Sn^{3+}, $[Kr]4d^{10}5s$, gunstig voor zowel experiment als berekening omdat het een relatief eenvoudig systeem is met één valentie-elektron. De tweede reden voor de focus op de lagere ladingstoestanden is dat verwacht kan worden dat de eerste stappen in de reductie van ladingstoestand relatief snel zullen plaatsvinden, omdat hogere ladingstoestanden in het algemeen makkelijker een elektron kunnen invangen.

De belangrijkste methode welke gebruikt wordt in dit proefschrift om deze processen te bestuderen is een experimentele techniek genaamd gekruistebundelexperiment. Met de ZERNIKELEIF (Zernike low-energy ion beam facility) faciliteit van de Rijksuniversiteit Groningen wordt een bundel van energetische Sn-ionen gemaakt welke vervolgens in een speciaal ontwikkelde experimentele opstelling een bundel H_2-gas doorkruist. Door middel van metingen van de ionenbundelstroom kan de werkzame doorsnede (*cross section*), een grootheid welke gerelateerd is aan de waarschijnlijkheid van een proces, voor elektroneninvangst bepaald worden. Doel is om deze werkzame doorsnede over een zo breed

mogelijk energiebereik te bepalen. Voor energieën minder dan zo'n 10 keV is de creatie en het transport van de Sn-ionenbundels echter zodanig inefficiënt dat er geen experimenten mee gedaan kunnen worden. Om dit probleem op te lossen is tijdens het promotieproject de opstelling grondig aangepast en uitgebreid zodat de opstelling op hoogspanning kan opereren, wat het mogelijk maakt om de binnenkomende ionen af te remmen.

Dit proefschrift bevat meerdere publicaties in samenwerking met de "*Theory of Atomic and Molecular Collisions*"-groep van professoren Rabadán en Méndez van de Autonome Universiteit van Madrid (Universidad Autónoma de Madrid - UAM). Zij gebruiken zowel semiklassieke als kwantummechanische modellen voor het bestuderen van elektroneninvangstinteracties. Door het vergelijken van experimentele resultaten met resultaten van theoretische berekeningen kunnen beide methoden getoetst worden. Daarnaast kan er met behulp van de modellen meer inzicht verkregen worden in de atomaire mechanismen die de processen drijven.

Hoofdstukken 2 en 4 behandelen onze studie van elektroneninvangst in botsingen van Sn^{3+}-ionen met H_2-moleculen. Door gebruik te maken van directe (Hoofdstuk 2) en afgeremde (Hoofdstuk 4) ionenbundels hebben we metingen verricht in onze gekruistebundelopstelling voor ionen-energieën van 50 eV tot 50 keV. De eerste serie van experimenten, beschreven in Hoofdstuk 2, heeft de fundering gelegd voor dit onderzoek en heeft voor dit botsingssysteem voor de eerste keer werkzame doorsneden voor enkelvoudige elektroneninvangst vastgesteld. Deze werkzame doorsnede nam toe wanneer we de energie lieten afnemen over het bereik van 50 keV tot 10 keV. Zoals hierboven benoemd is daarna een upgrade aan de opstelling uitgevoerd om lagere energieën te kunnen bereiken. Daarnaast is de *Faraday cup* ionendetector vervangen door een *retarding field analyzer*. Doordat hiermee onderscheid gemaakt kan worden tussen ladingstoestanden van ionen kon het meetproces worden verbeterd. Het vervolgonderzoek wat is gedaan met deze verbeterde opstelling is beschreven in Hoofdstuk 4. Over het hele energiebereik vinden we dat de kromme van de werkzame doorsnede voor de invangst van één elektron de vorm van een bergparabool aanneemt met een maximum rond 2 keV.

Een belangrijke en opvallende bevinding is dat de werkzame doorsnede voor de invangst van twee elektronen door Sn^{3+} hoge waarden aanneemt voor energieën tot een paar keV. Rond 5 keV neemt deze werkzame doorsnede scherp af naar waarden welke een orde van grootte kleiner zijn. De grote werkzame doorsnede is onverwacht omdat de invangst van twee elektronen in substantiële mate endotherm is voor dit botsingssysteem, wat wil zeggen dat het proces

energie kost in plaats van oplevert. Wij stellen het volgende mechanisme voor dat de observaties zou kunnen verklaren: voor lage snelheden van het projectiel zou er genoeg tijd kunnen zijn voor de H–H internucleaire afstand om toe te nemen na de invangst van het eerste elektron, zodanig dat de invangst van het tweede elektron door hetzelfde projectiel ook energetisch gunstig is, doordat de Coulombafstoting tussen de protonen is afgenomen.

Wij hebben onze meetresultaten voor enkelvoudige elektroneninvangst vergeleken met de resultaten van semiklassieke berekeningen. Deze berekeningen zijn beschreven in Hoofdstuk 2 en zijn gedaan voor energieën van 1 tot 100 keV. Voor lagere energieën wordt verwacht dat de Franck-Condonbenadering, de aanname dat de H–H internucleaire afstand constant is, ongeldig wordt. De berekende werkzame doorsneden zijn in goede overeenstemming met onze experimentele resultaten gepresenteerd in Hoofdstuk 4.

Hoofdstuk 3 rapporteert ionenmetingen welke daadwerkelijk gedaan zijn aan een lasergeproduceerdplasma gemaakt vanuit een microdruppel van Sn. De verdelingen van kinetische energie, gescheiden per ladingstoestand, van Sn-ionen die door het plasma uitgestoten worden zijn gemeten voor verschillende dichtheden van het H_2-buffergas welke het plasma omringt. In afwezigheid van dit buffergas worden energetische (keV) Sn-ionen waargenomen met ladingstoestanden van 4+ tot 8+. Wanneer de H_2-dichtheid verhoogd wordt, verschuift de ladingstoestand van de energetische ionen naar lagere waarden, tot aan alleen nog maar 2+ en 1+ op de hoogst gemeten dichtheid. Onze observaties zijn een duidelijk teken van het plaatsvinden van elektroneninvangst. Echter, op voorhand werd verwacht dat 2+ de laagste ladingstoestand zou zijn welke gegenereerd wordt, omdat vanaf dan de invangst van één elektron van H_2 niet langer exotherm is. De generatie van Sn^+ door het invangen van twee elektronen van H_2 door Sn^{3+} is nóg meer endotherm en werd daarom hier nog niet beschouwd. Met de kennis van de latere experimenten met de verbeterde gekruistebundelopstelling weten we nu dat voor energieën lager dan een paar keV, tweevoudige elektroneninvangst ook Sn^+ kan genereren. We hebben voorgesteld dat de Sn^+-ionen worden gegenereerd door enkelvoudige elektroneninvangst door Sn^{2+}, welke zich echter niet in de grondtoestand bevindt maar in een metastabiele toestand: $Sn^{2+}(5s5p\ ^3P^o)$ (Sn^{2+*}). De benodigde bevolking van deze metastabiele toestand wordt ondersteund door het theoretische werk van Hoofdstuk 2. Een schatting van de werkzame doorsnede voor enkelvoudige elektroneninvangst door Sn^{2+*} is verkregen door Landau-Zenerberekeningen. Na het toevoegen van het proces aan een simulatiemodel van de Sn-ionen die door het buffergas bewegen, vinden we goede overeenkomst met de experimentele observaties.

In Hoofdstuk 5 bestuderen we het in Hoofdstuk 3 geïdentificeerde elektroneninvangstproces nader. Semiklassieke berekeningen, vergelijkbaar met de berekeningen uit Hoofdstuk 2, zijn gedaan en laten zien dat voor energieën welke relevant zijn voor EUV-toepassingen, de werkzame doorsnede voor enkelvoudige elektroneninvangst door metastabiel Sn^{2+*} inderdaad veel groter is dan door Sn^{2+} in de grondtoestand. Met onze aangepaste en verbeterde experimentele gekruisebundelopstelling hebben we de werkzame doorsnede voor enkelvoudige elektroneninvangst door Sn^{2+*} bepaald door te kijken naar dubbele botsingen in het systeem Sn^{3+}-op-H_2. We vinden goede overeenkomst tussen experiment en berekening voor de hogere energieën. Echter, voor energieën lager dan 2 keV, waar de geldigheid van de Franck-Condonbenadering onzeker is, beginnen de twee uiteen te lopen. De gemeten werkzame doorsneden nemen toe voor lagere energieën, terwijl de berekende waarden afnemen. Dit wijst erop dat de vibratiebeweging in het H_2-molecuul meegenomen moet worden in de berekeningen voor lage energieën.

Concluderend, dit proefschrift heeft de werkzame doorsneden voor elektroneninvangst in botsingen van tweevoudig en drievoudig geladen Sn-ionen met moleculair waterstof vastgesteld, over het volledige energiebereik welke relevant is voor EUV-brontoepassingen. Terwijl men, gebaseerd op een eenvoudige reactie-energiebalans, zou verwachten dat de omzetting van hooggeladen Sn-ionen uit het lasergeproduceerdplasma tot lager geladen Sn-ionen door elektroneninvangst in het buffergas zou stoppen bij Sn^{2+}, hebben wij twee reactiekanalen gevonden welke efficiënt tot Sn^+-ionen leiden. Het eerste kanaal is tweevoudige elektroneninvangst door Sn^{3+}-ionen en het tweede kanaal is enkelvoudige elektroneninvangst door metastabiele Sn^{2+*}-ionen. Beide processen zouden opgenomen moeten worden in simulatiemodellen van Sn-ionen welke door een H_2-gas bewegen in een EUV-bron. Door de in dit proefschrift verkregen werkzame doorsneden in deze modellen te gebruiken, samen met schattingen voor de hogere ladingstoestanden, kan men voorspellen op welke posities in de bron de ionen veranderen van 3+ naar 2+ en naar 1+. Omdat het stopvermogen verschillend is voor deze verschillende ladingstoestanden, is dit belangrijke informatie voor de optimalisatie van de conditie van het waterstofbuffergas, en daarmee voor de algehele prestatie van de EUV-bron.

Het onderzoek wat in eerste instantie gemotiveerd is door een industriële toepassing heeft interessante fundamentele natuurkunde blootgelegd. Vanuit het perspectief van de atoomfysica is een botsingsenergie van een paar keV laag. Vanwege de hoge massa van Sn, is de botsingssnelheid erg laag op deze energieën. Als gevolg hiervan wordt bij energieën lager dan een paar keV, de interactietijd

tussen projectieldeeltje en doeldeeltje langer dan de vibratieperiode van het H_2-molecuul. Wij denken dat dit de reden is voor de opvallend grote waargenomen werkzame doorsneden voor tweevoudige elektroneninvangst door Sn^{3+} en voor de discrepantie tussen het experiment en de naar lagere energieën uitgebreide Franck-Condonberekening voor Sn^{2+*}.

Onze experimentele data, welke een breed energiebereik omvatten, zijn een ideale maatstaf voor lage-energieberekeningen. We kunnen concluderen dat het raamwerk van semiklassieke berekeningen beschreven in dit proefschrift succesvol is in het beschrijven van elektroneninvangst in Sn-H_2-botsingen voor energieën tot een minimum van een paar keV. Voor lagere energieën zal de Franck-Condonbenadering losgelaten moeten worden en zal de beweging van de waterstofkernen meegenomen moeten worden.

List of publications

1. K. Bijlsma, L. Oltra, E. de Wit, L. Assink, I. Rabadán, L. Méndez, and R. Hoekstra, "Electron Capture from Molecular Hydrogen by Metastable Sn^{2+*} Ions", *Atoms* **12**, 9 (2024).

2. S. Rai, K.I. Bijlsma, L. Poirier, E. de Wit, L. Assink, A. Lassise, I. Rabadán, L. Méndez, J. Sheil, O.O. Versolato, and R. Hoekstra, "Evidence of production of keV Sn^+ ions in the H_2 buffer gas surrounding an Sn-plasma EUV source", *Plasma Sources Sci. Technol.* **32**, 035006 (2023).

3. S. Rai, K.I. Bijlsma, I. Rabadán, L. Méndez, P.A.J. Wolff, M. Salverda, O.O. Versolato, and R. Hoekstra, "Charge exchange in collisions of 1–100 keV Sn^{3+} ions with H_2 and D_2", *Phys. Rev. A* **106**, 012804 (2022).

4. X. Wang, S. Rathnachalam, V. Zamudio-Bayer, K. Bijlsma, W. Li, R. Hoekstra, M. Kubin, M. Timm, B. von Issendorff, J.T. Lau, S. Faraji, T. Schlathölter, "Intramolecular hydrogen transfer in DNA induced by site-selective resonant core excitation", *Phys. Chem. Chem. Phys.* **24**, 7815-7825 (2022).

5. X. Wang, S. Rathnachalam, K. Bijlsma, W. Li, R. Hoekstra, M. Kubin, M. Timm, B. von Issendorff, V. Zamudio-Bayer, J.T. Lau, S. Faraji, T. Schlathölter, "Site-selective soft X-ray absorption as a tool to study protonation and electronic structure of gas-phase DNA", *Phys. Chem. Chem. Phys.* **23**, 11900-11906 (2021).

6. S. Rai, K.I. Bijlsma, S. Koeleman, O.G. Tjepkema, A.W. Noordam, H.T. Jonkman, O.O. Versolato, and R. Hoekstra, "Single-collision scattering of keV-energy Kr ions off a polycrystalline Cu surface", *Nucl. Instrum. Methods Phys. Res., Sect. B* **482**, 58-63 (2020).

Acknowledgements

Looking back at the last four and a half years, I am very grateful for having had the opportunity to do a PhD in such a nice and inspiring environment. It was not always easy, but in the end it was worth it. I truly enjoyed working in science and meeting so many interesting people. I would like to thank everyone who has helped me along the way.

Most of all, I would like to thank my supervisor Ronnie Hoekstra. Your guidance has been essential for my project. You were always available to answer my questions and to discuss my results or atomic physics in general. Thank you also for supporting me during times when I felt stuck. I admire your positive attitude and the way you manage to create a very pleasant environment in your research group.

I express my gratitude to my second supervisor, Oscar Versolato. Thank you for reading all my drafts and for quickly providing me with your valuable feedback.

I would like to thank Luis Méndez, Ismanuel Rabadán and Lamberto Oltra of the Universidad Autónoma de Madrid for the successful theory-experiment collaboration. I always enjoyed our online meetings and have learned a lot from you.

When doing experimental physics, a good research technician is worth its weight in gold. Mart, thank you for all your effort and help. Your knowledge and technical skills are impressive.

Special thanks to Luc and Alex for their work during the upgrade of CHEOPS. Emiel, thank you for your contributions during our experimental campaign. Laurens and Lucas, thank you for your help during our experiments at ARCNL.

Subam, thank you for helping me in the beginning of my PhD. I really liked working with you and I am happy we became friends.

I would like to thank John Sheil, Wim Ubachs and Wim van der Zande for their interest in my research and for the many insightful discussions we had.

Special thanks to Harry Jonkman for giving me valuable advice.

I want to thank Niels Braaksma for his enthusiasm about my research.

I would like to acknowledge all the people from the workshop, both in Groningen and in Amsterdam. Special thanks to Wigger for the many times you fixed a broken power supply.

I am thankful to all the people from the secretariat, both in Groningen and in Amsterdam.

I would like to thank Steven Hoekstra, Roger Jaspers and Stefan Schippers for accepting the invitation to take a seat in my assessment committee.

Xin, Denisse, Alexander and Yuly, I enjoyed and appreciate our coffee and lunch breaks where we could share and discuss our experiences as a PhD student.

Many thanks to Luc and Eline for being my paranymphs and helping me to prepare my defense.

I had a great time working in the Quantum Interactions and Structural Dynamics group and would like to thank all my colleagues: Ronnie, Thomas, Jan, Linda, Harry, Sadia, Oksana, Mart Johan, Subam, Xin, Wen, Yining, Mart, Denisse, Marcelo, Luc and Emiel. Also many thanks to all the bachelor and master students who have worked in the group: Wessel, Sybren, Roeland, Bas, Melav, Laurens, Wouter, Fleur, Lukas, Marco, Pieter, Alex, Boris, Ernst, Rutger, Hester, Robbert, Sjoerd, Sjoukje, Robert, Lennart, Symen, Thomas, Michiel, Matthijs and Zafer.

I appreciate having been a true part of ARCNL, even though I was working in Groningen. I want to acknowledge everyone at ARCNL who has helped me. Special thanks to Oscar, John, Wim Ubachs, Wim van der Zande, Joost, Marjan, Rosa, Romy, Laurens, Ruben, Joris, Bo, Lucas, Yahia, Diko, Lars, Zoi, Adam, Javier, Edcel, Randy, Jane, Karl, Dion, Stan, Youssef, Mikheil, Hugo, Jorge, Felix and Xyoisan.

I would like to thank my friends for all the good times we had and for their support.

Heit en Mem, Hinke en Kim, tige tank foar al jimme leafde en stipe.

Eline, you make my life so much better. Thank you for all your love and support. I love you.